Superfluid and spin dynamics of strongly interacting atomic Fermi gases

Giacomo Valtolina

SCUOLA
NORMALE
SUPERIORE

Pisa 2016

Superfluid and spin dynamics of strongly interacting atomic Fermi gases

Dissertation for Classe di Scienze Matematiche e Naturali
Scuola Normale Superiore di Pisa

submitted by

Giacomo Valtolina

Pisa, May 2016

Supervisor: Prof. Massimo Inguscio

Co-Supervisor: Dr. Giacomo Roati

Abstract

Superfluidity and magnetism represent a spectacular manifestation of strong interactions in fermionic systems. These antithetic complex many-body phases encompass a wide range of environments at different energy scales, from solid-state up to quark and nuclear matter.
Within this thesis, I have addressed some aspects of these two fundamental phenomena by exploiting ultracold atomic lithium-6 (^{6}Li) Fermi gases prepared in a optical potentials. Fermi gases of ^{6}Li atoms are particularly well suited for the investigation of strong interactions in fermionic systems. This atomic species features broad Feshbach scattering resonances, allowing an ultimate control over the inter-particle interactions, a necessary ingredient for exploring strongly interacting many-body phases in a controlled way. A celebrated example is represented by the experimental realization of the BEC-BCS crossover, where long-range Cooper pairs can be smoothly converted into bosonic molecular dimers.
During the first part of this thesis, I have built a new experimental apparatus able to produce ultracold ^{6}Li mixtures, either in the superfluid or in the normal phase, confined in optical potentials. In particular, I have demonstrated, for the first time on this atomic species, a new and robust sub-Doppler laser cooling technique based on D_1 gray molasses.
In the second part of my work, I have investigated the physics of these cold fermions trapped in a double-well potential, realized by superimposing to a standard optical dipole trap a thin repulsive barrier, which splits the harmonic potential into two reservoirs. With such a setup, I have performed two different kinds of studies. First, I have employed the optical barrier as an insulating junction connecting two superfluid samples, to investigate the coherent Josephson dynamics of such strongly interacting systems, so far never observed in these fermionic superfluids. The characterization of the superfluid dynamics allowed the determination of the Josephson coupling energy across the whole BEC-BCS crossover, which was found to be maximum at the unitary limit (i.e. at the center of the Feshbach resonance). This peculiar trend results from the interplay of both bosonic and fermionic degrees of freedom. Our results may allow an alternative way to radio-frequency spectroscopy fot the determination of the superfluid pairing gap on the BCS side of the resonance, in analogy to Giaever tunneling experiments in solid-state systems. Moreover, similarly to the phenomenology of superfluid helium, we have found that, beyond critical values of the barrier height and chemical potential imbalance, phase-slips and vortex nucleation quench the coherent dynamics in the whole crossover, leading to dissipation.

As long as the second research line is concerned, the same experimental setup allowed me to study the dynamics of repulsively interacting Fermi gases. The peculiar trapping geometry allowed to create an initial state with each side of the double-well filled with a polarized Fermi sea of up and down atoms, preparing the system into a domain-wall configuration. In particular, I have performed the quantum simulation of the textbook Stoneŕs model for itinerant ferromagnetism, and I have studied the spin transport properties of such systems over a wide range of interaction and temperature regimes. Our trap configuration (optical potential + repulsive barrier) has allowed to hinder those detrimental pairing mechanisms that affects the stability of atomic Fermi gases with resonant repulsive interactions and to demonstrate, for the first time, that a ferromagnetic instability may actually occur in this atomic system, for critical values of repulsion and temperature. This has been firstly probed by observing the softening of the spin-dipole mode while approaching the critical value of interactions. Analogously to spin fluctuations measurements, the softening of this mode is unequivocally linked to the divergence of the spin susceptibility at the ferromagnetic transition. Moreover, in a second set of experiments, I have measured the spin transport properties of such a system and consistently with the spin-dipole measurements, I have found that spin diffusion may actually stop for a finite time window for interactions above the critical one. This has allowed me to draw the critical boundary in the temperature-interaction plane for the emergence of a ferromagnetic instability.

Contents

CHAPTER 1

Introduction

The dynamical and transport properties of any physical system arise from its underlying microscopic mechanisms, whose understanding is a fundamental task for the shaping of accurate many-body theories. Several experimental observations, such as superconductivity or the quantum Hall effect, boosted the development of groundbreaking theoretical frameworks which molded our comprehension of the intrinsic mechanisms of materials.

In this picture, simulating strongly interacting systems with ultracold atomic Fermi gases has already proven to be a test-bed for many-body theories and a platform for exploring exotic, or even novel, phases of matter [1]. Their unprecedented precision, typical of the atomic physics, is a powerful and valuable resource for disclosing the intricate complexity of condensed matter systems, with a twofold interest in both fundamental and technological scientific advancements. The tunable interplay among quantum statistics, symmetry, interactions and dimensionality in atomic gases is a key inspiration for the realization of the experiments presented in this thesis, focusing on the implementation of elementary toy models of condensed matter systems, with the goal to provide a reference for state-of-the-art theoretical tools or even to prove the existence of debated phases.

Interactions drive the emergence of many intriguing phenomena in solid state physics. Notable examples are the fractional quantum Hall effect and the High-T_C superconductivity in cuprates. However, the analytical description of these strongly interacting systems is generally unfeasible, as well as their numerical simulation, since the available computation power reduces the solution to very small size problems, which lack the overall complexity of the real quantum state [2].

The presence of magnetically tunable Feshbach resonances makes ultracold atomic Fermi gases well suited for the implementation of quantum Hamiltonians of strongly interacting systems and to physically simulate their features, measurable by the evolution of both single-particle and collective excitations spectra.

At first glance, Feshbach resonances, intrinsically linked to the existence of a shallow (real or virtual) molecular state [3], provide a mechanism to pair unequal spin fermions, the necessary ingredient for superconductivity to develop. In the presence of a Fermi sea, the

Cooper instability may drive the superfluid transition for any arbitrary weak attraction. The phenomenology of this is captured by the Bardeen-Cooper-Schrieffer (BCS) theory of superconductivity. The creation of long-range Cooper pairs is the main mechanism behind the superfluid behavior of conventional superconductors, as well as for rather different fermionic systems, such as helium-3. Helium is a paradigmatic example of the rich phenomenology behind superfluidity, since even its other isotope, i.e. helium-4, may turn superfluid. The addition of a single neutron turns helium-3 into a boson. More correctly, helium-4 is a composite boson made out of fermions. In bosonic systems, superfluidity is associated to Bose-Einstein condensation, and not to the Cooper instability. It is so legitimate to ask ourselves whether a connection exists among these different regimes of superfluidity, where on one side the fermionic character of the constituents is washed out by their tight bonding.

A positive answer to this question was first given by A. Leggett in 1980[4]. He predicted the existence of a smooth crossover among long range Cooper pairs and deeply bound bosonic molecules, as the inter-species attraction is increased.

At present, ultracold atomic Fermi gases are the only experimental systems where this BEC-BCS crossover picture has been realized and investigated [5]. On top of a Feshbach resonance, these systems encompass the two paradigmatic weakly-interacting limits of superfluidity, passing through the most interacting system allowed by quantum mechanics, the so-called unitary limit, where the diverging scattering length on top of the Feshbach resonance makes the pair size and the correlation length comparable with the inter-particle distance, similarly to what happens in High-T_C superconductors at optimal doping, or even in more exotic systems such as neutron stars or the quark-gluon plasma of the early universe. These table-top atomic systems encompass quantum matter at different energy scales, allowing a transfer of knowledge from different research lines.

The main peculiarity of any superfluid is its frictionless flow when passing through obstacles or constrictions. This was intensively investigated for both superconductors and superfluid Helium, for early investigation of the superfluid gap and the critical velocity [6]. However, as pointed out by B. Josephson in the sixties, a more interesting regime arises when the obstacle or the insulator among two superfluids is smaller than, or comparable with, the superluid coherence length. The overlap between the superfluid wavefunctions on each side of the obstacle allows a direct current among the two reservoirs, even if no bias field is applied. This is the famed Josephson effect, which is not only the manifestation of a quantum effect on a macroscopic scale, but also a valuable resource for metrology and quantum information [7]. On a more fundamental level, the overlap of the two macroscopic wavefunction across the junction acts as a mutual probe of the two condensates, as their relative interference is the only way to access their most intimate feature, the superfluid order parameter. The Josephson effect connects two objects which violate the same symmetry, providing us a unique tool to physically pin down the order parameter [8]: far from being just a textbook example of a macroscopic quantum phenomenon, the Josephson effect represents a powerful possibility for probing and characterizing a superfluid state. Inspired by this, we have first experimentally investigated the still unexplored Josephson dynamics of ultracold crossover superfluids. The implementation on our set up of a high-resolution optical system allowed us to imprint onto the atomic cloud a micrometer-sized optical barrier. Acting as a tunnel junction, the barrier bisects the cloud into two reservoirs, creating an atomic physics analogue of a solid-state Josephson Junction, with our neutral fermionic atoms playing the role of electrons in superconductors. The disclosure of coherent particle transport through the junction via the observation of Josephson oscillations, together with the ultimate control over cold atoms, opens the possibility to investigate regimes where quantum fluctuations and exotic phenomena are enhanced, with a possible boomerang effect on the quest for novel quantum devices.

The unique control of interactions between Feshbach resonant ultracold atoms allowed me also to experimentally address another fundamental phenomenon, notoriously difficult to quantitatively describe: namely, itinerant ferromagnetism. In this frame, it is still debated whether a homogeneous Fermi gas can turn ferromagnetic once short-ranged repulsive interactions between particles with different spin are sufficiently strong. At the mean-field level, this picture is captured by the Stoner model of itinerant ferromagnetism, which dates back to 1933 [9]. More sophisticated theoretical models, going beyond the mean-field approximation, confirmed the occurrence of the Stoner instability and refined its properties. However, side-by-side comparison between microscopic theory models and real solid-state materials has proven to be difficult, due to unavoidable imperfections and complications, such as the presence of disorder and of intricate lattice structures. Instead, quantum gases experiments, thanks to their unprecedented cleanliness, offer an ideal battlefield for targeting this goal.

Within this spirit, we engineered a trapping configuration where the aforementioned barrier potential separates two macroscopic domains with opposite spin. Notably, in the absence of the barrier, this would almost correspond to the exact ground state predicted by the Stoner model. Our setup allowed the investigation of the (meta)stability of such an initial state, avoiding the detrimental mechanisms (i.e. pair formation and three-body recombination) that so far hindered the investigation of atomic Fermi gases with resonant repulsive interactions [10, 11]. By measuring collective modes, we probed the magnetic properties of such state at different values of the two-body scattering length. In particular, by focusing on the spin-dipole mode, i.e. the out-of-phase oscillation of the spin domains, we could unveil the trend of the spin susceptibility χ_s, which was found to abruptly increase when approaching the critical interaction, consistently with the occurrence of the

Stoner instability and the emergence of a ferromagnetic phase transition.
Further studies may shed new light on more unconventional scenarios, difficult to target in the solid state counterparts. Control over the relative spin population may allow to investigate the dynamics of impurities in a Fermi seas and their transport properties, even in reduced dimensions. The combination of this with the accurate interferometric probing techniques of atomic physics may give access to spatial and time-resolved emergence of correlations in a many-body state, a fertile and still mainly unexplored research line [12].

Outline of the thesis

This thesis is organized as follows:

- In Chapter 2, we review the basic theoretical framework for understanding the physics behind strongly interacting trapped atomic Fermi gases. The concept of Feshbach resonance is introduced, focusing on its effect at both the two-particle and the many-body level. The emergence of a *lower* and an *upper* branch in the energy landscape of this system allows to investigate two orthogonal regimes: a strongly interacting fermionic superfluid and a normal Fermi gas with repulsive interactions. Finally, the basic theory concepts to understand the two topics of this thesis, namely the coherent Josephson dynamics and itinerant ferromagnetism, will be briefly introduced.

- In Chapter 3 we give details over the experimental setup, built during the period of this thesis, which is used to perform our experiments.

- Chapter 4 covers the production of degenerate quantum gases of ^{6}Li, both in the normal and the superfluid regimes, achieved by exploiting, for the first time on this atomic species, a sub-Doppler laser cooling technique. Details on the performances of this cooling stage, called D_1 gray molasses, will be given.

- The first investigation of coherent Josephson dynamics across the BEC-BCS crossover is described in Chapter 5. By bisecting the cloud into two reservoirs, we could observe Josephson oscillations in both the population imbalance and the phase, whose frequency was measured and compared throughout whole crossover. Our results highlight the robust nature of resonant superfluids.

- Finally, in Chapter 6, we perform the quantum simulation of the Stoner model, initializing the system in two separated spin domains. Details of the initial state preparation will be given. The observation of the softening of the spin dipole mode towards the ferromagnetic transition and the occurrence of a finite time window of zero spin diffusion above it, suggest the occurrence of the Stoner instability in repulsive Fermi gases without the need of any lattice, even if in a metastable sense.

Publications

The following list of articles has been published in the context of this thesis

- A. Burchianti, G. Valtolina, J. A. Seman, E. Pace, M. De Pas, M. Inguscio, M. Zaccanti and G. Roati, *Efficient all-optical production of large* ^{6}Li *quantum gases using* D_1 *gray-molasses cooling*, Phys. Rev. A **90**, 043408 (2014).
- G. Valtolina, A. Burchianti, A. Amico, E. Neri, K. Xhani, J. A. Seman, A. Trombettoni, A. Smerzi, M. Zaccanti, M. Inguscio and G. Roati, *Josephson effect in fermionic superfluids across the BEC-BCS crossover*, Science **350**, 1505 (2015).
- G. Valtolina, F. Scazza, A. Amico, A. Burchianti, A. Recati, T. Enss, M. Inguscio, M. Zaccanti and G. Roati, *Evidence of ferromagnetic instability in a repulsive Fermi gas of ultracold atoms*, in preparation.

CHAPTER 2

Fundamentals of interacting atomic Fermi gases

The experiments presented throughout this thesis probe the dynamical properties of strongly interacting Fermi gases. Within this chapter, a brief introduction is given about the properties of these fermionic systems, focusing on the physical scenarios that tunable interactions and optical manipulation offer for the implementation of textbook models of condensed matter from an atomic physics perspective.

2.1 Degenerate Fermi Gases

Fermions are named after Enrico Fermi. In 1926 [13], the italian physicist was the first to discover the statistical laws governing these particles. Fermions, namely all elementary or composite particles with half-integer spin, obey the *Pauli exclusion principle*, which prevents two identical ones to occupy the same quantum state. Particles with integer spin instead are called bosons and obey the Bose-Einstein statistics, which allows them to condense into the same single quantum state. This different spin statistics becomes crucial as temperature is lowered down to regimes where the thermal de Broglie wavelength, defined as $\lambda_{\mathrm{dB}} = \sqrt{\frac{2\pi\hbar^2}{mk_B T}}$, becomes comparable with the interparticle distance. Here, in the so-called degenerate regime, particles are no more distinguishable and the quantum statistics starts playing a major role (see fig.2.1).

2.1.1 Ultracold atoms in harmonic traps

The energy levels that particles populate reflect the boundaries and structure of the space where they are found. The common traps for holding the atomic gases can be very well approximated by a harmonic potential, with the typical dispersion relation $\frac{1}{2}\omega_i x_i^2$, where ω_i is the trap frequency in the i-th direction.

Given the *Pauli exclusion principle*, the single-atom probability to occupy a quantum state

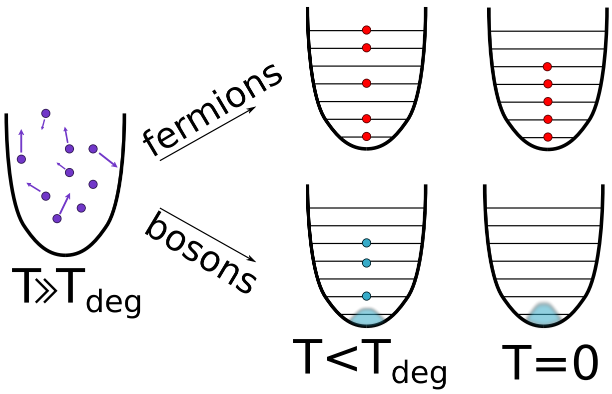

Figure 2.1 – When de Broglie wavelength λ_{dB} is of the same order of the inter particle distance d, the quantum statistics starts arising and particles organize themselves according to their spin properties. A phase transitions drive bosons to condense towards the lowest accessible energy level. Fermions instead pile up one for each level. At T=0 only the lowest states are occupied but there is no phase transition involved with this behavior.

at an energy ϵ is given by the Fermi-Dirac distribution:

$$f(\epsilon) = \frac{1}{e^{\frac{(\epsilon-\mu)}{k_B T}} + 1} \tag{2.1}$$

where $\epsilon = \frac{p^2}{2m} + V(r)$ is the sum of kinetic and potential energy, μ the chemical potential, T the temperature and k_B the Boltzmann constant.

As shown in fig.2.2, for decreasing temperatures, the Fermi distribution shows a sharper drop at the chemical potential position, due to the emergence of a Fermi surface. At $T = 0$, all energy levels from the lowest up to the chemical potential are occupied. This last one defines so the Fermi energy E_F. In the case of a three-dimensional harmonic trap, the Fermi energy is expressed as:

$$E_F = (6N)^{1/3}\hbar\overline{\omega} \tag{2.2}$$

where $\overline{\omega} = (\omega_x\omega_y\omega_z)^{1/3}$ is the geometric average of the trapping frequencies.
The Fermi energy sets the most important energy scale in the system, and eq.(2.2) is related to the peak density $n(0)$ of the gas at the trap center as $E_F = \frac{\hbar^2 k_F^2}{2m} = \frac{\hbar^2}{2m}(6\pi^2 n(0)^{2/3}$, where k_F is the Fermi momentum. The inhomogeneity of the trap makes the chemical potential position dependent. In the Local-Density-Approximation (LDA), it is convenient to define it as:

$$\mu(r) = \mu - V(r) \tag{2.3}$$

where $V(r)$ is the trapping potential. On the trap edges, we have a vanishing local chemical potential and the atomic cloud tails are essentially classical. This would be a limitation when looking for critical phenomena across a quantum phase transition, since it will happen only at the trap center due to the higher degree of degeneracy. Over the whole trap, the divergent correlation length will be renormalized to lower values, with a possible

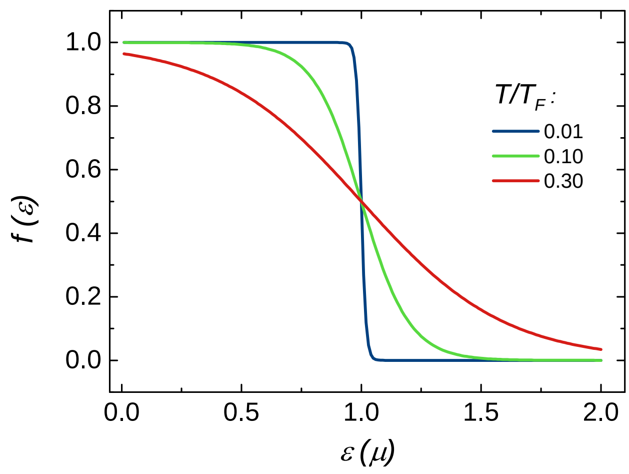

Figure 2.2 – Fermi-Dirac distribution $f(\epsilon)$ at various temperatures. The energy levels on the x-axis are in units of the chemical potential μ.

hindering of the critical phenomenon. However, the presence of the trap can sometimes turn advantageous. First of all, the trap frequency naturally provides a time reference for comparing the dynamics of collective modes. These are powerful tools for disclosing the effects of interactions and quantum fluctations on the elementary excitations of the many-body state [14, 15]. Second, the trap dispersion allows the investigation of the system over a wide range of local chemical potentials. In a single experimental shot, it is possible to reconstruct the thermodynamical properties and the phase diagram over a wide range of temperatures (i.e. degree of degeneracy).

Density distribution and temperature

Accounting for the Fermi statistics and the harmonic confinement [16], the density distribution for trapped ideal Fermi gases can be expressed as:

$$n(\mathbf{r}) = \int \frac{d\mathbf{p}}{(2\pi^3)} f(\mathbf{r},\mathbf{p}) = -\frac{1}{\lambda_{\mathrm{dB}}^3} \mathrm{Li}_{3/2}\left(-e^{\beta(\mu - V(\mathbf{r}))}\right) \tag{2.4}$$

where Li_n is the n-th order polylogarithmic function [16].

At zero temperature, the density distribution has a polynomial expression proportional to $(1-(x_i/R_{Fi})^2)^{3/2}$, vanishing at a distance $R_{Fi} = \sqrt{\frac{2E_F}{m\omega_i^2}}$, which defines the Thomas-Fermi radius along the i-th direction.

In the weakly interacting regime, the density distribution after releasing the atoms from the trap becomes isotropic at long expansion times, due to the initial isotropic momentum distribution. However, in the degenerate regime, it still reflects a strong deviation from a classical gaussian profile [17, 18], allowing to determine the temperature and the degree of degeneracy of the sample [16, 19].

2.2 Scattering theory of ultracold collisions

The scenario of cold collisions in quantum gases can be described in a simple and elegant way. Morever, the interaction strength can be easily controlled by means of magnetic Feshbach resonances [3], which allow an ultimate control over interaction tunability, unachievable in ordinary solid-state systems.

2.2.1 Elastic collisions

The simple physical picture to understand cold collisions arises from the combination of two main properties of these quantum gases. First, the inter-atom scattering potential is of Van der Waals type ($\sim -\frac{C_6}{r^6}$, where C_6 is the Van der Waals coefficient), meaning it is essentially short-ranged and with central symmetry. Second, quantum gases are extremely dilute, more than a million of times thinner than air, such that we can consider only pairwise interactions (i.e. two-body collisions).
The Schrödinger equation in the reference frame of two colliding atoms can be generally written as:

$$H|\psi\rangle = (H_0 + V(\mathbf{r}))|\psi\rangle = E|\psi\rangle \tag{2.5}$$

where H_0 is the free particle Hamiltonian and $V(\mathbf{r})$ the interaction potential.
Away from the target region, the wavefunction can be expressed as:

$$|\psi\rangle = e^{i\mathbf{k}\cdot\mathbf{r}} + f(\theta,\phi)\frac{e^{ikr}}{r} \tag{2.6}$$

i.e. as the sum of an incident plane wave and an outgoing spherical wave. This last one is modulated by the scattering amplitude $f(\theta,\phi)$ which records the amplitude and phase of the scattered components along the angular direction (θ,ϕ). This is related to the scattering cross section σ by the differential relation: $\frac{d\sigma}{d\Omega} = \frac{4\pi}{k^2}|f(\theta,\phi)|^2$, with Ω the solid angle.

Due to the central symmetry of the problem, the wavefunction can be expanded in partial waves. For any of these partial waves with a defined angular momentum l there is a Schrödinger equation with a potential given by the sum of the Van der Waals one and the centrifugal repulsive barrier at a given momentum l (see fig.2.3). At low temperatures, for the considered short-range potentials (i.e. $V(r)$ that falls off faster than $1/r^3$ at large distances, collisions in any channel with $l > 0$ are deeply suppressed. Only collisions in the s-wave $(l = 0)$ channel are allowed. At low momenta, the s-wave scattering amplitude

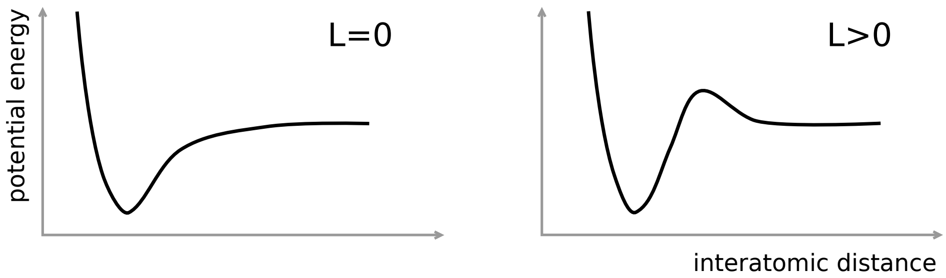

Figure 2.3 – Left panel: sketch of a typical Van der Waals potential in the s-wave channel ($l = 0$) with the $1/r^6$ scaling at long distances. Right panel: same left panel potential with the addition of the centrifugal barrier for $l > 0$. The barrier prevents atoms to approach at short distances, quenching collisions and thermalization.

can be expressed as [20]:

$$f = \frac{1}{k\cot\delta_0 + ik} \approx \frac{1}{a^{-1} + r_{\text{eff}}k^2/2 + ik} \tag{2.7}$$

The collision imprints a phase shift δ_0 onto the scattered wavefunction which, according to eq. 2.7, can be parametrized as a function of the only scattering length a and the effective range r_{eff} of the potential. Despite that a and r_{eff} are set by the microscopic details of the potential, an equal scattering amplitude can be obtained by very different microscopic interaction potentials , with the same scattering length and effective range. This allows replacing the complicated and not exactly known inter-atomic potential with a much simpler effective one, called pseudopotential, which at long distances leads to the same asymptotic behavior for the wavefunction [21].
The scattering length a is defined as:

$$a = \lim_{k\to 0} \frac{\tan\delta_0(k)}{k} \tag{2.8}$$

When δ_0 is equal to $\pm\pi/2$, a diverges. In the context of this thesis, it is instructive to understand the physical meaning of a diverging scattering length. To explain this, we analyze the scattering problem for a simple square-well pseudopotential. The well is characterized by a range R and a depth V_0. In panel 2.4, the function $u(r)$ is plotted for different V_0, with $u(r) = rR_0(r)$, where $R_0(r)$ is the s-wave solution of the radial Schrödinger equation. For repulsive wells ($V_0 > 0$) as in fig.2.4a, the boundary conditions at the origin and at $r = R$ force $u(r)$ to have a positive curvature inside the well (black solid line). The scattering length a is here defined as the intercept of the wavefunction just outside of the well, extended to all abscissas (orange dashed line). With this potential, even in the hard-sphere limit ($V_0 \to \infty$), the scattering length cannot diverge and is upper-bounded by the range R. The situation changes if the potential becomes attractive ($V_0 < 0$) as in fig.2.4b. The wavefunction curvature becomes negative, which gives an intercept for the extended wavefunction at $r < 0$, namely a negative scattering length. The analytical solution for a in this well potential reads as $a = R(1 - \tan\gamma/\gamma)$, where $\gamma = |V_0|^{1/2}R$ is equivalent to the

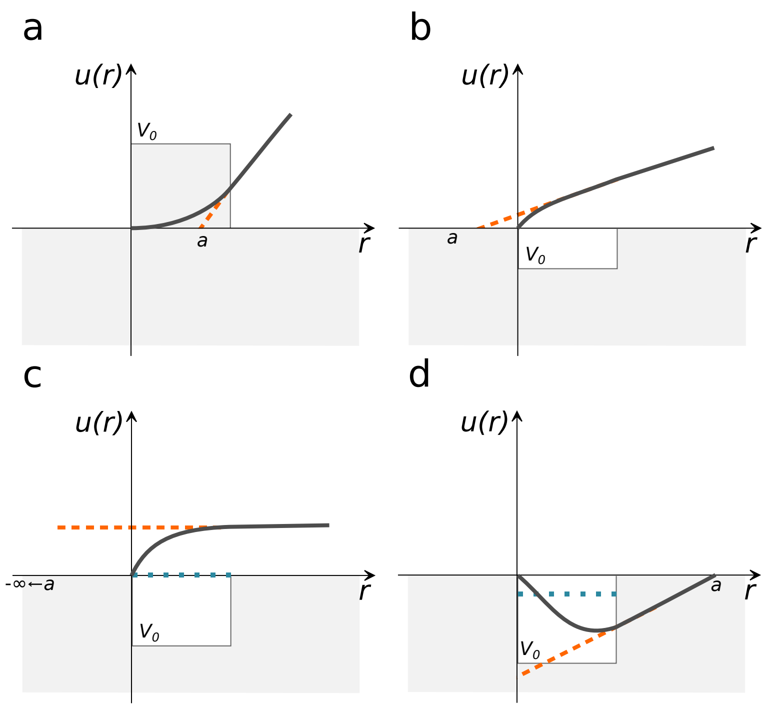

Figure 2.4 – Qualitative trend at short distances of $u(r)$ (solid line) and a (dashed orange line) for different heights V_0 of the square-well potential. The oscillating behavior at large distances ($r \ll 1/k_F$) is not reported [22]. a) $V_0 > 0$: The repulsive well does not allow a scattering length larger than the range R. b) $V_0 < 0$ but still not enough for supporting a bound state: a becomes negative as well as the curvature of $u(r)$. c) $V_0 < 0$ and a bound state (dotted blue line) is found at the same energy of the scattering threshold: the scattering length a asymptotically tends to $-\infty$. d) $V_0 < 0$ and the bound state energy is below the scattering threshold: despite the attractive potential, a is positive and the potential is effectively repulsive.

phase shift δ_0. When $|V_0|$ is further increased until $\gamma = \frac{\pi}{2}$, the scattering length diverges (see fig.2.4c). At this critical V_0, the well is deep enough to support a bound state at zero energy. Despite $a \to \infty$, the cross-section remains finite, ensuring the stability of the system. For s-wave collisions we have:

$$\sigma = \frac{4\pi}{k^2} \sin^2 \delta_0 \tag{2.9}$$

When $a \to \infty$ or equivalently $\delta_0 = \frac{\pi}{2}$, the cross section saturates to $\sigma = \frac{4\pi}{k^2}$, which is the maximum value allowed by quantum mechanics.

Coming back to the well potential exploration, a further small increase of $|V_0|$ flips the sign of a, as in fig.2.4d. Despite the overall attractive potential, the presence of a bound state just below the energy threshold of the interacting particles introduces a positive and large scattering length and consequently a repulsive interaction between atoms in scattering states. By further increasing $|V_0|$, the positive scattering length can be first reduced to zero and then turned negative again. The appearance of other bound states into the potential will create a periodic divergence in a [3]. This leads to some additional consider-

ations. First, a negative scattering potential V_0 allows both positive and negative scattering lengths, while the condition $V_0 > 0$ implies only a positive scattering length. Furthermore, purely repulsive potentials do not allow a finite scattering length in the zero-range limit ($R \to 0$), differently from attractive ones. Attractive potentials can support bound states at an energy E_b. The relative distance between the bound state and the scattering threshold at $E = 0$ sets the value of the scattering length a. At the same time, changing the scattering length means tuning the bound state energy respect to the scattering one, implying that diverging scattering lengths at both negative and positive values can be achieved only with the presence of a bound state really close to the scattering state.
Despite looking like a textbook exercise, this scenario can be actually implemented in quantum gases thanks to magnetic Feshbach resonances [23]. As it will be explained in the following sections, the "tuning" of the bound state energy will affect the mere value of the scattering length but also the ground state of the many-body system.

Role of quantum statistics

The quantum statistics introduces some constraints on the previously discussed scattering problem with short-ranged potentials. For fermions, the wavefunction must be antisymmetric respect to particles permutation. This allows the scattering to happen only in those channels with odd angular momentum l. In the cold collisions framework, this means that identical fermions do not collide. The *Pauli exclusion principle* forbids s-wave scattering and the centrifugal barrier at $l > 0$ prevents atoms to get closer one to the other and to experience the scattering potential. Two fermions with different spin can instead collide, since they are distinguishable and the s-wave channel is not impeded by any quantum statistics rule.

2.2.2 Feshbach Resonances

Thanks to the hyperfine and Zeeman structure of the atoms, the previously investigated scenario of tuning the energy of a bound state relative to the scattering channel can be actually implemented in quantum gases. The scattering state of two atoms defines the energetically accessible open channel, characterized by a certain magnetic moment μ_1. In the overall molecular spectrum of the two atoms, it may also be possible to find another scattering channel, this time closed, i.e. not energetically accessible. Suppose now that this latter potential supports a bound state with a magnetic moment μ_2 different from the open channel one (see fig.2.5). The simple application of a magnetic offset field shifts the relative energy of the bound state respect to the scattering threshold. If a hyperfine coupling exists between the two channels, a mixing among the two states will take place. As

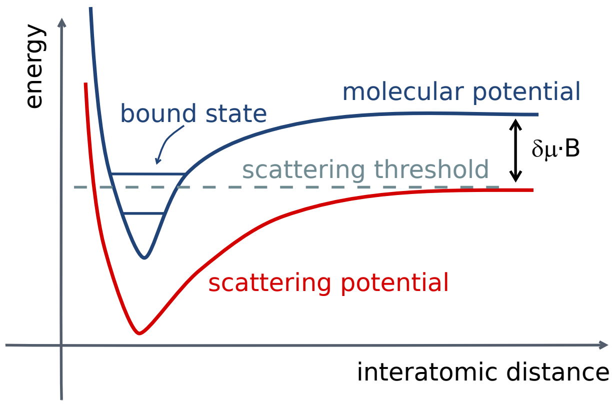

Figure 2.5 – Representation of the closed and open channel in the scattering problem. The relative energy difference can be controlled by a magnetic offset field if a non-zero difference exists among the magnetic moments of the atoms in the two channels.

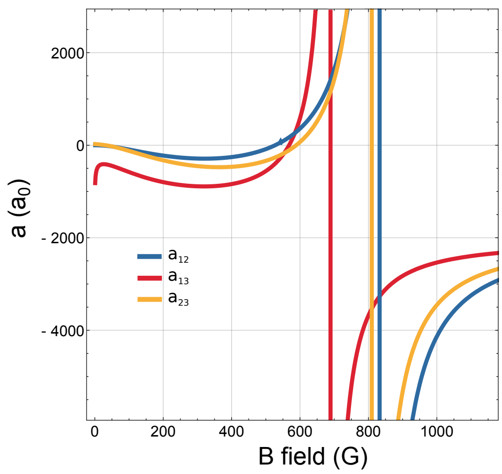

Figure 2.6 – Feshbach resonances in Lithium 6 for different hyperfine mixtures. Any of pairwise combination of the three lowest hyperfine states has one broad Feshbach resonance.

a result, the bound state will affect the continuum scattering channel with a resulting effective tuning of the scattering length. This is the phenomenon of the Feshbach resonance (FR)[24], which is an extremely powerful tool for boosting the efficiency of evaporative cooling and for exploring strongly interacting many-body phases in a controlled way. Usually, the magnetic dependent scattering length follows the relation:

$$a = a_{bg}\left(1 - \frac{\Delta}{B - B_0}\right) \tag{2.10}$$

where B_0 is the resonance center, where a diverges and the bound state reaches the scattering threshold, Δ its width and a_{bg} the background scattering length.

For ^{6}Li the FRs scenario is quite appealing. Any pairwise combination of its lowest three hyperfine states supports a broad scattering FR (see fig.2.6). The most used one is that between the lowest two states, which is located at a B_0 field of 832 G [25]. Moreover,

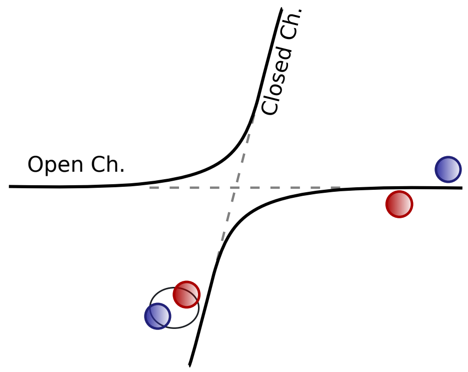

Figure 2.7 – The bare atoms and molecules form a two level system. Hyperfine coupling provides the dressing among the two. As in Landau-Zener picture, the dressing results in avoided crossing among the bare states.

Lithium FRs are among the broadest ones observed in ultracold gases. The broadness of FRs mainly affects the effective range r_{eff}, which has profound implications on both the microscopic scattering mechanism and the many-body regimes that can be accessed.
For alkali atoms, the expression for r_{eff} reads as:

$$r_{\text{eff}} = \frac{\hbar^2}{2\mu a_{\text{bg}} \Delta \delta \mu} \tag{2.11}$$

where μ is the reduced mass and $\delta\mu$ the difference in the magnetic moments between open and closed channels.
For the FR at 832 G, we have Δ=300 G and $a_{\text{bg}} = -1400a_0$. This makes r_{eff} smaller the Van der Walls one, making the scattering problem almost decoupled from the microscopic potential details and with a universal character. Coming back to eq.(2.7), we can therefore neglect the effective range term in the scattering amplitude. Without it, the scattering amplitude has a pole at an energy:

$$E_b = -\frac{\hbar^2}{2\mu a^2} \tag{2.12}$$

where E_b is the binding energy of the Feshbach molecule. The quadratic dependence on the scattering length is an evidence of strong coupling between the molecular bound state supported by the closed channel and the scattering one. Here, the bound and the scattering states can be interpreted as energy levels in a textbook two-level system. The hyperfine coupling provides the off-diagonal term in the matrix representation, which leads to the quadratic dependence in a as in the usual picture of avoided crossing (see fig.2.7). For narrow FRs instead, the dispersion relation of the binding energy is almost linear close to resonance, evidence of a weaker coupling and of non-universal character of the scattering problem.
The resulting dressed Feshbach molecule state has a molecular part embedded in the scattering one and reads as:

$$|\psi_b\rangle = \sqrt{Z}|C\rangle + e^{i\phi}\sqrt{1-Z}|Bg\rangle \tag{2.13}$$

where $|C\rangle$ is the closed channel components or bare molecular part, while $|Bg\rangle$ represents the bare atoms in the open channel. Z represents the closed-channel fraction.
Eq.(2.13) is valid for both broad and narrow resonance, but only for the first ones the fraction Z of the closed channel component is extremely small (i.e. $Z \ll 1$) over a large fraction of the resonance width Δ. In this case, the dressed bound state has a universal character and it is usually referred to as "halo dimer", since its wavefunction extends much over the classical turning point of the Van der Waals potential (that is $|\psi\rangle \propto \exp(-r/a)$). The molecular weight is zeroed if the bare bound state energy is above the open channel one. However, if we cross the resonance by shifting the relative position among the bare states, the open channel one is adiabatically converted into the dressed one, with an increasing molecular character away from the resonance center.
The resonant wavefunction has however a non-zero molecular weight at short distances, hence three-body collisions may lead to inelastic decay into more deeply bound molecules, provided these last to have a non-vanishing Franck-Condon overlap with the resonant wavefunction. Luckily again, this does not happen in ^{6}Li for two main reasons. First, the closed-channel fraction is proportional to r_{eff}/a, hence it is small and negligible over a wide magnetic field region. Second, if three fermions approach each other, two of them are identical, and so again the *Pauli exclusion principle* inhibits three-body processes [26].
About the few-body problem, FRs can be seen as a bridge among free atoms and bound molecules but they can as well dramatically affect the system at the many-body level. Notably, the experimental investigation of FRs in atomic Fermi gases led to the first realization of the famed BEC-BCS crossover. In the following, I will give a brief introduction about this scenario.

2.2.3 The energy spectrum

The general question we have to solve now is about how interactions affect the energy spectrum of a many-body system. A simple intuitive picture to this problem has been presented in ref.[27], where just two fermions with tunable interactions, confined in a box are considered [28]. Despite being extremely qualitative, the aforementioned theoretical toy model is useful for understanding the phenomenology of two Fermi gases close to a FR.
The system investigated in [27] is composed by a particle confined in a spherical box with a fixed scatterer at the center. In turn this can be qualitatively connected to the case of two homogeneous Fermi gases with opposite spin, equal number of atoms $N/2$ and equal mass m. Confining the particle in a sphere of radius $R \propto \frac{1}{k_F}$ with infinite walls mimics the effect of Pauli blocking that prevents scattering at low momenta, i.e. too large wavelengths. By introducing a fixed scatterer at the center of the box between fermions with unequal

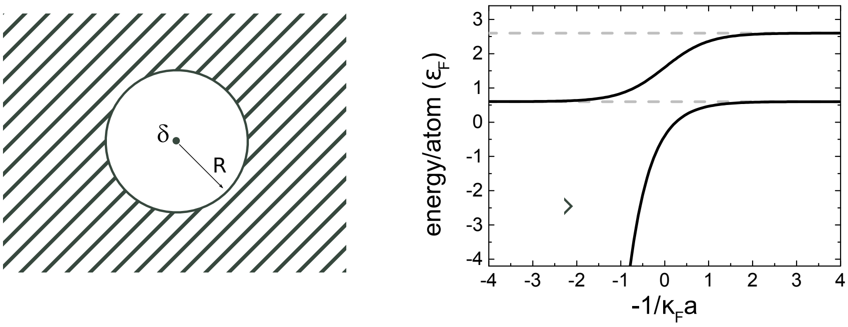

Figure 2.8 – On the left, the fictitious model of ref.[27] is represented, where the many-body problem of two interacting Fermi seas is reduced to the scattering solution of a particle in a box of radius R with a delta-like scatterer in the center. On the right, the energy spectrum for the non-interacting case (dashed gray lines) and the interacting one (black solid lines) is reported as a function of the interaction strength. Interactions mix the levels of the ladder of the non- interacting solution towards the resonance center. The drop of the lowest level for positive scattering length is due to the increasing binding energy of the atomic pair.

spin, this simple single particle picture can reproduce the case of two Fermi gases close to a Feshbach resonance (see fig.2.8). A delta functions is used to approximate the real scattering potential between the particles. For the purposes of this toy model, we can neglect the unphysical ultra-violet divergence of the delta pseudopotential and focus on the convenient approximation that it gives to the scattering amplitude. The considered pseudopotential is zero-ranged and so the scattering amplitude can be written as:

$$f = -\frac{1}{a^{-1} + ik} \tag{2.14}$$

This is the same formula of eq.(2.7) for vanishing effective range $r_{\text{eff}} \ll a$. As already stated, this is a good approximation for the case of ^{6}Li and its broad FR with universal character.

The formula in (2.14) is equivalent to introduce another boundary condition, the so-called Bethe-Peierls condition at zero interparticle distance which reads as:

$$\lim_{r\to 0} \frac{\partial_r (r\psi)}{r\psi} = -\frac{1}{a} \tag{2.15}$$

A qualitative trend of the resulting energy levels is shown in the right panel of fig.2.8 as a function of the dimensionless parameter $-1/k_F a$. The non-interacting case (gray dotted lines) shows an infinite ladder of constant levels, with equal spacing due to the boxing of the problem. For clarity we only show the lowest two of these levels. For the interacting case the situation is different. The lowest level, usually called *lower branch*, coincides with the non-interacting case for weak attractions ($-1/k_F a \to \infty$), and progressevely decreases its energy while approaching and then crossing the resonance towards ($-1/k_F a \to -\infty$). Therefore, the lower branch is associated to a net attractive interaction.

The strong energy decrease of the lower branch as $a \to 0^+$ is associated to the increase of the molecular character of the bound state and of its binding energy.
Being the lower branch associated with an effective attraction, it represents the minimal picture for the BEC-BCS crossover, leading to a superfluid state at sufficiently low temperature. The fermionic character on the attractive side is smoothly converted into a bosonic one when crossing the resonance. For sufficiently low temperatures we will find a BCS superfluid when sitting on the attractive side or a molecular Bose-Einstein Condensate on the repulsive one. The transition between these two regimes, as predicted by Leggett [4], is a crossover rather than a phase transition, since these are adiabatically connected extremes of the same branch. The lower branch is therefore the ideal playground for investigating the two aspects of fermionic superfluidity.
The first excited state is instead usually called *upper branch*. For weak repulsions ($-1/k_F a \to -\infty$) it asymptotically approaches the non-interacting ground state, while monotonically increasing its energy towards the resonance and connecting to the first excited state of the non-interacting system as $a \to 0^-$. Here, particles feel an effective repulsion when sitting on this branch for positive scattering lengths, differently from the effective attraction on the lower branch [29]. This can be further understood by looking at the wavefunction of the two-body solution for the different branches, as sketched in fig.2.9. While on the lower branch, when moving from the BCS to the BEC side, the wavefunction acquires the exponentially decaying character of the bound state, on the upper-branch the wavefunction gets a node in the radial direction when moving towards the resonance from the BEC side. In the thermodynamic limit this would describe a state orthogonal to the BEC-BCS crossover superfluid, with the node introducing an effective repulsion among the particles. The upper branch is therefore the place where normal repulsive Fermi gases can be studied. However, in real 3D many-body system this would be intrinsically metastable, since the true ground state is the paired one. Three-body recombination leads to the decay towards the lower branch. Nonetheless, if populated for sufficiently long time, the upper branch allows the investigation of ferromagnetic phenomena of a repulsive Fermi liquid [29].
Very importantly, at $1/k_F a = 0$ both the upper and lower branch exhibit an energy which does not depend by a, but only on E_F. Hence, the properties of the system are expected to be universal. Within this thesis, I actually probed both the superfluid properties on the BEC-BCS crossover and the magnetic ones on the upper branch of the system. The physical picture arising from this brief introduction will be discussed in more details in the following sections.

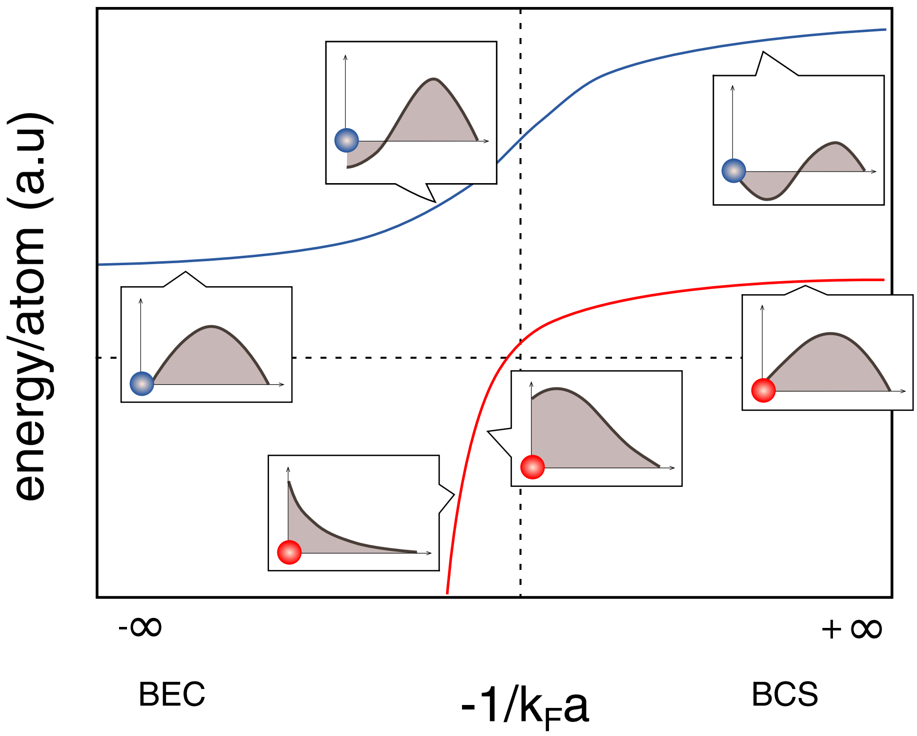

Figure 2.9 – Evolution of the two body wavefunction across the Feshbach resonance for the lower and upper branch. The wavefunction at weak interactions on the lower branch is almost equal to the upper branch one at weak repulsion. The two branches are indeed adiabatically connected by the zero crossing of the Feshbach resonance. After [30].

2.3 BEC-BCS Crossover

The bridge among atom pairs and molecules allows us to investigate the Leggett's picture of the BEC-BCS crossover on the lower branch of a Feshbach resonance. The crossover spans among the two paradigmatic regimes of superfluidity: a fermionic BCS superfluid of long-range Cooper pairs on the attractive side of the FR and a Bose-Einstein Condensate (BEC) of tightly bound molecules on the repulsive one. In the intermediate regime, where the scattering length diverges on top of the resonance, the gas is said to be a unitary one. With the scattering length dropping out of the problem, the gas has a universal character since the only relevant scales are set by the Fermi energy E_F and the Fermi momentum k_F [4]. The unitary limit is a pristine realization of a many-body system which encompasses quantum matter at different energy scale, and therefore a rich test-bed for quantum many-body theories.

BEC side: Bose gas of tightly bound molecules

On the repulsive side of the Feshbach resonance, halo dimers are converted into deeply bound molecules when the scattering length is reduced. For a sufficiently large bind-

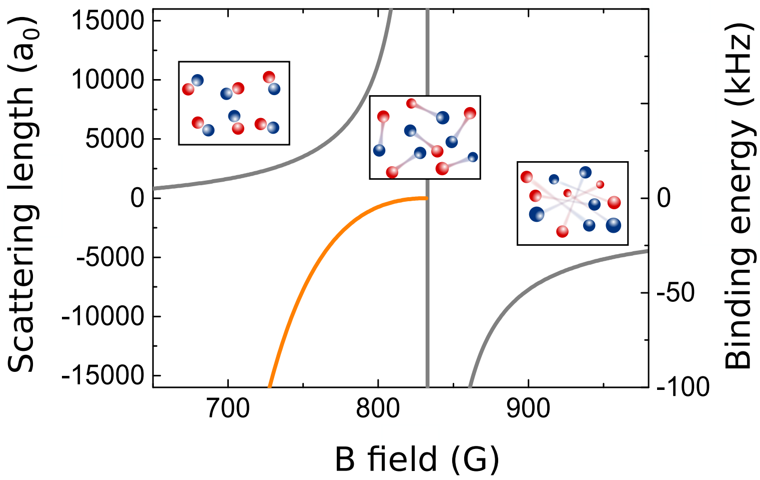

Figure 2.10 – Different regimes of fermionic superfluidity across the BEC-BCS crossover. Just by changing the value of an external magnetic field we can smoothly pass from a Bose condensate of tightly bound molecules to a BCS Fermi gas.

ing energy, these composite molecules behave like bosons, their size being much smaller than the inter-particle distance. In this limit, few-body calculations [26] found that the dimer-dimer scattering length a_m is related to the atom scattering length by the relation $a_m = 0.6a$. Dimers, though less than free atoms, interact repulsively with each other, ensuring a relatively large stability with respect to collapse into more deeply bound molecules. The same calculation found that the atom-dimer scattering length a_{ad} is related to the atomic one by the relation $a_{ad} = 1.2a$

If the temperature is sufficiently low, these dimers may undergo Bose-Einstein condensation [31]. For trapped gases [32] and weak repulsive interactions, the critical temperature for condensation is expressed as

$$T_{BEC} = \frac{\hbar\bar{\omega}}{k_B}\left(\frac{N}{\zeta(3)}\right)^{1/3} \tag{2.16}$$

where $\zeta(n)$ is the Riemann zeta function.

Below T_{BEC}, a macroscopic occupancy of the lowest energy level occurs. The ratio of the number of atoms in the lowest level N_0 respect to the total number N can be expressed as

$$\frac{N_0}{N} = \left(1 - \frac{T}{T_0}\right)^3 \tag{2.17}$$

For samples with temperature above T_{BEC} the momentum distribution measured after release from the trap has a gaussian profile, as expected for a thermal cloud. Below T_{BEC}, the distribution becomes bimodal, with a peak in the center of the gaussian profile [32], increasing in height as the temperature is further reduced. The emergenge of a BEC in these dimerized gases has been proven in [33–35], demonstrating one limiting case of the whole crossover picture.

BCS side: weakly bound Cooper pairs

When the scattering length is negative and the temperature sufficiently low, the Fermi gas can be unstable towards Cooper pairs formation [36]. Introduced by Bardeen, Cooper and Schrieffer in 1957 [37], BCS theory was the first one to successfully describe superconductivity in normal metals and it is applicable also on the attractive side of a Feshbach resonance where no two-body bound state exists in vacuum.
When the Cooper instability takes place, an energy gap appears in the excitation spectrum of the Fermi sea, which can be expressed as:

$$\Delta_{\text{gap}} = \frac{8}{e^2} E_F e^{-\pi/2k_F|a|} \tag{2.18}$$

At the mean-field level, the critical temperature for the emergence of a gap reads as:

$$T_C = 0.28 T_F e^2 e^{-\pi/2k_F|a|} \tag{2.19}$$

Below T_C, the neutral atomic gas is expected to be superfluid, in analogy to the emergence of superconductivity of charged particles in metals.
Differently from the BEC side, the momentum distribution measured after release from the trap does not show a central peak or any other feature of an occurring superfluid phase transition [38].
The most important characteristic on the BCS side is the emergence of the superfluid gap Δ, which acts as the order parameter of the superfluid state. This is a genuine fermionic property, not present at all for purely bosonic superfluid. In a simple interpretation, the gap sets an energy shell of width Δ around the Fermi surface where the pairing occurs. As expressed in eq.2.18, the gap is exponentially vanishing with interactions, making the BCS state extremely fragile. Despite being small, the gap drastically affects the density of states at the Fermi energy and consequently the whole many-body picture is linked to it. Accessing this quantity is so of paramount importance. In solid-state physics, this is generally accomplished by both tunneling experiments [39] and ARPES spectroscopy [40], based on which the amplitude and symmetries of the order parameter can be determined. In quantum gases, this investigation has been restricted only to radio-frequency spectroscopy, by observing a gap opening in the excitation spectrum [41, 42].

Unitary Fermi gas

On top of the FR the previous two limiting cases of superfluidity are connected by the so-called Unitary Fermi Gas (UFG). Here, the scattering length diverges and the cross section

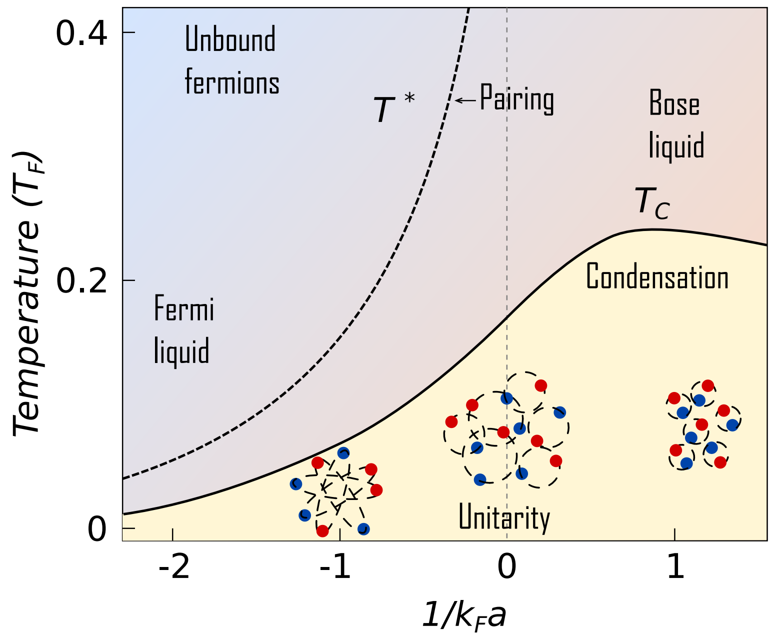

Figure 2.11 – Theoretically expected phase diagram as a function of temperature and interaction strength across the BEC-BCS crossover. Exploration of the Pseudo-gap phase in the Unitary Fermi gas should allow to unveil microscopic mechanism behind High-T$_C$ superconductivity. Picture taken from [43].

reaches its maximum value allowed by quantum mechanics, thus realizing a paradigmatic strongly interacting many-body system [44].

As for the toy model of previous section, with the scattering length dropping out of the problem, all thermodynamical quantities become universal functions of the Fermi energy. For instance, the energy per particle E/N and the pressure P are related to ideal gas values by the expressions $E/N = (1+\beta)3E_F/5$ and $P = (1+\beta)nE_F$, where β is the so-called Bertsch parameter [45].

A large part of the interest in resonant superfluidity in atomic gases is due to speculated connections with pairing effects in High-T_C superconductors [46]. In both systems superfluidity occurs at relatively high temperatures and in a strongly interacting regime [47, 48], but more importantly, in the whole crossover, the superfluid healing length reaches a minimum on top of the resonance and becomes comparable with the interparticle distance, in analogy to what happens for High-T_C superconductors at optimal doping. Despite being discovered already in 1986 [49] by Bednorz and Müller, the microscopic origin of such phenomenon is still not fully understood.

Ultracold atoms, thanks to the high control over a wide range of parameters, such as temperature, dimensionality, interactions and spin-imbalance are an ideal toolbox for investigating on the physics behind strongly correlated superfluids [46]. One example of an expected phase diagram for a 3D Fermi gas is shown in fig.2.11. Besides the conventional superfluid and normal Fermi liquid phases, more exotic phases are expected to show up.

One of these is the pseudo-gap regime, where fermion pairs are created above the superfluid transition. Despite many evidences of this pseudo-gap in High-T_C superconductors [50, 51], a consensus on its origin and its role on high-temperature superconductivity is still missing.
Going beyond these general considerations, the superfluid properties are strongly affected by the nature of the pairs. On the BCS side, the single-particle momentum distribution looks like the normal Fermi gas step-function, only broadened over a small width $\Delta \ll E_F$ af the Fermi wavevector. Towards the BEC side, this broadening is increased, more momentum states are occupied and the Fermi surface gets washed out, reflecting the higher bosonic character of the pairs [52, 53]. The crossing from fermionic to bosonic statistic affects the overall properties of these fermionic superfluids. First of all, as just said, on the BCS side in the limit of weak attractions ($1/k_F a \to -\infty$), the gas is essentially a normal Fermi one, with a chemical potential μ close to the Fermi energy ($\mu \sim E_F$), while on the BEC side the chemical potential can be expressed at the mean-field level as:

$$\mu = -\frac{\hbar^2}{2ma^2} + \frac{\pi \hbar^2 a n}{m} \tag{2.20}$$

where the first term is the molecular binding energy per fermion, while the second is a mean-field contribution due to the repulsive interactions of molecules [26].
Naively, when μ turns negative on the BEC side, the Fermi surface disappears as well as the fermionic gap Δ at finite momentum in the single-fermion excitation spectrum (see below).
On the BCS side, the stiffness of the Fermi surface introduces a strong modulation in the spatial Cooper pair wavefunction at the inverse Fermi wavevector $1/k_F$, with a typical length-scale associated with the two-particle correlation length ξ_0, much larger than $1/k_F$. The broadening in the momentum distribution towards the BEC side reduces the extension of the pair wavefunction. In the deep BEC limit this approaches the extent of a molecule of size $\sim a$.
As anticipated, the single-particle excitation spectrum is affected as well by the pairing mechanism, as shown in fig.2.12. On the BEC side, the spectrum has a minimum at $k = 0$, in accordance to the Bogolioubov picture. Towards the unitary limit, the minimum shifts at a finite momentum $k < k_F$, evidence of a gapped Fermi surface. Further in the BCS limit, the position of the minimum approaches k_F and its peak value becomes vanishing small, according to the superfluid gap trend.
So far, one way to probe this spectrum was accomplished by moving an obstacle at a certain velocity in the superfluid, looking at the creation of elementary excitations (heating) into it. According to the Landau's criterion for superfluidity, energy cannot be dissipated into any superfluid by an object, which moves at a velocity below a certain critical one. The critical velocity was found, both theoretically [54] and experimentally [55, 56], to

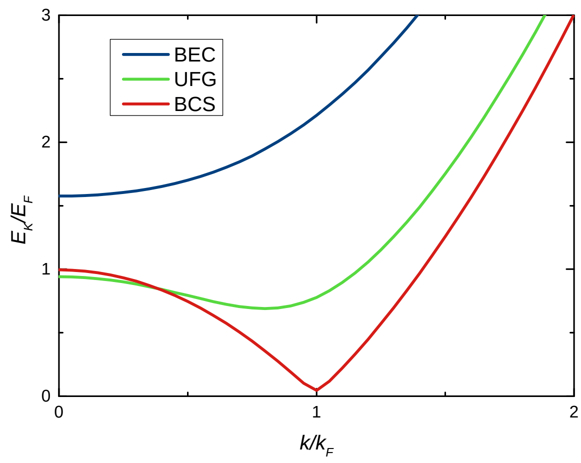

Figure 2.12 – Qualitative mean-field trend of the single-particle excitation spectrum across the BEC-BCS crossover. On the BEC side ($1/k_F a \simeq 1$ in the graph, blue line), the spectrum has a minimum at $k = 0$, while this shifts at $k > 0$ on resonance ($1/k_F a = 0$, green line) and becomes more pronounced on the BCS side ($1/k_F a \simeq -1$, red line) and close to k_F. After [5].

be maximum on resonance due to increasing robustness against limitations set by both bosonic sound modes and fermionic pair-breaking. Further studies are however needed to disclose the properties of these resonant superfluids, in particular in the coherent regime where the superfluid flow is not quenched by heating effects.

It is so possible to excite a BEC-BCS crossover superfluid in two ways. One is a bosonic density fluctuation exciting the whole fermionic pairs, the other is a single-atom excitation, related to pair-breaking. Due to the character of the pair wavefunction, only bosonic excitations affect the system on the BEC side, since the pair-breaking energy becomes too large because of the strong interatomic binding and any fermionic character can't be discerned anymore. The properties of such a Bose condensate, as pointed out by London [57] and later by Penrose and Onsager [58], should be described by the one-particle density matrix:

$$\rho_1(r, r') = \langle \Psi_B^\dagger(r) \Psi_B(r') \rangle \tag{2.21}$$

where $\Psi_B^\dagger(r)$ is the bosonic creation operator. The presence of a macroscopically occupied quantum state, such as a condensate, should be signaled by the existence of long-range order and so of a non-vanishing value of eq.(2.21) at long distances, as:

$$\lim_{|r-r'|\to\infty} \rho_1(r, r') = \psi_B(r) \psi_B^*(r') \tag{2.22}$$

where $\psi_B(r)$ is the direct bosonic wavefunction. Even in the thermodynamic limit, the number of condensed particles $N_0 = \int d^3r |\psi_B(r)|^2$ is sizeable respect to the whole particle number N.

For fermionic superfluids, the existence of long-range order is apparent in the two-particle density matrix ρ_2, since Pauli blocking prevents macroscopic occupation of a single quantum state. The ρ_2 can be written as:

$$\rho_2(r_1, r_2, r_1', r_2') = \langle \Psi_\uparrow^\dagger(r_1)\Psi_\downarrow^\dagger(r_2)\Psi_\downarrow(r_2')\Psi_\uparrow(r_1')\rangle \tag{2.23}$$

where $\Psi_\uparrow^\dagger$ ($\Psi_\downarrow^\dagger$) is the creation operator of a fermion with spin up (down).
Again in the long distance limit, eq.(2.23) leads to:

$$\lim_{|R-R'|\to\infty} \rho_2(r_1, r_2, r_1', r_2') = \psi(r_1, r_2)\psi^*(r_1' r_2') \tag{2.24}$$

where we have used the center of mass notation $R = (r_1 + r_2)/2$ and $R' = (r_1' + r_2')/2$.
The term $\psi(r_1, r_2) = \langle \Psi_\uparrow^\dagger(r_1)\Psi_\downarrow^\dagger(r_2)\rangle$ is the BCS pair wavefunction and from it we can write down the condensate fraction n_0 as:

$$n_0(R) = \int d^3r |\psi(R + r/2, R - r/2)|^2 \tag{2.25}$$

where $r = (r_1 - r_2)/2$. In a homogeneous system [59], eq.(2.25) reduces to:

$$n_0 \propto n \frac{\Delta}{E_F} \sqrt{\frac{\mu + \sqrt{\mu^2 + \Delta^2}}{E_F}} \tag{2.26}$$

On the BCS side, the condensed fraction is proportional to the finite superfluid gap Δ. The formula in eq.(2.26) for the deep BEC limit gives $n_0 = n/2$, the factor of 2 coming from n_0 being the density of molecules and n the atomic one. This is consistent with the one-body matrix results of eq.(2.22), giving a condensed fraction close to 1. Some theoretical expectations for the condensed fraction are reported in fig.2.13. As one can notice, the condensed fraction is around unity for a non-interacting BEC, while, when interactions are turned on, the zero-momentum state is depopulated and higher momenta are occupied. This is the quantum depletion predicted by the Bogoliubov theory for an interacting Bose gas. Towards the BCS side, the *Pauli exclusion principle* provides the main mechanism for depleting the condensate, reducing its size only to an amplitude Δ around the Fermi surface.
It is worth to remind that the condensed fraction is different from the superfluid one [60]. The latter one quantifies the part of the system which, after experiencing an external perturbation such as a rotation or the presence of a moving object, does not respond. A non-interacting BEC can be all condensed, but its superfluid fraction is zero, while for a two-dimensional Bose gas there could be a superfluid response even if no condensation is expected [61]. For the BEC-BCS crossover case, at $T = 0$ the superfluid fraction is constant and equal to unity across a considerable range. A first experimental measurement of the superfluid fraction for a resonantly interacting Fermi gas was achieved by excitation of the

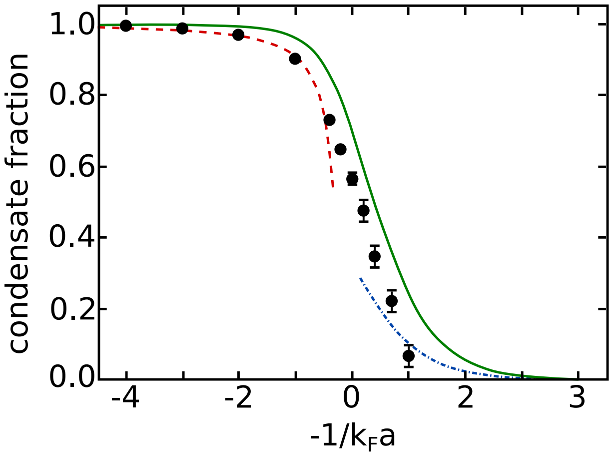

Figure 2.13 – Evolution of the condensed fraction across the BEC-BCS crossover. Its value approaches 1 in the BEC limit and exponentially vanishes on the BCS side, similarly to the superfluid gap. Symbols are for Quantum Monte Carlo simulation, red dashed line for Bogoliubov model for a molecular BEC with $a_m = 0.6a$, blue dot-dashed line for BCS theory, and green solid line for a self-consistent mean-field theory. From [52].

second sound mode [62], namely the out-of-phase oscillation of the normal component versus the superfluid counterpart. By looking at its dispersion into the atomic cloud, the superfluid fraction was found to increase very fast below the critical temperature, similarly to the case of Helium-4. In the lowest temperature regime achievable by conventional quantum gases experiments, the superfluid fraction for the Unitary Fermi gas saturates to unity. It may be inferred an analogous result for the remaining strongly interacting regime ($-1 \leq 1/k_F a \leq 1$), but an experimental confirmation is still missing.

2.4 Probing the lower and upper branches: from superfluidity to magnetism

As introduced before, depending on which branch the system is sitting different phenomena arise. The scope of my thesis has been the investigation of the dynamical properties on each individual branch.

In the lower branch atoms with opposite spin feel an attraction which causes pairing and eventually superfluidity. Here we focused on one aspect which represents a hallmark of superfluid coherent transport, namely the Josephson effect, and we used it as an effective probe for the condensate wavefunction in the superfluid state.

The upper branch features no pairing siince atoms with opposite spin interact repulsively. Within this framework, we performed the quantum simulation of the still debated Stoner model of itinerant ferromagnetism.

In the following, a theoretical description of both the Josephson effect and the Stoner

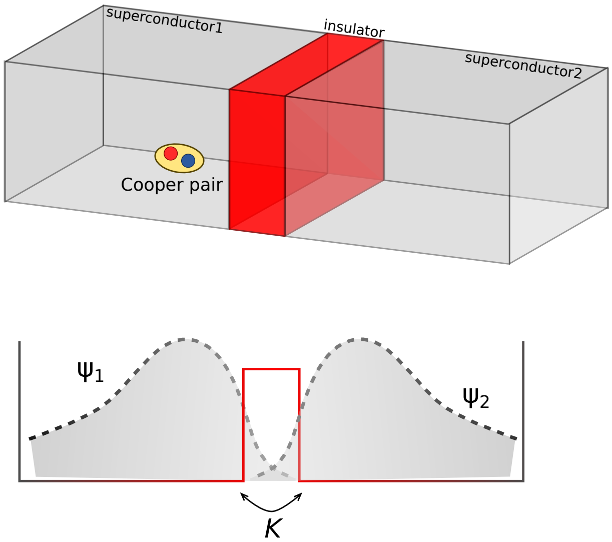

Figure 2.14 – Top panel: sketch of a typical Josephson Junction, where two superconductive metals (gray) are separated by a thin insulator (red). Bottom panel: representation of the macroscopic condensate wavefunctions in the above Josephson Junction. Despite the vanishing order parameter in the insulator, a finite coupling K may be established by the wavefunctions overlap.

model will be given.

2.4.1 The Josephson effect for quantum gases in a double well

When atomic physicists started to investigate atomic BECs in the late 90s, one of the first seminal results was the observation of interference patterns among two expanding condensate [63]. Supported by the later observation of arrays of quantized vortices [64–66], this was an evidence of superfluidity and of the existence of macroscopic phase coherence, connected to a global condensate wavefunction. These are necessary conditions also for the occurrence of the Josephson effect in atomic quantum gases.
The basic configuration for observing the Josephson effect is represented in fig.2.14, where two coherent quantum states are separated by a potential barrier. If the barrier is thin enough, the two wavefunctions may overlap inside of it, allowing a coupling which in turn drives a particle flow or current among the two distinct sites.
Back to the example of fig.2.14 we can assume the condensate wavefunction to be written as:

$$\psi_i = \sqrt{\rho_i} e^{i\phi_i} \tag{2.27}$$

where $i = 1, 2$ is the label site, ρ_i the condensate "charge" density and ϕ_i its global phase. If a weak, though non-zero coupling K is established between the two condensates, by solving the coupled Schrödinger equations the time derivative of ρ defines a net current J

flowing among the reservoirs through the barrier, which reads as:

$$J = \dot{\rho} = \frac{2K}{\hbar}\sqrt{\rho_1\rho_2}\sin\phi = J_0\sin\phi \tag{2.28}$$

where $\phi = \phi_1 - \phi_2$ is the phase difference between the two condensates and J_0 the maximum Josephson current. From eq.(2.28), one can therefore see how the Josephson effect relates a physical quantity, the current, to a more elusive one, the phase, directly connected to the order parameter ψ.

If a potential difference V exists among the two sites, the time derivative of the relative phase ϕ can be written as:

$$\frac{\partial\phi}{\partial t} = \frac{q}{\hbar}V \tag{2.29}$$

where for a superconductor $q = 2q_e$ is the charge of a Cooper pair and q_e the charge of a single electron.

When $V = 0$, we may have a DC current flowing through the barrier, with an upper bound given by J_0. This is the so-called DC Josephson effect. Instead, for a constant non-zero voltage drop, the phase evolves as $\phi(t) = \frac{qV}{\hbar}t$. Inserting this in eq.(2.28), a regime of alternated current is achieved, called AC Josephson effect, with a characteristic current frequency at $\omega = \frac{qV}{\hbar}$.

Thanks to optical manipulation, it is possible to engineer a potential landscape for cold atoms very similar to the one experienced by electrons in a Josephson junction. By bisecting a cloud with a repulsive potential barrier, or by placing the atoms into two nearest sites of a superlattice, one can exactly reproduce the situation of two superfluid reservoirs separated by a thin insulator as in fig.2.14.

Let us first focus on the Josephson effect of a weakly interacting BEC, where pair-breaking effects can be neglected and the system is captured by a Gross-Pitaevskii equation [67]. In the case of an atomic BEC, we can write the condensate wavefunction of eq.(2.27) as $\psi_i = \sqrt{N_i}e^{i\phi_i}$, with N_i being the number of atoms for the condensate on site i. Using the Gross-Pitaevskii equation for a BEC, the time-evolution for the condensate on site 1 can be written as:

$$i\hbar\frac{\partial\psi_1}{\partial t} = (V + U|\psi_1|^2)\psi_1 - K\psi_2 \tag{2.30}$$

with the equation for the site 2 mirroring this one.

The term U in eq.(2.30) is due to the on-site interactions. Because of its coupling to $|\psi|^2$, the U term introduces a non-linearity in the evolution and consequently new dynamical phases, as it will be explained later. The expression in eq.(2.30) has a physical sense in the so-called two-mode approximation, valid for a barrier height much larger than the chemical potential of the condensates. In this way we can properly define two separate wavefunctions, as well as the coupling K.

After some math [68], the condensate dynamics can be described in terms of an effective

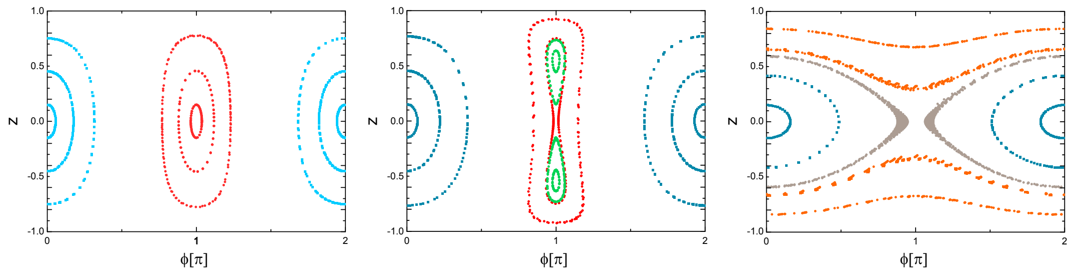

Figure 2.15 – Transition from Rabi to Josephson regime. On the left panel ($\Lambda = 0.4$), the phase portrait shows closed orbits around the $(0, 0)$ and $(0, \pi)$ phase-space points. When Λ is increased over one (central panel $\Lambda = 1.2$), the bifurcation of the $(0, \pi)$ occurs with resulting π-modes with a non zero average population imbalance (green symbols). For larger Λ (right panel $\Lambda = 10$), the typical MQST orbits happen (orange symbols) with a non zero average imbalance and a running phase. After [69].

Hamiltonian which, for $V = 0$, can be written as:

$$H = \frac{E_C}{2} z^2 - E_J \cos\phi \tag{2.31}$$

where E_C is the charging energy and E_J the Josephson tunneling energy. We have introduced the new conjugate physical quantities, the population imbalance $z = \frac{N_1 - N_2}{N_0}$ and the relative phase $\phi = \phi_1 - \phi_2$, with N_0 being the total number of atoms in the condensate. After eq.(2.31), the time dependence of z and ϕ reads as [68]:

$$\dot{z} = -\frac{\partial H}{\partial(\hbar\phi)} = \frac{E_J}{\hbar} \sin\phi, \tag{2.32}$$

$$\dot{\phi} = \frac{\partial H}{\partial(\hbar z)} = \frac{E_C}{\hbar} \cos\phi \tag{2.33}$$

The definition of the atomic current is $I = -dzdt = I_0 \sin\phi$, which again recovers the typical sinusoidal behavior of the Josephson effect, with $I_0 = 2E_J/\hbar$ and the factor of two accounting for the composite nature of the pairs [68].
From E_C and E_J, we can define the parameter Λ as $\Lambda = E_C/E_J$. The value of Λ shapes the landscape of the possible dynamical trajectories of z and ϕ. It is usually possible to distinguish between three regimes: Rabi ($\Lambda \to 0$), Josephson ($\Lambda \sim 1$) and Fock ($\Lambda \to \infty$). In our experimental investigation, we cannot access neither the Fock regime, due to too large atom number, nor the Rabi regime, because of too large interactions. This last regime has been achieved in atomic quantum gases only in an internal Josephson junction [69], thanks to the possibility of reduci almost to zero the interactions in those spinor BECs. Here, we only show in fig.2.15 how the dynamics in the system evolves as a function of the Λ term in the (z,ϕ) plane for both the Rabi and Josephson regime, which for the features of our system is the one we can deeply study.

An important dynamical regime of Josephson oscillations is achieved in the linear limit ($z \ll 1, \phi \ll 1$), where both the imbalance and the phase undergo a sinusoidal oscillations with a $\pi/2$ relative phase-shift, at the same frequency given by:

$$\omega_J = \frac{1}{\hbar}\sqrt{E_C E_J} \tag{2.34}$$

This is analogous to the Josephson plasma frequency [70] observed in BCS superconductors [71]. Usually [68, 70], the charge and Josephson energy can respectively be expressed as $E_C = 2\frac{d\mu}{dN}$ and $E_J = N_0 K/2$. The charge energy is proportional to the chemical potential. For the case of a bosonic superfluid, the chemical potential is proportional to interactions and when these are too large, the E_C term tends to localize the condensate in each separate well. On the contrary, the Josephson energy quantifies the system tendency to delocalization and sets the robustenss of the superflow, being proportional to both the tunneling K through the barrier and the condensate fraction N_0.

Some important considerations have to be made for the case of BEC-BCS fermionic superfluids. First, for the charging energy, we can write down the general relation $E_C \propto \frac{\partial \mu}{\partial N} \propto 1/\kappa$, with κ being the thermodynamical compressibility. Due to Pauli blocking, κ goes to zero on the BCS side, while increasing towards the BEC regime, being infinite for an ideal non-interacting Bose gas. In our system, three-body recombination effects impede to access the regime of weak inter-molecule interactions, hence, even at the lowest accessible $k_F a$ on the BEC side, the charging energy E_C is always large. This prevents the observation of Rabi dynamics in our system, since the Λ term is always above unity. While E_C monotonically increases from the BEC to the BCS limit, the Josephson energy E_J is influenced by the nature of the particles tunneling through the junction. We can approximate the junction Hamiltonian as:

$$H = H_1 + H_2 + H_t \tag{2.35}$$

where $H_{1,2}$ are the local Hamiltonians of the condensates reservoir and $H_t = -\sum t_{1,2} a_1^\dagger a_2 + h.c.$ is the transfer Hamiltonian, with $t_{1,2}$ being the tunneling amplitude and $a_i^\dagger$ the creation operator of a particle on site i.

Treating perturbatively the transfer matrix H_t [72], for the case of a Bose gas the Josephson energy arises already at first order, reading, for the case of $T = 0$ [72], as:

$$E_J = \langle \psi | H_t | \psi \rangle = 2 t_{1,2} N_0 \tag{2.36}$$

For genuine fermionic superfluids, being the tunneling associated to Cooper pairs, the first term vanishes. E_J becomes proportional to the second order term $|t_{1,2}|^2$ and it is possible to recover the Ambegaokar-Baratoff formula [73]:

$$E_J \propto \Delta \tanh(\beta\Delta/2) \tag{2.37}$$

with $\beta = 1/k_B T$.

The Josephson energy is so proportional to the condensate amplitude for both the BEC and the BCS case. The Josephson plasma frequency is connected in both cases to the microscopic properties of the superfluid state, and it can therefore be exploited as a weak probe of their intimate order parameter.

The Josephson regime may support other dynamical phases. Given a certain imbalance, for increasing values of Λ, the nice plasma oscillations get more and more anharmonic until a critical value Λ_C, where the oscillation becomes over-damped. For $\Lambda > \Lambda_C$, a new dynamical phase is reached, usually called Macroscopic Quantum Self-Trapping (MQST). In the MQST the population undergoes small and fast oscillations at a mean value different from zero ($\langle z \rangle \neq 0$). Moreover, the phase does not perform a bounded orbit around the π-point, but periodically runs from 0 to 2π through phase-slippage.

In a genuine two-mode picture, these different trajectories may as well be explored by changing the initial population imbalance. Given a certain value of $\Lambda > 1$, it is possible to define a certain critical population imbalance z_C at which, as for Λ_C, the dynamics looks over damped. For an initial $z_0 \ll z_C$ we recover the harmonic plasma oscillations, while for $z_0 \gg z_C$ we enter into the MQST.

The MQST is a non-linear effect due to the self-interactions in each well. When the imbalance surpasses the z_C critical value, the internal energy of the condensates differs so much that the two sites are brought off resonance, with a resulting localization of most of the particles on one site. The large energy difference brings the phase to run, but this is a completely different regime from the AC Josephson effect since it is self-sustained and dependent on the initial conditions[74]. So far, this dynamical regime has been demonstrated in a large variety of synthetic bosonic systems, from the first observations in quantum gases [75, 76] to their investigation in polaritonic systems [77].

The MQST is a phase that arise from a first-order treatment of the tunneling Hamiltonian in eq.(2.35). The inclusion of higher-order terms [72] in the tunneling Hamiltonian of eq.(2.35) introduces the effect of non-condensate particles currents through the junction. These are expected to eliminate the MQST phase at long evolution times making this regime intrinsically metastable. We expect these higher-order terms to play a more significant role with respect to the previously discussed bosonic systems [75–77]. First of all, as discussed above for the derivation of the Ambegaokar-Baratoff formula, the first-order term vanishes for Cooper pairs tunneling. Moreover, the strong interactions in the BEC-BCS crossover reduce the condensate fraction from unity [52], eventually increasing the role of non-condensed particles in the tunneling dynamics and consequently washing out the MQST regime.

In BCS superconductors the MQST dynamical phase has been elusive so far and it is very difficult to observe. The main problem is due to the extremely weak interactions, that would require a high initial population imbalance and consequently an application of a large voltage drop across the junction. However, before reaching the required imbalance,

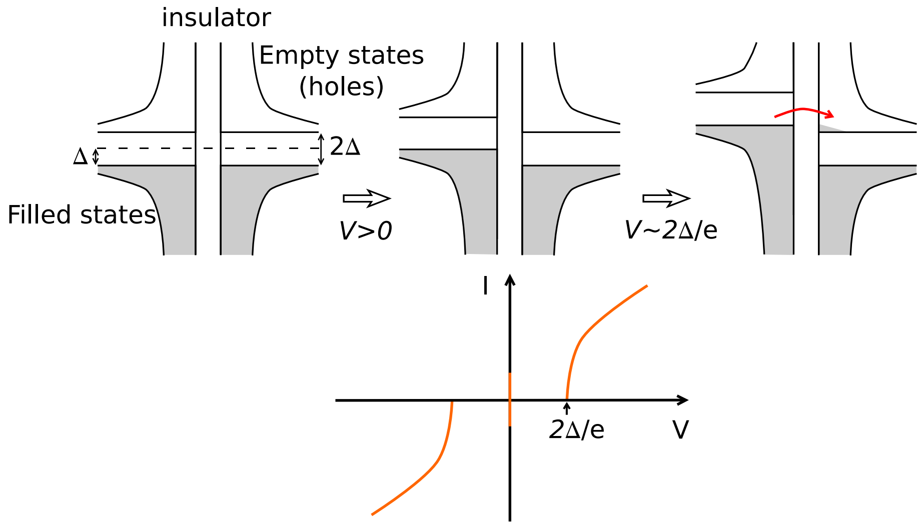

Figure 2.16 – Representation of the Giaever tunneling effect in a Superconductor-Insulator-Superconductor (SIS) Junction with the trend of the density of states at increasing voltage V (top three panels) and the characteristic $I - V$ curve of the system. The superfluid gap Δ renormalizes the density of states at the Fermi energy level (dashed line) of the normal Fermi gas (top-left panel), both for the filled states (gray area) and for the holes (white area). With no bias field, current may flow due to the DC Josephson effect, resulting in the peak (orange central line) at $V = 0$ of the $I - V$ curve. If a current is applied the filled state level of the first reservoirs is brought out of resonance with the second one. Due to the superfluid gap, there is an avoided region for electrons on top of the last filled states of size 2Δ, resulting in a suppression of the DC current. When the voltage V brings the filled states of the first reservoir at the empty states level of the second, a thermal current flows due to newly available states. For large voltages, the usual ohmic flow is recovered. In a Superconductor-Insultor-Normal metal (SIN) junction, we would get a slightly different $I - V$ curve, with the absence of the $V = 0$ current peak associated to the DC Josephson effect and the shift of the onset of the normal current at a value of Δ/e, since the normal state has no gap.

pair-breaking effects would set in, resulting in an onset of a normal current among the two sites of the junction, completely washing out any quantum non-linear effect. In solid state, this phenomenon is usually called Giaver tunneling (see fig.2.16) and is a valuable resource for measuring the superfluid gap, since the normal current sets in when the potential energy across the junction matches the superfluid gap or twice its value [39, 78].

Instabilities of the superflow and vortex creation

In the MQST regime, the relative phase dynamics is governed by phase slips. In a genuine two-mode picture, any 2π phase slips would correspond to the creation of a soliton among the two condensate, with a periodic creation and annihilation of this inside the barrier. In a more realistic three-dimensional junction the topological excitation with the lowest energy would be a vortex ring. The regime where these topological excitations are created is that of high barriers, meaning a strong reduction of the superfluid density in the link. This results in a lowering of the superfluid critical velocity inside the barrier. When this becomes comparable to the superflow velocity through the barrier, the creation of these topological defects becomes energetically favored [79]. Considering the case of cold atoms, these defects would start nucleating at the edge of the cloud, where the density is lower, while shrinking towards the center and there annihilating [80, 81]. This would result in a complete phase-slip, with an overall quantized drop of the superflow velocity, similarly to the case of helium [6]. However, small imperfections and asymmetries in the trap may cause vortices to not fully perform a complete phase-slip inside of the barrier and to escape from this and to propagate into the superfluid bulk [80], providing a dissipative channel, where damping and decoherence may eliminate the MQST phase, similarly to the effect that the current of non-condensed particles would have on the coherent tunneling dynamics [72].

2.4.2 Ferromagnetism in normal Fermi gases with repulsive interactions

Magnetism represents, together with superconductivity, a fundamental phenomenon characterizing a wealth of many-body fermionic systems. Unlike superfluidity, magnetism requires strong repulsions to occur. As a consequence of electronic interactions, many condensed matter systems, from metals to insulators, may undergo a magnetic phase transition below a certain critical temperature T_C, the Curie temperature [21], where ordered spin patterns would spontaneously create, even in the absence of an external magnetic field.

In certain systems, called ferromagnets, neighboring spins prefer a parallel orientation, creating a non-vanishing local magnetization. In antiferromagnets, antiparallel alignment is preferred, leading to a zero net magnetization, though featuring strong spin up-down correlations, hence magnetic order. In both cases, magnetic properties require strong interactions to show up. Consequently, magnetism is not a weak coupling problem and its theoretical description is notoriously difficult and challenging.

A notable theoretical model for the description of magnetic phases is represented by the Stoner model for itinerant ferromagnets, first introduced to describe the behavior of d- and f-metallic elements, such as iron or nickel. Similarly to the Heisenberg or Hubbard pictures [82] for electrons pinned on lattice sites, the Stoner model [9] describes mobile and delocalized magnetic moments that, because of the competition between screened short-ranged repulsive interactions and Fermi pressure, may arrange spins to acquire a non-vanishing magnetization. Within his model, Stoner found out that in a homogeneous system with continuous symmetry (i.e. with no lattice), by turning on interactions the system may undergo a quantum phase transition from an unmagnetized sample to a partially polarized one and then, for even larger interactions, to a fully polarized one, as depicted in fig.2.17. Nowadays, it is clear that Stoner mean-field model can only hold at the qualitative level, but the possibility of a ferromagnetic transition driven by short-ranged repulsion between itinerant fermions is confirmed by more rigorous approaches [83]. Despite strong experimental advances in solid-state physics for disclosing the properties of this magnetic phase, the unavoidable presence of impurities and disorder and the complex band structure of metals make comparison among experiments and Stoner's initial scenario a still unresolved challenge. Consequently, there is still not an unanimous consensus whether or not a homogeneous system, as originally envisioned by Stoner, can turn ferromagnetic.

The original Stoner model can be introduced considering the Hamiltonian for N electrons of the form:

$$\hat{H} = \sum_{i=1}^{N} \frac{p_i^2}{2m} + \frac{4\pi a\hbar^2}{m} \sum_{i<j} \delta(r_i - r_j) \frac{\partial}{\partial r_{ij}} r_{ij} \tag{2.38}$$

where opposite spin $\sigma = \uparrow, \downarrow$ particles may interact via a general short-ranged pseudopotential, whose interaction strength is parametrized by the usual scattering length a.

Using a short-ranged potential is a convenient approximation even for describing electronic interactions in solids, since the whole metallic state screens the Coulomb potential, exponentially cutting off its long-range behavior.

This allows to write down the energy at first order in interactions as:

$$E = \sum_{\sigma=\uparrow,\downarrow} \frac{3}{5} E_{F,\sigma} n_\sigma + \frac{4\pi a\hbar^2 V}{m} n_\uparrow n_\downarrow \tag{2.39}$$

having defined the spin density $n_\sigma = N_\sigma/V$ and the Fermi energy $E_{F,\sigma} = \frac{\hbar^2 k_{F,\sigma}^2}{2m}$. The first term in eq.(2.39) represents the kinetic energy, while the second the interaction one.

Introducing $y = N_\uparrow/N$, the expression for the energy reads as:

$$E = \frac{3}{5} E_F \left((1-y)^{5/3} + y^{5/3} \right) + \frac{4}{3\pi} k_F a E_F y(1-y) \tag{2.40}$$

where k_F and E_F are now the Fermi wavevector and energy of a single component Fermi gas with density $n = \frac{N_\uparrow + N_\downarrow}{V}$ and $k_F^3 = 6\pi^2 n$. Among the single-component and the two-components Fermi gases, the relation $k_F = 2^{1/3} k_{F,\sigma}$ holds. It should be noticed the invariance of eq.(2.40) under the transformation $y \leftrightarrow 1-y$.

By minimizing the total energy as a function of y, we are left with three possible scenarios [21], also depicted in fig.2.17:

- for $k_{F,\sigma} a < \pi/2$, the minimum energy is achieved for $y = 1/2$, meaning zero net magnetization
- for $\pi/2 < k_{F,\sigma} a < 3\pi/2^{7/3}$, the $y = 1/2$ point becomes unstable and the system becomes partially polarized

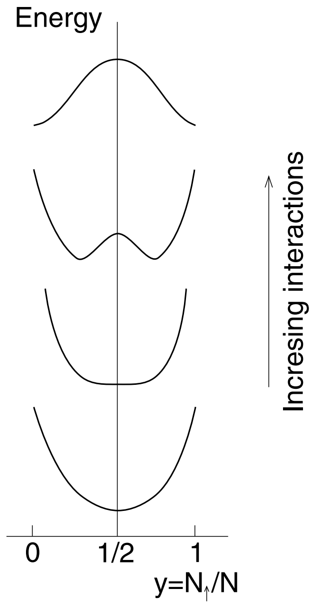

Figure 2.17 – Evolution of the energy at constant volume for different interaction strengths. For weak interactions, the energy has a stable minimum at $y = 1/2$. Progressively increasing interactions (from bottom to top) makes the point $y = 1/2$ unstable, with the creation of two minima, symmetric with respect to $y = 1/2$. For large enough interactions, the system is in a saturated ferromagnetic state (minima in $y = 0$ and $y = 1$). After [84].

- for $k_{F,\sigma}a > 3\pi/2^{7/3}$, the system becomes fully polarized (i.e. $y = 0$ or $y = 1$) and the ferromagnetic state gets saturated

The mean-field Stoner model predicts a transition to the ferromagnetic state for $k_{F,\sigma}a \geq \pi/2$, which can be translated into the condition:

$$g(k_{F,\sigma})U \geq 1 \tag{2.41}$$

where $g(k_{F,\sigma}) = mk_{F,\sigma}/(2\pi^2\hbar^2)$ is the density of states at the Fermi surface and $U = 4\pi\hbar^2 a/m$ is the strength of the contact potential.
Furthermore, the mathematical translation of the instability of the $y = 1/2$ point at the critical strength $k_{F,\sigma}a = \pi/2$ is expressed by the thermodynamical spin susceptibility χ_s defined as:

$$\frac{1}{\chi_s} = \frac{\partial^2 E}{\partial y^2} \tag{2.42}$$

where E is the system free energy.
At the critical point, χ_s diverges. This is the thermodynamical variable which quantifies the tendency of the system to turn ferromagnetic and a fundamental parameter to be measured, being related to the spin fluctuations at the phase transition.
Nevertheless, the very same presence of a non-vanishing coupling term ($k_{F,\sigma}a \geq 1$) makes this perturbative treatment unreliable in the quantitative determination of the critical pa-

rameters of this phase transition. For instance, the Stoner model predicts for any temperature range a second order phase transition, while more sophisticated theories [85], which take into account particle-hole excitations coupled to magnetization [21, 86] turn the phase to be first order at temperatures $T < 0.2T_F$, as experimentally confirmed in investigations over ultra clean samples [87]. Inclouding higher order perturbative terms in the mean-field Stoner picture reduces the critical interaction strength and actually drives the phase transition to be of first order at low temperatures [88].

However, Quantum Monte Carlo (QMC) numerical experiments are at present the more sophisticated theoretical tool for targeting this problem in mixtures of repulsive Fermi gases. In these studies the pairwise interaction is modeled by using both purely repulsive (i.e. Hard Sphere and Soft Sphere) and attractive (i.e. Square Well or Pöschl-Teller) potentials. Provided the potential to be sufficiently short-range, the microscopic details of the chosen potential do not affect the overall (long-range) physical picture. As seen in section 2.2.1, this assumption is valid for attractive potentials, contrary to repulsive ones. However, for both the considered case, QMC calculations show the Stoner instability to take place at $T = 0$ at a critical interaction parameter of the order of $0.8 \leq k_{F,\sigma}a \leq 0.9$ [29, 89], significantly lower that any perturbative result from the mean-field model.

In this framework, ultracold atomic gases are an ideal platform for comparison with state-of-the-art theoretical models. The unprecedented cleanliness of these systems, combined with the extreme control over interactions, temperature and geometry would allow the exploration of an ideal phase-space, unlike conventional condensed matter systems. One important difference among quantum gases experiments and solid-state one is that spin-changing collisions are not allowed, making each spin population N_σ conserved. Hence, spontaneous magnetization is translated into the development of phase separated domains with unequal spin densities. Ideally, in a quantum gas simulation, above the critical interaction there would be a spatial separation of domains with unequal spin reducing the interaction energy from the overlap, as depicted in fig.2.18.

As anticipated, this issue can be addressed in normal atomic Fermi gases on the upper branch of a Feshbach resonance. While existing on this excited level, the gas has no pairing and the pairwise interaction is genuinely repulsive. A successful platform for understanding the properties of these atomic Fermi gas with tunable repulsive interactions is given by Landau's Fermi liquid theory. In the following a basic introduction to this theory will be given.

Basics of Landau's Fermi liquid theory: quasiparticles and Stoner instability

When interactions are "adiabatically" [90] turned on in a non-interacting Fermi gas, the eigenstates of the interacting case have a one-to-one correspondence with the non-

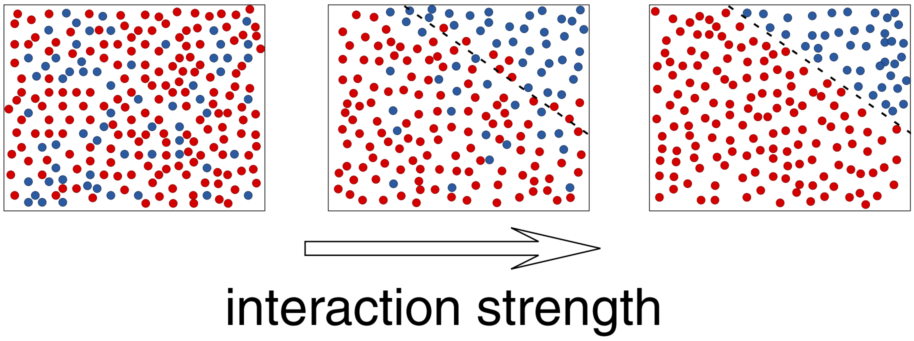

Figure 2.18 – Representation of the Stoner phase transition in repulsive atomic Fermi gases. For vanishing interactions (left panel) the system is in a paramagnetic phase, with random spatial spin distribution. Increasing interactions, the paramagnetic phase becomes unstable and, spontaneously, phase separated spin domains start to appear (center) with non-zero local magnetization. For very strong repulsion (right), even a single spin impurity is energetically not allowed. The dashed line represents a domain wall.

interacting ones. This is the basic idea behind Landau's picture of Fermi liquids [91, 92]. Landau realized that, in the limit of weak excitations, the single-particle occupation numbers $\mathcal{N}_{k\sigma}$ of the non-interacting state evolve extremely smoothly even for strong interactions. Consequently, the same set of $\mathcal{N}_{k\sigma}$s can be used as approximate quantum numbers for the interacting system [90]. This allows to threat the excitations of a Fermi liquid as *quasiparticles*, which, despite some renormalized properties, behave like non-interacting elementary particles.

Consider for example the ground-state of an ideal non-interacting Fermi gas at $T = 0$. An elementary excitation of the system will be the addition of a particle at momentum $k > k_F$, since below the Fermi momentum any state is occupied. This excitation would be itself an eigenstate of the system, thus having infinite lifetime. Suppose now to take the same system and, as envisioned by Landau, smoothly turn on interactions. The free eigenstates will start scattering into the new ground state and the excitation would be properly defined only if surviving for a sufficiently long time.

Taking into account the *Pauli exclusion principle* and conservation laws, the available states for scattering of the quasiparticles lie within a shell of thickness $|k - k_F|$ around the Fermi surface. Consequently, its scattering probability or inverse lifetime would be proportional to $1/\tau \propto (k - k_F)^2$. Hence, quasiparticles can be treated as an approximate eigenstate only close to the Fermi surface.

Here, the Landau's Ansatz for the quasiparticles energy functional can be written as:

$$E[\mathcal{N}_{k,\sigma}] = E_0 + \sum_{k\sigma} \mathcal{E}_k \delta\mathcal{N}_{k\sigma} + \frac{1}{2} \sum_{k\sigma,k'\sigma'} f_{k\sigma,k'\sigma'} \delta\mathcal{N}_{k\sigma} \delta\mathcal{N}_{k',\sigma'} \tag{2.43}$$

where E_0 is the ground state energy, $f_{k\sigma,k'\sigma'}$ the Landau interaction function and $\delta\mathcal{N}_{k\sigma} = \mathcal{N}_{k\sigma} - \mathcal{N}^0_{k\sigma}$ is the difference among the quasiparticles distribution function and that of an ideal Fermi gas at $T = 0$.

The quasiparticle energy can be evaluated as:

$$\mathcal{E}_k = \left(\frac{\partial E}{\partial \mathcal{N}_{k\sigma}}\right)_{\mathcal{N}_{k\sigma}=\mathcal{N}^0_{k\sigma}} \tag{2.44}$$

At the Fermi energy with chemical potential μ, this gives:

$$\mathcal{E}_k = \mu + \frac{\hbar^2 k_F}{m^*}(k - k_F) \tag{2.45}$$

where $m^* = \hbar^2 k_F / |\frac{\partial \mathcal{E}_k}{\partial k}|_{k=k_F}$ is the effective mass.
The latter is one of the fundamental properties of the quasiparticle, which depends upon the interaction function. One may think that interactions dress a certain particle with the others in its surroundings, creating an effective particle dragged by all the others while it is moving. This would result in an effective mass different from the bare one, similarly to what happens for electrons on a lattice, but with a renormalization now driven by interactions.
The interaction function $f_{k\sigma,k'\sigma'}$ can instead be considered as the interaction energy among quasiparticles. From it, one can derive the expression for the Landau parameters:

$$F_l^{s,a} = \frac{VN(\mu)m^*}{2m}\int \frac{d\Omega}{\Omega}[f_{\uparrow\uparrow}(\cos\theta) \pm f_{\uparrow\downarrow}(\cos\theta)]\mathcal{P}_l(\cos\theta) \tag{2.46}$$

where Ω is the solid angle and $\mathcal{P}_l(\cos\theta)$ the l-order Legendre polynomial. The label s and a means symmetric or antisymmetric respect to the angular dependence over the interaction function, that here have been reduced to $f_{k\sigma,k'\sigma'} \simeq f_{\sigma\sigma'}(\cos\theta)$, due to the spherical symmetries of the quasiparticles distribution $\mathcal{N}_{k\sigma}$.
When using the Landau parameters, the expression for many of the quasiparticle properties can be expressed in simple and elegant formulas. For instance, the expression for the effective mass reads as:

$$\frac{m^*}{m} = 1 + F_1^s \tag{2.47}$$

or again the one of the spin susceptibility becomes:

$$\frac{\chi_s}{\chi_0} = \frac{m^*}{m}\frac{1}{1+F_0^a} \tag{2.48}$$

where χ_0 is the spin susceptibility of the non-interacting gas. In the case of a ferromagnetic transition, χ_s diverges for $F_0^a \to -1$.
The previous arguments introduced the quasiparticle properties from a sort of macroscopic point of view. More and deeper insights can instead be inferred by a rigorous microscopic treatment of the problem, dealing with the Green's function $G(\mathbf{k}, \omega)$ of the system [93, 94]. This can be generally expressed as:

$$G(\mathbf{k}, \omega) = \frac{1}{\hbar\omega - \epsilon_k - \Sigma(\mathbf{k}, \omega)} \tag{2.49}$$

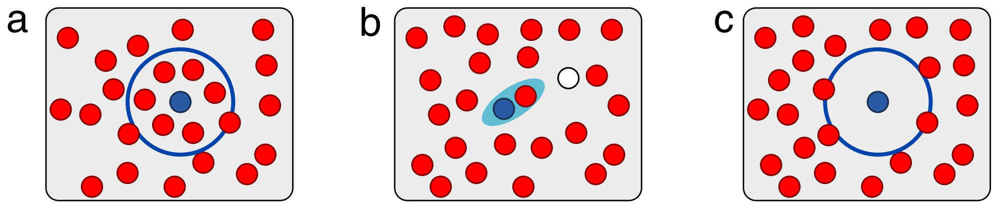

Figure 2.19 – Quasiparticles for an impurity (blue circles) immersed in a Fermi sea (red circles). Sketch of: a) Attractive polaron, b) molecule + hole, c) repulsive polaron

where we have introduced the self-energy $\Sigma(\mathbf{k},\omega)$ which encodes the effects of the interactions on the correlations of the many-body state.

The relevant problem for our experimental investigation is that of Fermi gases with spin polarization, the simplest case being the one of a $\downarrow$ particle immersed in a $\uparrow$ Fermi sea. The resulting quasiparticle in this framework is usually called polaron [95]. The properties of these quasiparticles are usually described by the spectral function $A(\mathbf{k},\omega)$. In the non-interacting regime the spectral function is a comb of delta functions, peaked at the eigenstates ϵ_k of the problem. When interactions are considered, the function $A(\mathbf{k},\omega)$ is still peaked at some resonance frequencies, generally featuring a Lorentzian shape. The central position of the Lorentzian is expressed as $\xi_k = \epsilon_k + \mathrm{Re}[\Sigma(\mathbf{k},\omega)]$ and is interpreted as the "new" quasiparticle energy. The width of the distribution is instead equivalent to the imaginary part of the self-energy $\mathrm{Im}[\Sigma(\mathbf{k},\omega)]$, which defines the inverse lifetime Γ_k of the quasiparticle.

In the many-body problem of a $\downarrow$ impurity in a $\uparrow$ Fermi sea, the spectral function depending on the interaction parameter $1/k_F a$ is strongly peaked around two branches, similarly to the aforementioned case of the two-body problem in a box. The lowest of these branches describes an impurity attracting a cloud of majority atoms [21] (see fig2.19) and for this the associated quasiparticle is called *attractive polaron*. The energy E_- of this branch versus $1/k_F a$ is reported in fig.2.20, together with the trend of the other higher branch energy E_+. This upper branch describes an impurity repelling the majority components and it is the many-body analogue of the excited state of the two-body solution. For this reason, the quasiparticles on this branch are called *repulsive polarons*.

Differently from the two-body problem, the many-body solution predicts an increasing decay towards resonance of the upper branch, making eventually the repulsive polaron ill-defined [21]. Moreover, a continuum of states between the two branches is expected (see fig.2.20). Considering the BEC limit, it is also possible that the impurity particle binds with one majority component, taken from any place in the Fermi sea. This leads to the creation of a dimer, or dressed molecule, together with a hole. The resulting excitation has a spectral width of the order of the Fermi energy E_F [21], becoming the true ground state in the BEC limit ($1/k_F a > 1$). The experimental proof of this scenario has been shown in

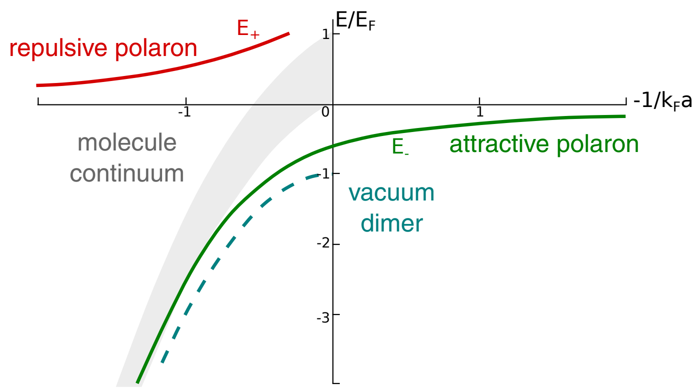

Figure 2.20 – Representation of the lower (green) and upper (red) branches, together with the molecule-hole continuum for a broad Feshbach resonance. After [21].

ref.[96].

The decaying channels for the repulsive polaron are provided by both the attractive polaron branch and the molecule-hole continuum. Two-body processes lead to the formation of attractive polarons, while three-body processes to the formation of a molecule and a hole excitation, the latter decaying channel becoming dominant only in the BEC limit.

The stability of the ferromagnetic phase is connected to the properties of these quasiparticles. For instance, in the usual case of a ↓ impurity interacting with a Fermi gas of ↑ particles with a Fermi energy $E_{F\uparrow}$, if the energy of the polaron E_+ is higher than $E_{F\uparrow}$, the diffusion of the ↓ particle in the ↑ Fermi sea will be impeded, favoring a phase separation among the unequal spins [97].

The most important question is however related to the intrinsic metastability of the upper-branch, in particular whether the lifetime of such a many-body state is sufficient to establish ferromagnetic correlations in the system.

CHAPTER 3

Experimental Setup

This chapter covers the description of the machine used to obtain and manipulate ultracold Fermi gases of Lithium 6. The apparatus is composed of an Ultra-High-Vacuum (UHV) system (see fig.3.1) to isolate cold atoms from hot thermal background ones. The main element of this system, the science chamber, has large optical access to perform high-resolution imaging of the atomic cloud and to imprint arbitrary optical potentials.
A brief introduction to laser cooling and trapping will be given, focusing on the laser sources used in our apparatus.

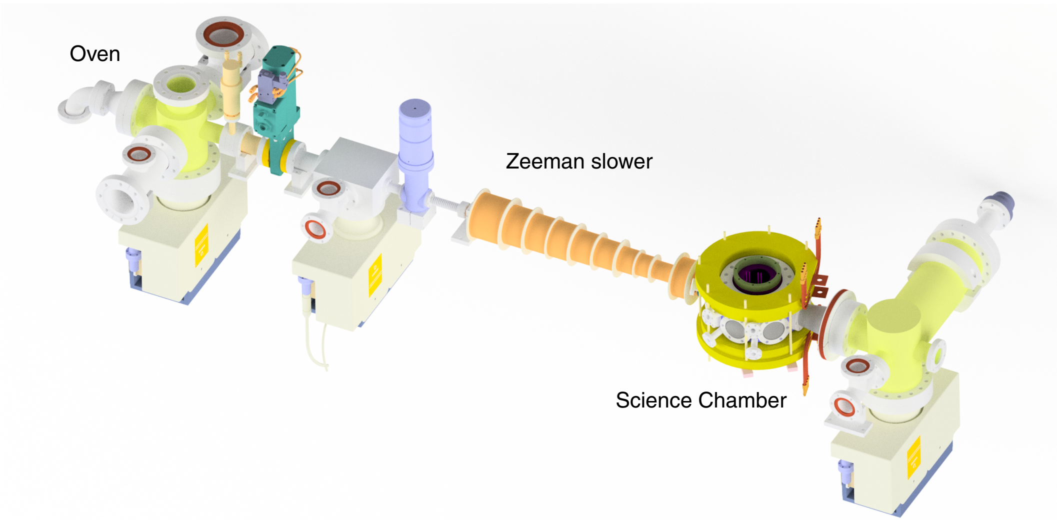

Figure 3.1 – View of the overall UHV apparatus for isolating the cold atoms from the background. Atoms are initially held in the oven and then enter though a nozzle in the main UHV system. Decelaration by the Zeeman slower allows atoms to be captured inside the Science chamber.

3.1 Overview of the vacuum system

Isolation from thermal background atoms is a mandatory task for efficiently perform cold atoms experiments. A pressure below 10^{-11} mBar is generally required into the science chamber to guarantee a sufficient long lifetime to the atomic sample. Atoms enter into the science chamber coming from an effusive oven, where a sufficient flux of ^{6}Li is produced at a temperature above 400°C. To avoid pressure contamination in the science chamber from the oven, an intermediate differential pumping stage has been placed among the two. An overview of these three main different parts, the oven, the differential pumping stage and the science chamber will be given in the following sections.

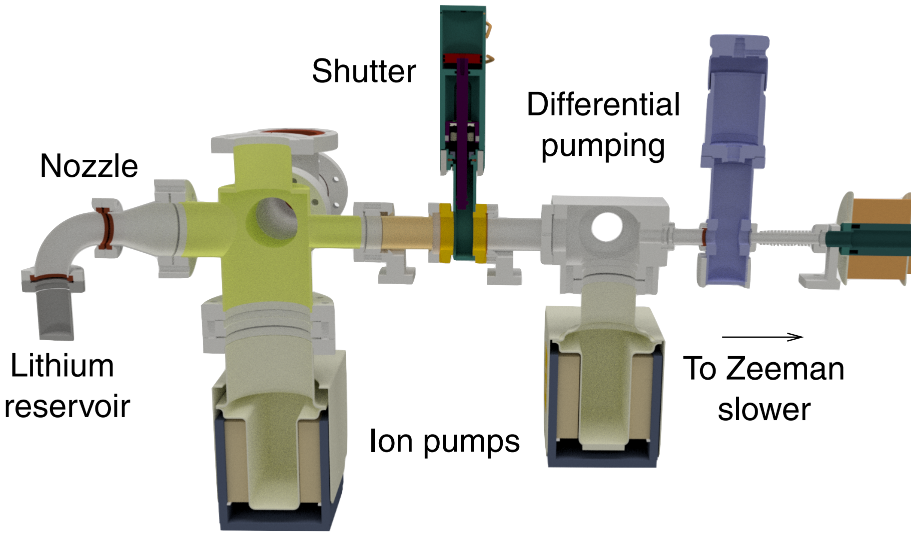

Figure 3.2 – Section-view of the oven chamber. Lithium is held in the reservoir on the left and enters the apparatus from the nozzle, which provides a first collimation of the atomic beam. After passing through the differential pumping stage, atoms are decelarated by the Zeeman slower.

3.1.1 The oven and the differential pumping stage

Lithium is solid at room temperature. To extract a significant vapor pressure from the solid metal, this is heated up till a temperature over 400°C. In our oven a sample of artificially enriched ^{6}Li is held in a cup at a temperature around 420°C. As shown in fig.3.2, a circular nozzle connects the cup to the main oven chamber, collimating the vapor traveling into the system. To avoid sticking and solidification of Lithium onto the nozzle, this is generally held at a temperature of 460°C. To reduce pressure due to high temperatures, a *Agilent* 75 l/s ion pump is placed below the oven chamber. For further collimating the atomic beam, a copper cold finger is placed after the nozzle. On the other side, an electric gate valve disconnects the oven from the rest of the apparatus. This will allow refilling of the atomic sample, once the oven runs out of it, without affecting the pressure in the science chamber.

A sufficient pressure gradient among the oven and the science chamber is provided by a differential pumping stage. This stage is composed by two tubes, with a diameter of 4.6

mm and 7.7 mm and a length of 12.6 cm and 6.35 cm, respectively. The low conductance among the tubes does not allow the oven pressure to contaminate the science chamber. Moreover, another *Agilent* ion pump of 55 l/s capacity has been placed among the tubes to further decrease their conductance. This stage connects through a manual gate valve to the Zeeman slower tube and then to the science chamber.

3.1.2 Science chamber

All cooling stages, from the magneto-optical trap (MOT) to the evaporative cooling, and all of the physical experiments are performed in the same science chamber. It is a custom octagonal stainless-steal cell from *Kimball Physics* (see fig.3.3). Its several windows allow good optical access among different directions. On the vertical axis, it is equipped with two large re-entrant viewports. These are silica windows made by *Ukaea* with a 60 mm diameter and a thickness of 6 mm. Their relative distance in vacuum is 25.4 mm. This allows to have a large numerical aperture and to place a high resolution imaging system close to the atoms. A sufficiently low pressure in the chamber is achieved by placing another *Agilent* 75 l/s ion pump after the science cell. To further reduce the pressure, the chamber's walls have been coated with a non-evaporative getter (NEG) coating. This coating is thermally activated during the bake out and acts as an additional titanium sublimation pump, sticking mainly to H_2 molecules, which are weakly affected by ion

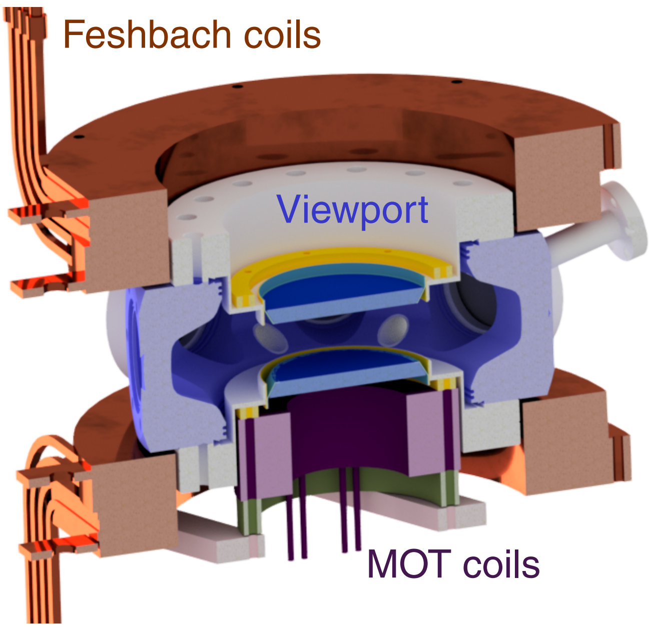

Figure 3.3 – Section of our custom chamber, with addition of some magnetic field coils. The re-entrant viewports are shown in dark blue, the Feshbach coils in brown and the MOT coils (for clarity only at the bottom) in purple.

pumps. We achieve pressure of the order of 10^{-12} mBar in the science chamber after activation of NEG coating.

3.2 Laser sources

In atomic physics experiments, laser beams can be used for creating both dissipative and confining forces. The dissipative one relies on the absorption and scattering of near resonant light with the atomic transition. Photons with energy below the atomic transition can be absorbed by counter propagating atoms thanks to the Doppler effect. Consequent spontaneous emission of absorbed photons at the atomic transition determines a reduction of atoms' energy and of their temperature. Inhomogeneous far-detuned laser beams can instead be used to create conservative potentials to trap and confine atoms in different geometries. In our experiment we rely on both kinds of atom-photon interaction and a description of the laser system to control them will be given.

3.2.1 Lithium 6 laser system

The hyper-fine structure of ^{6}Li is reported in appendix A, with indications of all relevant atomic levels. The hyper-fine splitting in the ground state manifold is just 228 MHz large. This allows to obtain both cooling and repumper lights from the same source. Our main laser is a *Toptica* TA-Pro, set to work at the D_2 transition with a wavelength around 670.977 nm. To increase the available power, two MOPA amplifier always by *Toptica* are used, one for the cooling light and the other for the repumper. Each one gives an output power around 360 mW. The amplifiers are lodged on a different optical table respect to the TA-Pro's one and a single mode polarization maintaining optical fiber connects the two. An Acousto-Optical Modulators (AOMs) scheme on the amplifiers' table produces all relevant frequencies for both cooling and imaging of the atoms. The beams are then brought by other single mode polarization maintaining optical fibers onto the experimental chamber. On the same table of the D_2 TA-Pro, we placed another TA-Pro working on the D_1 transition, which is essential for our cooling strategy. The shift among this two optical transitions is just 10 GHz large. Therefore, we cannot simultaneously inject the MOPAs with the two wavelengths. An electronic switch selectively controls which light injects the MOPAs. A sketch of the scheme is shown in figure 3.4.

Laser Locking

We use Doppler-free saturation absorption spectroscopy to lock the two TA-Pros on atomic references. The reference beams are made pass through an heat pipe where a sample of

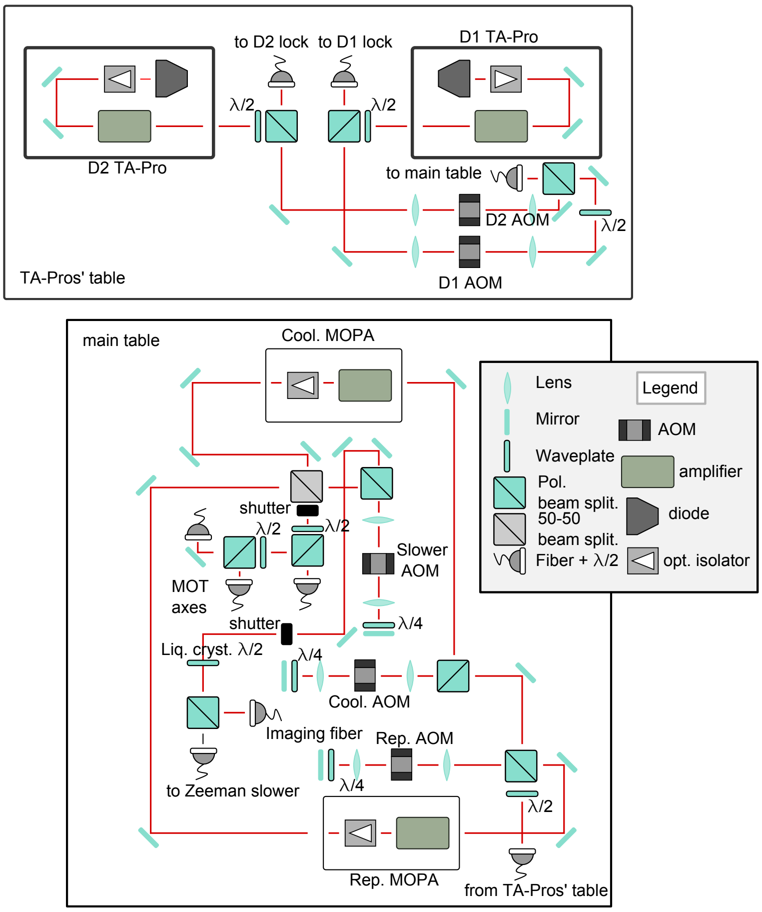

Figure 3.4 – Sketch of the ^{6}Li laser system for producing the cooling and repumper lights, on both the D_1 and D_2 transition.

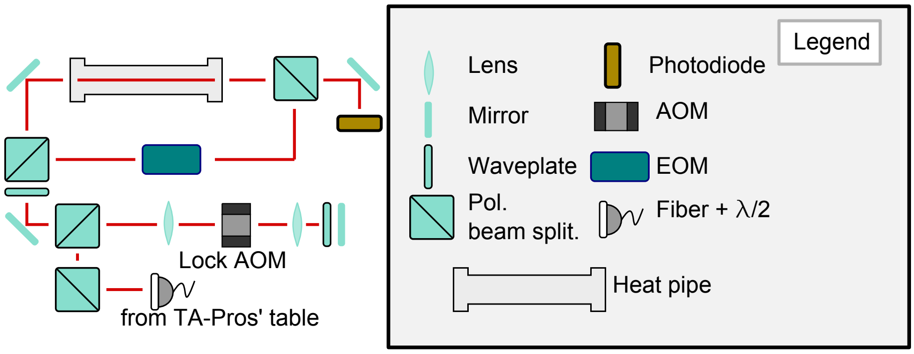

Figure 3.5 – Sketch of the locking scheme for the D_2 TA-Pro. The EOM carries the modulation without affecting the main laser.

enriched ^{6}Li is held at a temperature around 330°C. The D_1 laser is locked using conventional modulation transfer spectroscopy, adding a time-dependent current modulation to the diode current. On the D_2 laser we instead apply modulation transfer spectroscopy using an Electro-Optical Modulator (EOM) at a frequency of 12.5 MHz. The EOM's high frequency allows to cut off all noise in the kiloHertz regime and to have a more robust locking. Moreover, the modulation for the locking scheme is carried by a side beam, without perturbing the diode current with an additional modulation. The D_2 laser is locked on the closed $S_{1/2}$ F=3/2 $\rightarrow$ $P_{3/2}$ F=5/2 transition, while the D_1 laser is locked on the crossover of the $P_{1/2}$ F=3/2 transition of the D_1 manifold. A representation of the D_2 locking optics is shown in figure 3.5.

Laser Cooling: Zeeman slower and MOT lights

A sketch of the AOMs scheme used to generate the right frequencies is reported in figure 3.4. The light coming from the TA-Pros' table is first split in two paths, one for the cooling and one for the repumper. For the cooling we placed a double-pass blue-detuning AOM with a center frequency around 90 MHz before injecting the MOPA. For the repumper light we use the same scheme with a different AOM, with a center frequency around 200 MHz. Lights coming from MOPAs are overlapped and then split again in two paths, one for the Zeeman slower and one for the MOT beams. The MOT light is simply split in three different paths, for the tree spatial directions of the MOT beams. On any of them a polarization maintaining optical fiber is injected to reach the science chamber. For the Zeeman slower instead, we use a double-pass red-detuning AOM with a center frequency around 220 MHz and then we inject another optical fiber to reach the UHV apparatus.

Zero field and High field imaging

Our experiments are performed at different values of the magnetic field. For compensate the Zeeman shift, we use another AOMs scheme to generate probe beams with different frequencies. Since the Zeeman slower light is already 400 MHz red-detuned, we derive our imaging setup from it. We placed a liquid crystal waveplate and a polarization beam splitter on the Zeeman slower beam. The liquid crystal waveplate can change the polarization of the light passing through it as a function of the applied voltage. After the loading of the atoms, the Zeeman slower is turned off and the liquid crystal waveplate rotates of 90°the beam polarization. The light is so reflected by the following beam splitter and does not inject anymore the Zeeman slower fiber. A different polarization maintaining fiber brings this light to a different breadboard. With a combination of waveplate and AOMs we can selectively generate resonant light for three different magnetic field configuration. For zero-field imaging, the beam passes through a double-pass blue-detuning AOM for compensating the Zeeman slower AOM. For imaging at around 300 G, we use the shift given by the AOM Zeeman slower and no other manipulation is needed. As it will be explained later, the normal Fermi gas is generally produced at 300 G. To explore the Feshbach resonance at around 800 G, we use instead a double-pass red detuning AOM at 200 MHz. The probe beams are brought to the science chamber by other polarization maintaining optical fibers.

3.2.2 Optical dipole traps

Light can also be used to create conservative potentials for neutral atoms [98]. The oscillating electric field $\mathbf{E}$ of the laser can induce onto the atoms a dipole moment $\mathbf{p}$ of the form:

$$\mathbf{p} = \alpha \mathbf{E} \tag{3.1}$$

where α is the atomic polarizability. The electric field acts as a driving field creating an interaction potential of the form:

$$U_{\text{dip}} = -\frac{1}{2}\langle \mathbf{p} \cdot \mathbf{E} \rangle = -\frac{1}{2\epsilon_0 c}\text{Re}(\alpha) I(\mathbf{r}) \tag{3.2}$$

However, the oscillating atoms absorb some power from the driving field which is re-emitted as dipole radiation. This process is related to the imaginary part of the polarizability and the scattering rate of it can be described by the relation:

$$\Gamma_{\text{sc}} = \frac{\langle \mathbf{p} \cdot \mathbf{E} \rangle}{\hbar\omega} = \frac{1}{\hbar\epsilon_0 c}\text{Im}(\alpha) I(\mathbf{r}) \tag{3.3}$$

where ω is the frequency of the laser light.
In the assumption of a two-level atomic system, we can approximate the previous relations

with the following formulas:

$$U_{\mathrm{dip}} = \frac{3\pi c^2}{2\omega_0^3}\frac{\Gamma}{\Delta}I(\mathbf{r}) \tag{3.4}$$

$$\Gamma_{\mathrm{sc}} = \frac{3\pi c^2}{2\hbar\omega_0^3}\left(\frac{\Gamma}{\Delta}\right)^2 I(\mathbf{r}) \tag{3.5}$$

where Γ is the linewidth of the transition and $\Delta = \omega - \omega_0$ is the detuning among the frequency ω of the laser and the atomic transition frequency ω_0.
The scattering rate scales as I/Δ^2, while the depth of the potential as I/Δ. Thus, largely detuned wavelengths are more suited for creating conservative potentials with low scattering rate. By changing the sign of the detuning Δ it is possible to have a confining potential ($\Delta < 0$, red-detuning) or a repulsive potential ($\Delta > 0$, blue-detuning). In the following sections the different laser beams used to shape optical traps will be described.

High power Optical Dipole Trap: IPG laser

To trap the atoms after the MOT phase we use a single focus Optical Dipole Trap (ODT), derived from an *IPG Photonics* laser. The maximum available power is around 200 W. The laser has a central wavelength of 1070 nm with almost a 3 nm broadening. To handle the *IPG* high power we use the optical scheme represented in figure 3.6. Because of the extremely high intensity, the *IPG* beam is collimated to a 1 mm waist before entering a single-pass AOM, reducing detrimental effects on the AOM crystal spot. Most of the *IPG* optical path is held in a box under a continuous flux of air, to avoid dust deposition on any optical element. The beam passes through a hole on one of the walls and then is brought to the science chamber and focused onto the atoms with a waist of 45 μm, both in the x and y direction. The beam passes through the cell from one of the MOT windows, with an angle of 7°respect to the MOT beam.
To stabilize the *IPG* power we take a transmitted fraction from a mirror after the box and focus it onto a photodiode (*Thorlabs* DET36A/M). The photodiode acts as the measurement channel for an analog PID controller (*SRS* SIM960). The PID controller, after calibration, compares the signal coming from the photodiode with the one coming from the CPU user. Thanks to a feedback loop it actively corrects the beam power.
At full power the *IPG* ODT has a depth of around 3-4 mK. This is needed to effectively trap atoms after the MOT stage, since the temperature is of the order of 400 μK. However, after the application of the D_1 cooling (see chapter 4), the drop in the atoms temperature allows to decrease the ODT power. Furthermore, this allows us to play another trick on our optical trapping strategy. Having more *IPG* power available, we apply a fast sinusoidal modulation to both the central frequency and the amplitude of the *IPG*'s AOM, to increase the trapping volume of the ODT. The frequency modulation (FM) changes the frequency

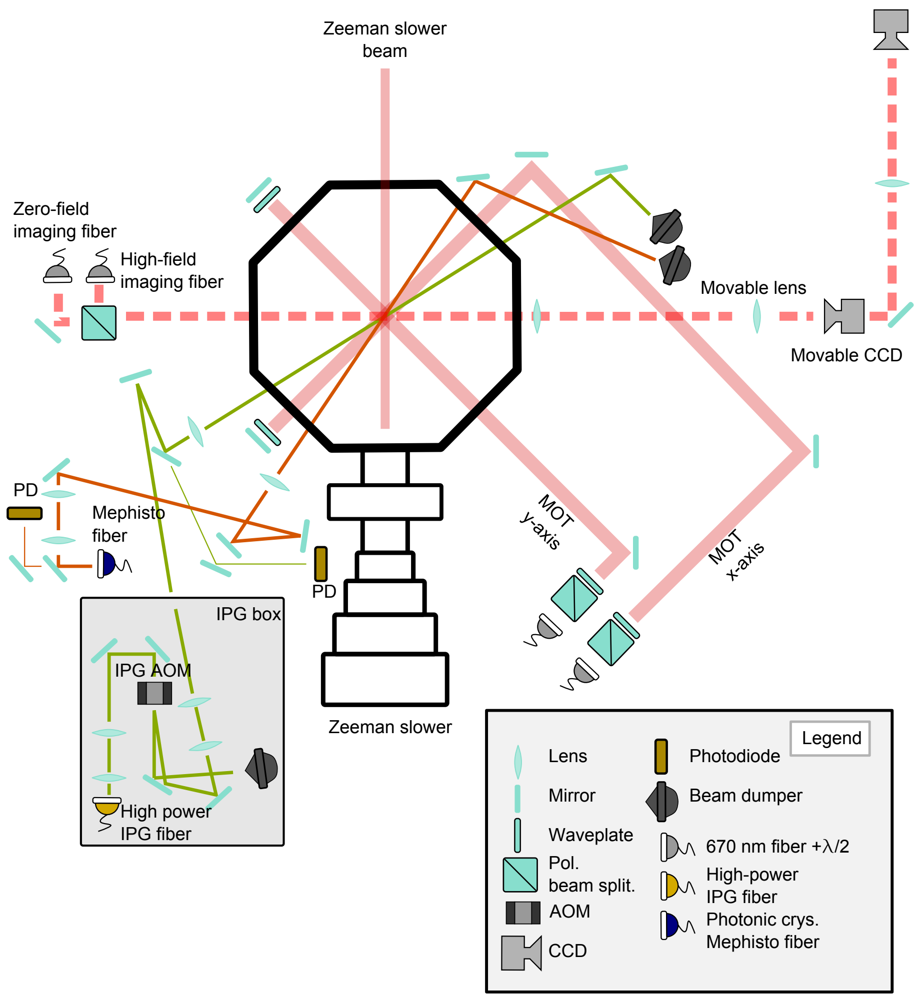

Figure 3.6 – Sketch of the optical scheme around the science chamber. The two horizontal MOT beams are shown in faded red, the IPG's in green and the Mephisto's in orange. The Zeeman slower beam is coming from above and is also shown in faded red, while the dotted lines are the imaging beams. The box where the IPG is brought towards the UHV apparatus is shown in the bottom left corner.

of the AOM oscillating crystal. This shift moves physically the position of the focused beam in the science chamber (fig. 3.7). If the frequency of this modulation is above the trapping frequencies, atoms experience a time-averaged dipole potential with a larger effective waist. We have set an FM frequency around 600 kHZ. While increasing the amplitude of the FM, we found the beam waist to be distorted, with a significant change from the typical gaussian profile 3.7. To correct for this, we apply also an amplitude modulation (AM) to the beam power, with a frequency twice the one of the FM (1.2 MHz) and a relative phase of $\pi/2$. The AM corrects for the deformation due to FM and restores a gaussian beam profile. At the maximum modulation, the beam waist on the x direction has a value around 85 μm. Both for the FM and AM, the frequency is well above the bandwidth of the PID ($\sim$ 100 kHz), and does not affect its feedback action. After application of D_1 cooling, the trap has a depth around 1 μK, even with the modulation on.

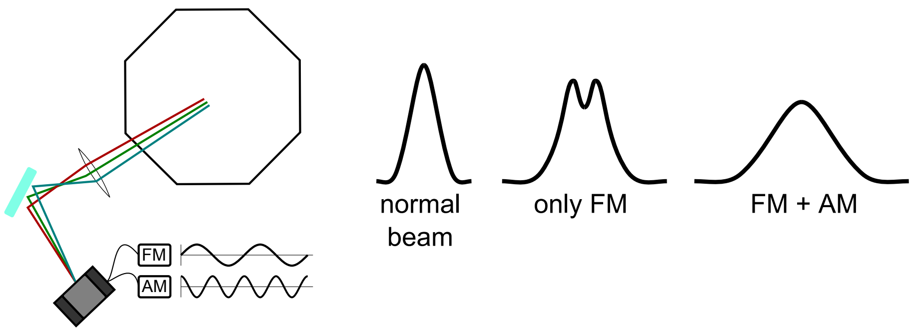

Figure 3.7 – Representation of the Frequency Modulation (FM) and of the Amplitude Modulation (FM) on the IPG AOM and their effect on the beam. The FM changes spatially the position of the IPG in the focus of the trap, but it distorts the beam shape. The AM corrects for the FM's distortion and helps recovering a gaussian beam with an enlarged waist.

Crossed Dipole Trap: Mephisto laser

To increase the axial confinement in our trap, in particular at low intensities of the IPG, we add a secondary ODT, derived from a *Mephisto* laser from *Innolight* at a wavelength of 1064 nm. The beam is focused onto the atoms with an angle of 14°respect to the *IPG beam*, with a circular waist of 45 μm. The *Mephisto* beam is brought by a *NKT Photonics* photonic crystals fiber close to the science chamber. As for the *IPG* beam, its power is stabilized with a PID feedback loop, taking the transmission from a mirror.

3.3 Magnetic fields

Different magnetic fields are needed during our experimental run. They are a necessary element for efficiently perform both laser and evaporative cooling and to explore the physics

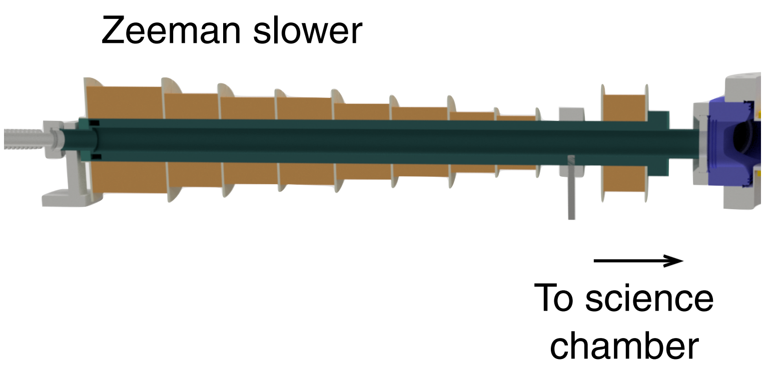

Figure 3.8 – Section view of the Zeeman slower. The magnetic coils are shown in brown.

behind Feshbach resonances. Apart from Zeeman slower ones, all coils are placed around the science chamber.

Zeeman Slower

The first combination of coils is the one of the Zeeman slower, used to decelerate atoms from the oven at a temperature around 400°. The Zeeman slower is a tube wrapped in coils (see fig.3.8), which create a spatially inhomogeneous magnetic field. The combined action of this field with a laser beam, counter propagating respect to the effusive atoms, decelerates them from a velocity of the order of 800 m/s till a value around 60 m/s, increasing the capture efficiency of the MOT. This magnetic field keeps the atoms in resonance with the counter propagating beam, compensating for the changes in the Doppler shift and allowing a continuous cooling. The shape of the required magnetic field can be found imposing the condition [99]:

$$\omega_L - \omega_0 + k_L v = \frac{\Delta E_{hs}(B)}{\hbar} \tag{3.6}$$

where ω_L is the beam frequency, ω_0 the atomic one at zero field and $\Delta E_{hs}(B)$ is the hyperfine splitting of the cooling transition, dependent on the magnetic field B. Since the ^{6}Li atom enters into the Paschen-Back regime at relatively low fields we can approximate $\Delta E_{hs}(B) = \mu_B B$. We obtain for the magnetic field the expression:

$$B = \frac{\hbar}{\mu_B}(\Delta_0 + k_L\sqrt{v_i^2 - 2az}) \tag{3.7}$$

where $\Delta_0 = \omega_L - \omega_0$, v_i represents the maximum velocity which is slowed down by the slower and a the deceleration, which can be evaluated by solving the optical Bloch equations [99].

For our slower, we have set $v_i = 830$ m/s, $\Delta_0 = -66.7\Gamma$, where Γ is the linewidth of the cooling transition, and an intensity close to the saturation one. The calculated magnetic field is reported in figure 3.9.

Our Zeeman slower is in a *spin-flip* configuration, since the magnetic field profile passes through zero. Because of this, we need some repumper light to recover atoms after depolarization. This configuration has two main advantages. First, the atoms, once exiting the slower, are off-resonance with the counter propagating beam, while traveling towards the science chamber. Second, the creation of such magnetic fields does not require high power consumption.

To match our theoretical calculations, we found the system of coils reported in the table 3.1 to be suitable.

The theoretical magnetic field generated by the coils is also reported in figure 3.9 and it

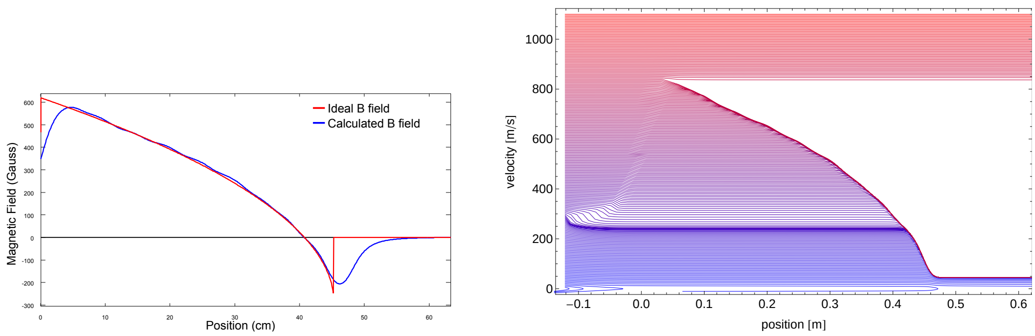

Figure 3.9 – Left panel: Comparison between the ideal magnetic field and the one calculated as superposition of the 9 coils of table 3.1. Right panel: simulation of the deceleration produced by the coils of table 3.1 onto the velocity classes of ^{6}Li atoms.

Coils Number	Position (cm)	N° turns	N° windings	current (A)
1	0	68	28	2
2	7	48	22	2
3	12	48	19	2
4	17	48	17	2
5	22	48	14	2
6	27	48	11	2
7	32	38	7	2
8	36	33	4	2
9	44.5	35	22	-1.6

Table 3.1 – Coils configuration for the Zeeman slower magnetic field. The position expressed in the second column is intended from the beginning of the slower. The "N° turns" column and "N° windings" column show the number of loops in the longitudinal and radial direction, respectively.

has been used in a simulation in *Mathematica* to check if the atoms were actually slowed down when put in such a field. As shown in the right panel of figure 3.9, the velocities of the atoms are really affected by the combination of a counter propagating laser beam and the designed magnetic field and all the atoms having an initial velocity below 830 m/s exit the slower with a much smaller one. With these parameters the final velocity of the atoms is around 30 m/s.
The winding of all the coils for the slower was realized by an external company, which also cared about sticking them together with the help of a thermic glue, which can sustain temperatures up to 170°C.

Magneto-Optical Trap coils

A large magnetic gradient is needed in the center of the science chamber to effectively trap atoms after the Zeeman slower. For this, we use a pair of coils in anti-Helmotz configuration, to generate a quadrupolar magnetic field. The combination of this field with three pairs of counter propagating laser beam, one for each spatial direction, will cool and trap atoms at the same time [100].
These coils can produce a gradient of the order of almost of 1 G/(cm·A). Each coil has an inner diameter of 70 mm and has 6 windings horizontally and 8 vertically, realized with a copper wire with a rectangular section of 1 X 3 mm. They are placed along the z axis of the science chamber, in the channel of the re-entrant viewports. They are shielded with a non magnetic plastic support, which allows water to circulate close to them and have sufficient cooling. Thanks to a relay we can switch the configuration of our coils from anti-Helmotz to Helmotz. In this way, the coils can provide an additional curvature when evaporative cooling is performed.

Feshbach coils

To exploit the rich scenario behind Feshbach resonances, we need some coils to generate offset magnetic fields till values around 1000 G. We designed a pair of large coils for working in an almost ideal Helmotz configuration. The small deviation from genuine Helmotz configuration introduces an helpful magnetic curvature during evaporative cooling.
The coils are realized with a kapton insulated wire with a section of 4.6 mm X 4.6 mm and a hollow core, for water circulation and cooling. Each coil has 8 vertical windings and 7 horizontal ones. Realization of these coils has been done by *Oswald Company*. These are connected to a 200 A power supply (SM 30-200 model from *Delta Elektronika*).
The magnetic field of the Feshbach coils is stabilized in current with the help of a transducer connected to a PID controller. The transducer is placed on one of the wire connect-

ing the power supply to the coils. The feedback loop of the PID controls and corrects the current circulating in the coils. Despite the current stabilization, the value of the magnetic field inside the chamber may change due to fluctuations in the room temperature and in the position of the coils.
To determine the stability of the Feshbach field we apply Radio-Frequency (RF) spectroscopy on a polarized Fermi gas. The RF signal is generated by an RF-antenna with a central frequency around 76 MHz, placed below the science chamber. For increasing duration of the RF-π-pulse, the broadening of the RF-spectrum over the pulse Fourier width signals that noise and fluctuations dominate over the experimental data. We obtain a relative high stability around one part over hundred thousands ($\frac{\Delta B}{B} = 10^{-5}$).

Additional coils: compensation and gradients

We also placed some additional coils around the science chamber for upgrading the features of our system. In particular:

- Compensation coils: these are a set of three pairs of small coils, each one made by a 1 mm X 1 mm copper wire with 6 windings both vertically and horizontally. These are arranged close to a Helmotz configuration, with one pair placed along one of the three spatial directions. These coils are used to shift the center of the MOT, in order to place it on top of the *IPG* beam once the optical dipole trap has to be loaded.

- Longitudinal gradient coils: Along the *IPG* and *Mephisto* direction we placed a pair of two coils in anti-Helmotz configuration, one before and one after the science chamber. These coils are wrapped with a 1 mm X 3 mm copper wire, with 10 (6) vertical (horizontal) windings. The separation among these is around 40 cm, thus the gradient at the center of the chamber is quite small, around 0.1 G/(cm·A). They are used only for the spin separation procedure explained in chapter 6.

3.4 Imaging system

Information about number of atoms, temperature and density distribution of trapped gases are generally obtained by optical diagnostic techniques. In our apparatus we implemented both destructive and non-destructive imaging techniques.
Absorption imaging with resonant light is performed to check the atomic features during the different stages of cooling and evaporation, as well as when during the physics experiment. It is the destructive imaging technique mainly used on a daily basis.
As a non-destructive imaging of the atomic cloud we implemented phase-contrast imaging

with non-resonant light. This technique allows us to repeatedly probe the cloud at different evolution times, with a minimal residual heating, since the imaging pulse is quite detuned respect to the atomic transition. Their features will be compared in the following.

3.4.1 Absorption imaging

This imaging technique is usually performed pulsing a resonant laser beam towards an expanding or even *in-situ* atomic cloud. From the differences of the intensities profiles of the probe beam with and without atoms, the density distribution of the cloud can be reconstructed from the Beer-Lambert law.

Assuming the cloud to be a group of absorptive objects the intensity I of the beam is modified as:

$$\frac{dI}{I} = n(x,y,z)\sigma(z)dz \tag{3.8}$$

where $n(x,y,z)$ is the atomic density, $\sigma(z)$ the scattering optical cross-section and z the direction of propagation of the beam.

The scattering cross section depends on the intensity of the beam and on the detuning δ among the beam frequency and the atomic transition, in accordance to the following formula:

$$\sigma = \sigma_0 \frac{1}{1+\frac{I}{I_{\text{sat}}}+\left(\frac{\delta}{\Gamma/2}\right)^2} \tag{3.9}$$

where $\sigma_0 = \frac{3\lambda^2}{2\pi}$, I_{sat} is the saturation intensity of the transition and Γ its natural width.

With resonant light $\delta = 0$, eq.(3.8) is generally solved in the two limiting cases of low intensities ($I \ll I_{\text{sat}}$) or high intensities ($I \gg I_{\text{sat}}$).

- Low intensity regime: for low saturation, the scattering cross section becomes a constant, and eq.(3.8) can be exactly solved as:

$$I(x,y) = I_0(x,y)e^{-\sigma_0 \int n(x,y,z)dz} \tag{3.10}$$

  The shadow produced by the absorbing atoms is generally casted onto a CCD camera which records the intensity profiles of the incidents beams. Typically, three different images have to be taken by the CCD to reconstruct the column integrated density distribution of the cloud. The first one gives the profile $I(x,y)$ due to absorption of the cloud in TOF measurements or *in-situ*. The second one is taken without atoms and gives the profile of $I_0(x,y)$ and the third one is the background signal I_{bg} taken without light, and which is subtracted at both of the previous images. The column densities $\tilde{n}(x,y)$ is obtained as:

$$\tilde{n}(x,y) = -\frac{1}{\sigma_0}\ln\frac{I(x,y)-I_{\text{bg}}}{I_0(x,y)-I_{\text{bg}}} \tag{3.11}$$

By knowing the CCD pixel size and the magnification of the imaging system, the measured column density is scaled to its real value and physical quantities are obtained.

- High intensity regime: in this regime the cross section is intensity dependent and a more rigorous treatment for solving (3.8) is needed [101]. This technique may be useful while probing high-density samples, as those measured *in-situ* [102]. In the high density regime, multi-scatter events of the probing photons among close atoms may occur. Keeping the intensity well above I_{sat} should saturate the transition, making the scattering cross section not density dependent.

3.4.2 Phase-contrast imaging

Another imaging technique used in our experiment is the so-called phase-contrast technique. This technique reconstructs *in-situ* density distribution in a non-destructive way, allowing to perform multiple images during the same experimental run. This technique may be helpful when probing time-evolution of atomic distribution or phase-separation of the spin components [103]. When a weak probe beam passes through an atomic cloud, it may experience a phase shift ϕ which is proportional to the atomic density and to detuning in the following way

$$\phi \sim \frac{\int n(x,y,z)dz}{\delta} \tag{3.12}$$

The difference of the electric field of the collimated beam and of the one scattered by the atoms will give information about the cloud without significant absorption of photons, since the detuning is generally larger than the linewidth of the transition.
The lowest two hyper-fine states of ^{6}Li have imaging resonances that are generally 76 MHz apart at high field, and so give a different signal when probed with the same beam. Actually if the probe detuning is set in the middle of the two levels, the signal will be proportional to the difference of the clouds with opposite spin. To increase the phase shift signal, the beam is made pass through a particular phase-plate which gives a phase shift of $\pi/2$ to the collimated beam. The phase-plate has a micrometric sized bump in the middle and is generally placed in the focus of the first lens after the science chamber of a certain imaging system. Here the image of the cloud is collimated, while the imaging beam is focused. The phase-plate is aligned to have the imaging beam passing through the bump. The size of the bump is calibrated to give the correct phase shift of $\pi/2$ to the imaging beam. With this the phase signal will be proportional to $|e^{i\pi/2}+i\phi| \sim 1+2\phi$, while without the phase plate the signal would be proportional to $|1+i\phi| \sim 1+\phi^2/2$. Since phase shifts are generally small, a linear dependence of the signal is better than a quadratic one.

3.4.3 Imaging setup

In our science chamber we rely onto two different imaging systems, one for checking day-to-day efficiency of our apparatus and another one for high-resolution imaging of the cloud.

Horizontal imaging setup

This imaging setup shines a resonant laser pulse along the $x - y$ plane of the MOT. The polarization of the beam is linear and perpendicular respect to the quantization axis posed by the Feshbach coils when working at high magnetic fields. In this condition the scattering cross section is reduced by a factor of two. The atomic shadow is then collected by a versatile imaging setup which allows fast switching from two configurations with different magnifications.
A first setup has a magnification $M = 0.5$ which is suited for checking the MOT cloud and the efficiency of the IPG loading. Two lenses in telescope configuration, the first one with focal length of 15 cm, the second with focal length of 7.5 cm, produce the density profiles onto a Stingray CCD camera. The Stingray CCD and the second lens are placed onto magnetic movable mountings, which allow to remove and re-insert them at will, without significantly affecting the imaging quality. After the Stingray, we placed a different lens, always in telescope configuration respect to the first one, with focal length of 40 cm for a magnification around 2.7 of the cloud, imaged onto a *Andor* Ultra camera. The magnified horizontal imaging is used to check the atom number during evaporative cooling stages.

High-resolution imaging system

A more sophisticated imaging system is placed onto the z-axis of the science chamber. This imaging system is based onto a large aspheric lens with a given numerical aperture around 0.61 and a working distance of 24 mm. This lens allows a resolution below 1 μm, which is the relevant length scale (healing length) for the unitary Fermi gas. After this large lens we placed a second aspheric lens with focal length around 15 cm, for a total magnification of the setup estimated to be $M = 7.8 \pm 0.2$.
The resonant imaging beam comes from below the science chamber and has a circular σ^- polarization to correctly drive the transition at high field. Images are then collected by an *Andor* IXon3 EMCCD camera. The high resolution of this setup allows to obtain *in-situ* density distribution and gives access to microscopic details of trapped gases.

Since we have only one science chamber, we must overlap the MOT beams on the z-axis with the imaging beam. We do this by using polarization optics such as a wire grid polarizer and a $\lambda/4$ waveplate. The wire grid polarizer reflects efficiently light with a

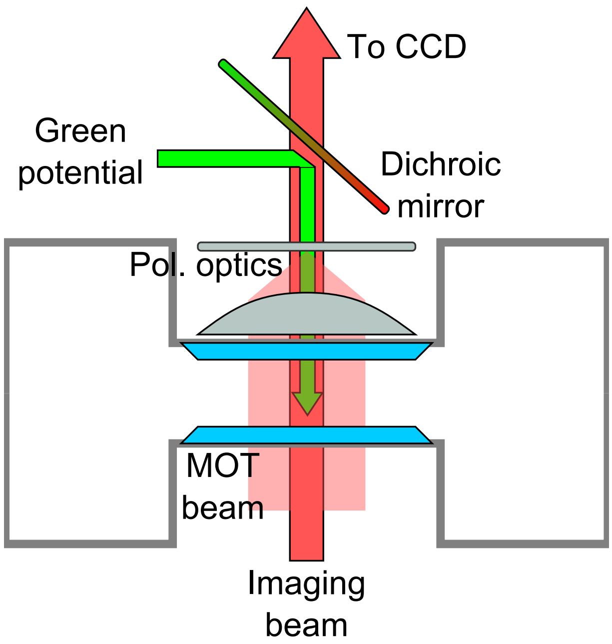

Figure 3.10 – Sketch of the imaging system on the vertical axis of the science chamber. The MOT beam is retro reflected by polarization optics (λ/4 and a wire-grid polarizer) while the imaging beam passes through it. The imaging beam is also transmitted by a dichroic mirror and then collected onto the CCD. The dichroic mirror can reflect instead green light in order to imprint repulsive microscopic potentials onto the atoms.

certain linear polarization and transmits the one with orthogonal polarization. To exploit this feature, the imaging beam and the upcoming vertical MOT beam are overlapped with opposite circular polarizations. Then the $\lambda/4$ waveplate changes their polarization to linear, but still orthogonal one respect to the other. The wire grid polarizer is aligned in order to have the MOT beam reflected and the imaging one passing. After being reflected the MOT beam reaches the atoms with the correct circular polarization. The imaging beam is collected by the CCD.

By preliminary tests of the imaging setup, we found that the resolution of the aspheric lens is not affected by the presence of this polarization optics if this is placed behind the lens. However, to have a collimated retro reflected MOT beam, the wire grid polarizer should be placed in the focus of the aspheric lens. This may represent a problem since we estimated that the intensity of the focused beam should be higher than the damage intensity threshold of the wire grid polarizer. To avoid this we slightly shifted the position of the wire grid polarizer towards the aspheric lens. Despite this, the beam is just a bit focusing while passing through the atoms position and does not significantly affects the efficiency of the MOT. A sketch of the optical configuration is shown in figure 3.10.

The large aspheric lens is also used to imprint microscopic optical potentials onto the cold cloud. With the help of a dichroic mirror, we can make green light at 532 nm passing through the last lens. In particular we aim at studying the transport and dynamics of Fermi gas with a thin barrier optical potential, which is created with the help of a cylindrical lens. Details of this setup will be given in chapter 5. As a future upgrade of the system, we plan to introduce a Digital Mirror Device (DMD) for creating more complex potentials in a holographic fashion [104]. DMDs allow fast and tailored creation of arbitrary potential which could be extremely well-suited in the exploration of transport phenomena in cold gases.

Both the high-resolution imaging and the optical system for tailoring the green light are placed above the science chamber on non-magnetic mountings. First, the aspheric lens and the polarization optics are placed in a PEEK plastic tube, which ensures a very good stability. This is then connected through a translation stage with micrometer accuracy (model LP-2A $XYZ\ \Theta X \Theta Y$ by *Newport*) to a table top breadboard. This is made of fiberglass resin, so completely amagnetic. This ensures a good stability and rigidity of the system during the experimental runs, in particular while fast switches of the magnetic fields are performed. The non-magnetic character of these components will prevent eddy currents to circulate in these, reducing any undesired oscillation of the components as well as the noise over the experimental signal.

CHAPTER 4

Production of degenerate Fermi gases using D_1 gray molasses cooling

In this chapter we summarize the experimental procedure we use to produce large Degenerate Fermi gases (DFGs) of ^{6}Li atoms exploiting, for the first time on this atomic species, D_1 gray molasses cooling. This laser cooling technique allows to achieve sub-Doppler temperatures for atoms, such as lithium or potassium, which lack of a good excited state hyper-fine splitting on the D_2 manifold and consequently of a good sub-Doppler cooling mechanism. D_1 gray molasses cooling allows better initial conditions for evaporation and to achieve quantum degeneracy of large samples in a fast and cheap way, with no need to rely on another coolant atomic species [105] or to use expensive optics and laser sources in the UV region [106].
The main results of this chapter have been published in:

- A. Burchianti, G. Valtolina, J. A. Seman, E. Pace, M. De Pas, M. Inguscio, M. Zaccanti and G. Roati, *Efficient all-optical production of large* ^{6}Li *quantum gases using* D_1 *gray-molasses cooling*, Phys. Rev. A **90**, 043408 (2014).

4.1 D_1 gray molasses

Laser cooling theory predicts the possibility to cool atoms when using pairs of counter propagating beams, red-detuned respect to the atomic transition [107]. Thanks to the Doppler effect, atoms can emit a photon with an energy higher than the absorbed one, lowering their kinetic energy. Theory also predicts a lower bound to the coldest achievable temperature. This temperature, called the Doppler temperature, is achieved at a detuning $\delta = -\Gamma/2$ and is equal to $T_D = \frac{\hbar}{k_B}\Gamma/2$, where Γ is the natural linewidth of the transition. For ^{6}Li the Doppler temperature is around 140 μK.
However, since the very first experiments were performed in the 80's [108], temperatures below the Doppler limit were reached. This was later explained by J. Dalibard and C.

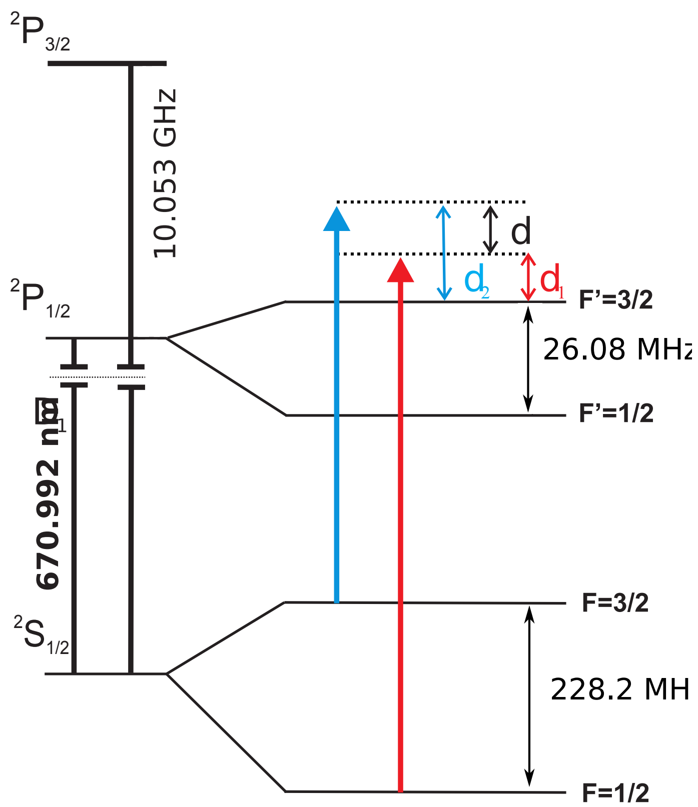

Figure 4.1 – Sketch of the atomic structure on the D_1 manifold. The $^2P_{3/2}$ excited state has been represented as a single line, to stress its small hyper-fine splitting. The splitting on the D_1 manifold is instead larger than the linewidth of the transition. The detunings of repumper and cooling are δ_1 and δ_2 respectively, while $\delta = \delta_1 - \delta_2$ is their relative one.

Cohen-Tannoudji [109] as a consequence of optical pumping among internal hyper-fine levels due to polarization gradient generated by the counter propagating beams, used both in molasses and MOTs scheme. This resulted in a larger cooling force and this effect is generally called Sysyphus cooling. Unfortunately, for ^{6}Li the hyper-fine structure of the excited state in the D_2 manifold is not resolved, causing Sysyphus cooling not to efficiently work.

However, recent experiments at ENS in Paris [110] showed the possibility of exploiting D_1 gray molasses cooling on potassium isotopes which, as lithium ones, lack of an efficient Sysyphus cooling on the D_2 line. This gray molasses reminds of a cooling mechanism in a Λ-type three-levels configuration (fig.4.2), pioneered by A. Aspect and coworkers [111], and successfully demonstrated on the D_1 manifold for heavy alkali atoms already in the 90's [112]. The cooling mechanism can be understood as a cooperative action of Sysyphus cooling and velocity selective coherent population trapping (VSCPT). Since the cooling transition on the D_1 line is a $F \rightarrow F' = F$ transition, Sysyphus cooling is achieved with blue detuning respect to the atomic transition. However, some repumper light is needed to recover atoms in the cycle. When the repumper detuning gets close to the cooling one, the

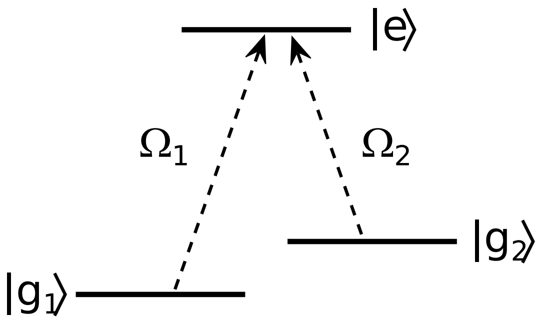

Figure 4.2 – Representation of the three level configuration with the two ground states, $|g_1\rangle$ and $|g_2\rangle$, and their respective coupling transitions, Ω_1 and Ω_2, to the excited state $|e\rangle$.

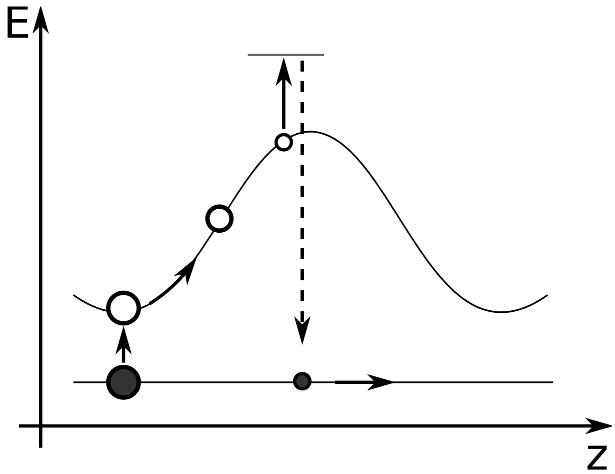

Figure 4.3 – Pictorial view of the Sysyphus mechanism in our configuration. The energy of the bright state (white circles) sinusoidally changes in space because of polarization gradients, while that of the dark state (gray circles) remains constant. At the minima of the bright potential, atoms are transferred from the dark to the bright state and starts climbing its potential, while loosing kinetic energy, naively represented as a shrinking of the circles radius. At the top of the bright potential, atoms are pumped back into the dark state, after a significant loss of kinetic energy. Picture adapted from [113].

atomic structure can be viewed as an effective three levels system. Atoms may so be found into two dressed states, one dark and the other bright, which are a coherent superposition of the two ground-state hyperfine levels, whose wavefunctions can be written as:

$$\begin{aligned} |\psi_{\text{dark}}\rangle &= \frac{1}{\sqrt{\Omega_1^2+\Omega_2^2}}(\Omega_2|g_1\rangle - \Omega_1|g_2\rangle) \\ |\psi_{\text{bright}}\rangle &= \frac{1}{\sqrt{\Omega_1^2+\Omega_2^2}}(\Omega_2|g_1\rangle + \Omega_2|g_2\rangle) \end{aligned} \tag{4.1}$$

where we have used the notation of figure 4.2. The first state of 4.1 is called dark since the action of the optical coupling operator $V = \hbar\Omega_1/2|e\rangle\langle\psi_1| + \hbar\Omega_2/2|e\rangle\langle\psi_2| + h.c.$ is zero. As shown in figure 4.3, the energy of the bright state has a spatial modulation because of polarization gradients, while the energy of the dark one is not affected by light.

For blue detuning, coupling from the dark state to the bright one is most likely to occur at the minima of the bright potential, causing atoms to lose energy by climbing it while moving. At the top of the potential, the coupling towards the dark state is maximum and atoms are pumped back, with a net loss of energy.

This cooling mechanism is expected to be more efficient for a relative detuning among the repumper and the cooling equal to zero (Raman condition). When this condition is fulfilled, only those atoms with zero velocity are pumped into the dark state and stop interacting with the laser light, causing a significant reduction of the cloud temperature.

In the following sections we show our experimental characterization of D_1 gray molasses in free space and its optimization for loading a large number of atoms into an optical dipole trap.

4.1.1 Characterization of D_1 gray molasses

We start by loading atoms from the Zeeman slower into the MOT on the D_2 light. For the MOT beams, we use three mutually orthogonal, retroreflected laser beams with a $1/e^2$ radius of 1.5 cm. At the beginning a large red detuning for both cooling($\delta_C = -9\Gamma$) and repumper ($\delta_C = -6\Gamma$) is set. This increases the capture volume despite raising the MOT temperature. After typically 8 seconds of loading, we have $2 \cdot 10^9$ atoms at a temperature around 2.5 mK.

The D_2 MOT is then cooled by decreasing the intensity of both cooling and repumper to almost 1% of the initial value, while simultaneously reducing their detuning to a value around $\delta_C = \delta_R = -3\Gamma$. After this, we have $N_0 = 1.6 \cdot 10^9$ atoms at T=500 μK. At this stage we apply the D_1 molasses.

The D_1 line is brought to the science chamber by the same optical fibers used for the D_2 MOT. For avoiding damages, we do not inject the amplifiers with the two different lights at the same time. An electronic switch selectively injects the proper beam onto the fiber from the master laser table to the other.

To check D_1 cooling efficiency, we start from a configuration where laser beams have equal intensity in all directions. The D_1 cooling is applied 2 ms after turning off the magnetic fields. We apply the D_1 stage for 2 ms and we set $I_{rep} = 0.2 I_{cool}$, where I_{rep} is the repumper intensity and I_{cool} the cooling one. This imbalance among the two intensities is extremely convenient for us since it provides for free optical pumping into the $F = 1/2$ manifold, which is the most suitable for evaporative cooling. For the data in figure 4.4, we set the cooling detuning to 5.4Γ. The behavior of the temperature and of the fraction of cooled atoms are reported versus the relative detuning δ among the repumper and the cooling. The graph of temperature clearly shows an asymmetric Fano profile, a clear signature of the emergence of a quantum interference effect. As expected, the minimum temperature

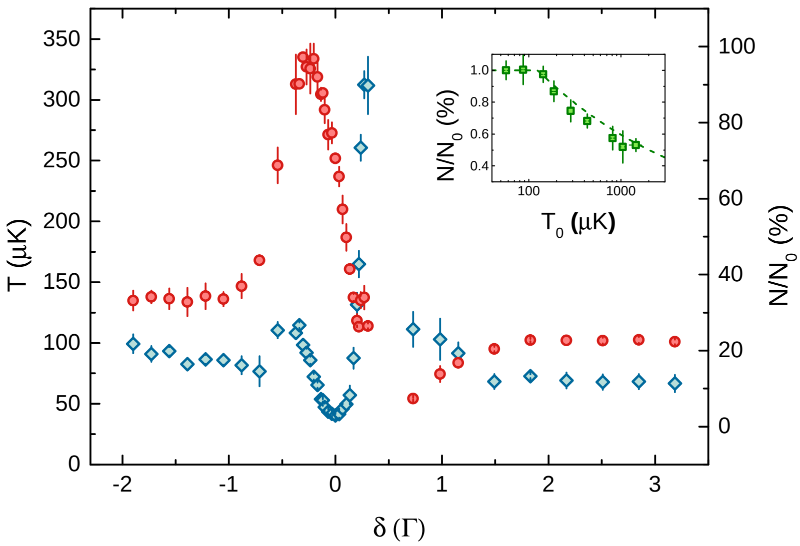

Figure 4.4 – Behavior of the temperature (blue diamonds) and of the cooled fraction (red circles) as a function of the relative detuning δ, here in units of Γ, among the cooling and repumper of the D_1 light. The temperature graph show a clear Fano profile around the Raman condition (gray dotted line). The minimum reported temperature is 40.5(1.0) μK. Error bars are one standard deviation from five independent measurements. Inset: trend of the cooled fraction of atoms after D_1 cooling at the Raman condition for different initial temperatures (x-axis). The capture efficiency is around 100% below an initial temperature of 150 μK. Dashed line is a guide to the eye.

is reached at $\delta = 0$, also referred to as Raman condition. Here, we report a minimum temperature T=40.5(1.0) μK and a cooled fraction $N/N_0 \simeq 75\%$. The Phase-Space-Density (PSD) of the cloud is increased by almost a factor of 20 at the Raman condition, respect to the final stages of the D_2 MOT.

For small values of δ above zero, we observe strong heating and increased atom losses, as discussed in [114]. Away from resonance the temperature instead reaches stationary values due to the Sysyphus effect alone. For values of δ slightly below the Raman condition, we observe a higher capture efficiency which reaches 100% at $\delta = -0.2\Gamma$, despite an higher final temperature. To estimate the capture efficiency at the Raman condition, we evaluated the cooled fraction for different initial values of the MOT temperature. Data are reported in the inset of figure 4.4 and show 100% of capture efficiency for initial temperatures below 150 μK.

The efficiency of D_1 cooling was also investigated, always at the Raman condition, for different values of the absolute cooling detuning. Results are shown in figure 4.5. For high detunings the efficiency of D_1 cooling does not change significantly. Further on, the value of the cooling detuning will be set to 5.4Γ.

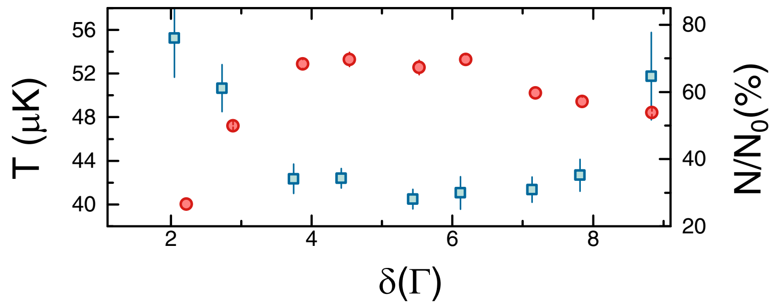

Figure 4.5 – Dependance of D_1 cooling at the Raman condition for different values of the absolute detuning δ_C, in units of Γ, of the cooling light. Minimum temperature is shown in blues squares, while cooled fraction in red circles. We found the best condition to be at $\delta_C = 5.4\Gamma$.

4.1.2 D_1 cooling for optical trap loading

For efficiently loading the *IPG* dipole trap, we apply the D_1 molasses in a different way. We prefer to have larger clouds of atoms in the ODT, with a temperature higher than the minimum one reported in figure 4.4. For this reason we found convenient to turn off both the MOT and compensations coils just 100 μs before applying the first D_1 stage. This lasts for 2 ms with a relative detuning condition $\delta = -0.2\Gamma$. In this configuration, as shown in 4.4, the capture efficiency of the molasses is higher, as well as the temperature.

The loading was further optimized by unbalancing the MOT beams' power. We significantly reduced the MOT beam power along the direction of propagation of the *IPG* and allocate it along the other axes. We so created on oblate cloud to increase the mode-matching among the atoms and the ODT. The *IPG* is raised till a value of 120 W, 3 ms before applying the D1 phase, by a linear ramp of 5 ms.

To increase the capture efficiency, the *IPG* beam waist along the horizontal direction is increased as explained in section 3.2.2 with the RF-modulation on the AOM signal. This results in an increase of the waist in one direction from 45 μm to 85 μm. Thus, we capture up to $N = 2 \cdot 10^7$ atoms at T=135(5) μK.

After this first stage, we apply a second D_1 phase for cooling atoms already captured by the ODT. The strong laser field created by the *IPG* beam induces a Stark shift for both the D_1 cooling and repumper transitions. By spectroscopic investigation of the D_1 lines in intense laser fields, we evaluate for both levels a linear energy shift of +6.3(7)/(MHz·cm^2). For the initial trap power, this results in a 13 MHz shift. This allows to perform the second D_1 stage without changing the absolute value of the cooling detuning. In fig.4.6, the efficiency of the second D_1 stage is investigated as a function of the relative detuning δ. A Fano profile, even if less pronounced, can yet be distinguished in the temperature trend, which is found to have a minimum of 80 μK at the Raman condition. Consistently with the previous investigation over the D_1 capture efficiency (see inset in fig. 4.4), the fraction of cooled atoms is around 100%.

Optical pumping in the $F = 1/2$ manifold is provided by switching off the repumper 20 μs before the cooling. This results in a moderate increase of the temperature of 10% and no detectable atoms in the $F = 3/2$ level.
Mastering of the D_1 gray molasses allows us to start the evaporation procedure with initial conditions significantly improved respect to the conventional case. This is an important step towards the production of large and deeply degenerate fermionic samples.
Moreover, D_1 cooling is extremely similar to recently demonstrated EIT cooling [115] for single-atom detection in optical lattices. This technique, similarly to Raman-sideband cooling [116, 117], allows to image single atoms in optical lattices while cooling them down. The achievement of single particle observation and manipulation will enable a new generation of experiments for the quantum simulation of exotic phases connected to condensed matter systems. The demonstration of D_1 cooling in ODTs is a first step in this direction for our apparatus.

4.2 Evaporative cooling till quantum degeneracy

The laser cooling stage pumps all atoms in the $F = 1/2$ manifold. The application of a Feshbach magnetic fields automatically splits the atomic population in the lowest and second to lowest hyperfine levels (called state $|1\rangle$ and $|2\rangle$, respectively). This is necessary since evaporative cooling of cold atomic fermions is efficient only if these are found in two different hyperfine levels, acting as a pseudospin degree of freedom.
To further enhance evaporation, we generally exploit the presence of a broad Feshbach

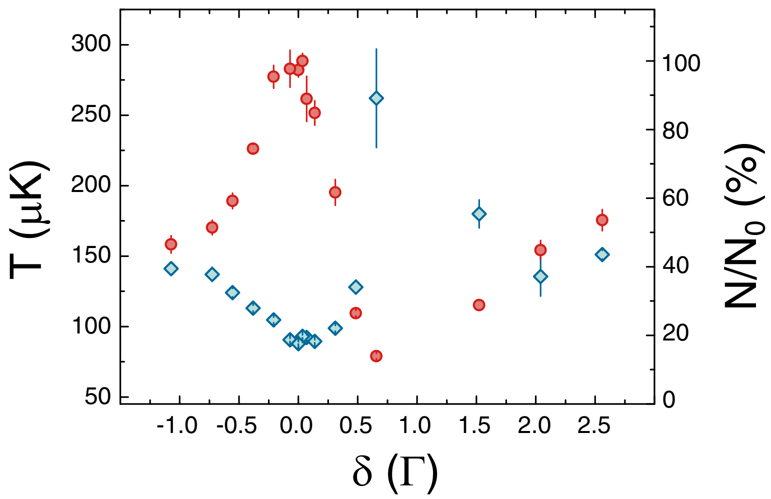

Figure 4.6 – Efficiency of D_1 cooling in a strong laser field. For this data set the ODT beam has 120 W of power and an ellpictic waist of 45 μm along gravity and 85 μm along the other direction. A Fano profile in the temperature trend is still observable (blue diamonds). Because of the lower initial temperature, the capture efficiency is maximum also at the Raman condition.

resonance among $|1\rangle$ and $|2\rangle$ at 832 G [25], which allows a fine tuning of the two-body scattering length. On top of the Feshbach resonance, the scattering cross-section reaches the maximum value allowed by quantum mechanics, making evaporation and thermalization extremely efficient. Moreover, differently from bosonic atoms, the *Pauli* exclusion principle forestalls three-body losses on resonance, avoiding the formation of Efimov trimers and increasing the lifetime of the sample [118].
We typically perform a first evaporation stage at 832 G, bringing the *IPG* from 120 W to 30 W by a 500 ms linear ramp. During this stage, we continuously apply RF sweeps at the $|1\rangle$-$|2\rangle$ transition, to balance the population in the two hyperfine levels in an incoherent way.
After this, the PID control sets in, controlling the output power of the *IPG* AOM through an exponential ramp, with adjustable duration and time constant, according to the kind of Fermi gas wanted. For ^{6}Li, the usual outputs of the evaporative cooling stage are two: when evaporation is performed on top of the Feshbach resonance a strongly-interacting fermionic superfluid is produced, while evaporation away from the resonance produces a normal, weakly-interacting Fermi gas.

Production of BEC-BCS crossover Fermi superfluids

At an offset Feshbach field among 760 G and 832 G, when the temperature is decreased, the atom-molecule chemical equilibrium favors the formation of molecules [119]. Close to resonance, these are dimers in a sort of halo state [3], with remarkable stability against inelastic three-body collisions.
Moving away from resonance on the BEC side, the reduction of the scattering length results in an increase of the binding energy and consequently of the bosonic character of the dimers. If the temperature is low enough, these composite molecules undergo Bose-Einstein condensation. A nice example of the formation of a molecular BEC, while crossing the critical temperature, is shown in figure 4.7. At best, we end up with $5 \cdot 10^5$ molecules, with a condensed fraction above 90%. The dimer-dimer scattering length is a finite fraction of the two-body one ($a_{\mathrm{dd}} = 0.6a$, see [26]), and so not vanishing.
According to Bogoliubov theory, the resulting interacting BEC is also a superfluid. If for positive scattering lengths ($a > 0$) superfluidity is provided by Bose-Einstein condensation of deeply bound molecules, on the other side of the resonance, hence for negative scattering lengths ($a < 0$), a many-body effect is responsible for superfluidity. This is generally driven by the Cooper instability in the framework of conventional BCS theory. The Feshbach resonance interconnects among these two limiting cases, with the creation of a stongly interacting state, the so-called the unitary Fermi gas, that is a pristine example of a genuine many-body state [120].

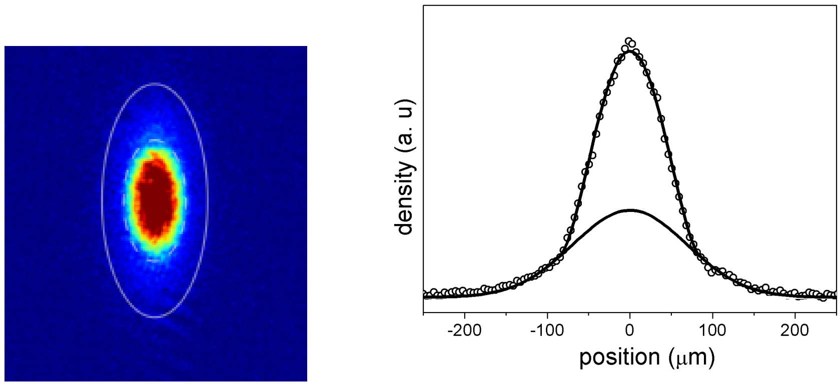

Figure 4.7 – Evidence of bimodal distribution towards the end of evaporation, showing evidence of Bose-Einstein condensation.

Despite the more difficult analysis for these systems, a first demonstration of the superfluid transition has been achieved by the observation of arrays of quantized vortices [121] after stirring a movable object (a repulsive laser beam).

Another elegant demonstration of the occurring superfluid phase transition has been provided by M. Ku and coworkers in ref. [122], where, by high-precision measurements of local thermodynamical variables in the Local Density Approximation (LDA), the characteristic lambda-like feature of both the compressibility and the specific heat were observed at the superfluid transition.

Following other seminal works on the determination of the Equation of State (Eos) across the BEC-BCS crossover [123, 124], the method of ref.[122] provides access to the uni-

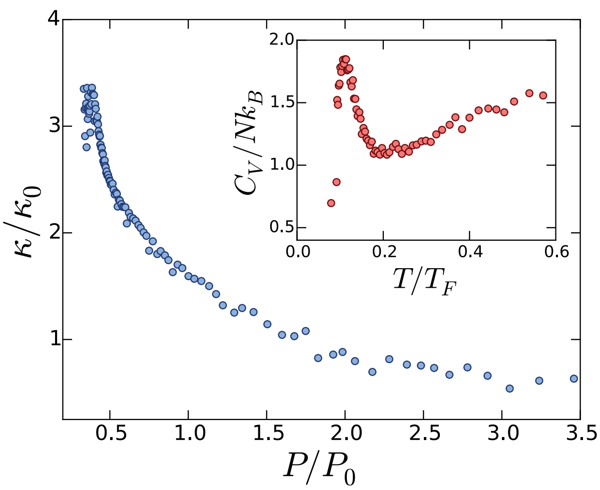

Figure 4.8 – The superfluid transition in the Unitary Fermi gas, through the lambda-like feature of the compressibility (blue) as a function of temperature. Inset: evolution of the specific heat (red) as a function of temperature at the crossing of the critical temperature.

versal thermodynamics of the Unitary Fermi gas, without the need of any external thermometer. With the high-resolution imaging system of our apparatus, we successfully implemented the method of ref.[122] for absolute thermometry of the Unitary Fermi gas. The resulting lambda-like feature of the compressibility is reported in fig.4.8.
With this method we could probe superfluidity of our gas at the end of evaporation and measure a temperature T at the trap center as low as $0.07(2)T_F$, where T_F is the Fermi temperature of our gas.
Another way for determining the temperature in our cloud is to perform a magnetic field sweep on the BEC side of the resonance. The gas is then mapped onto a molecular BEC and by TOF expansion it is possible to measure by absorption imaging the condensed fraction and from this the temperature of the cloud. At the end of our evaporation we can achieve at best a condensed fraction above 90%. On a daily basis, this method provides the easiest procedure for checking the efficiency of our apparatus, since the method of ref.[122], despite being more accurate and reliable, relies on the averaging over more than one hundred of experimental images for reducing the noise during the image processing.
Our experimental cycle for producing deeply degenerate fermionic superfluids last around 15 s. This is mainly limited by the 8 s loading of the MOT and by the small curvature given by the Feshbach field, which is of around 8 Hz for a Feshbach field of 832 G. Despite some disadvantages during evaporation, such a small magnetic curvature is ideal for exploring the physics behind two-dimensional Fermi gases, providing for free an almost flat potential along the axis of the two dimensional plane.

Production of a normal Fermi gas

After the first ramp of *IPG*, the still high thermal energy of the cloud allows to safely reduce the Feshbach magnetic field away from resonance, without creating molecules or observing any loss. The scattering length among state $|1\rangle$ and $|2\rangle$ (i.e. a_{12}) has a minimum at around 300 G ($a_{12} \sim -300a_0$), extremely convenient for evaporation. However, this minimum is more pronounced for the mixture of $|1\rangle$ and the third to lowest hyperfine level, hereafter called $|3\rangle$ (see fig.4.9 and appendixA). The a_{13} scattering length at 300 G has a minimum value of almost $-900a_0$. This results in almost a factor of 10 improvement in the scattering cross-section of the $|1\rangle$-$|3\rangle$ mixture respect to the $|1\rangle$-$|2\rangle$ one.
For exploting this, when reducing the Feshbach coils, we first target the magnetic field at 584 G. Since here $a_{13} \sim a_{12}$, the application of a 100 μs long RF π-pulse on the $|2\rangle$-to-$|3\rangle$ transition, brings all of the atoms in $|2\rangle$ to $|3\rangle$, with not detrimental final state effects or collisional broadening during the transfer. After this, we again reduce the Feshbach field till 300 G. To provide enough confinement, we selectively turn on an additional curvature

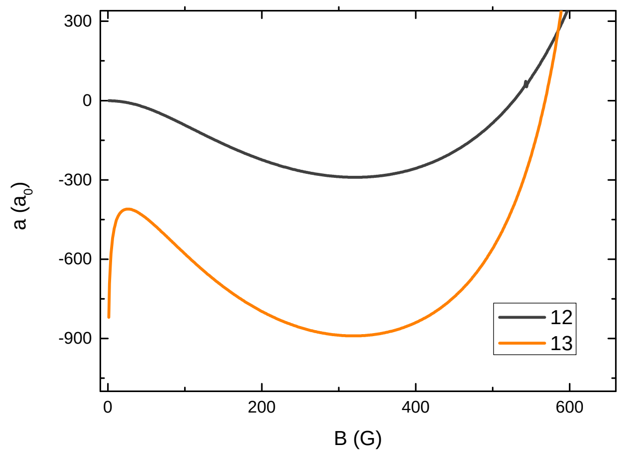

Figure 4.9 – Comparison among the scattering lengths away from the Feshbach resonance for the $|1\rangle - |2\rangle$ (gray line) mixture and the $|1\rangle - |3\rangle$ (orange) one. The $|1\rangle - |3\rangle$ has an advantageous minimum at 300 G. At around 584 G the two scattering lengths are almost equal.

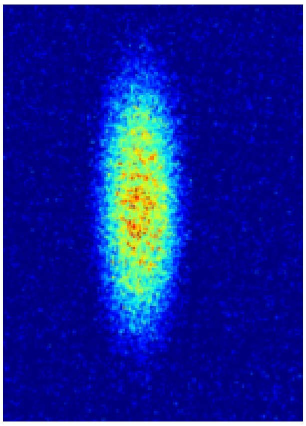

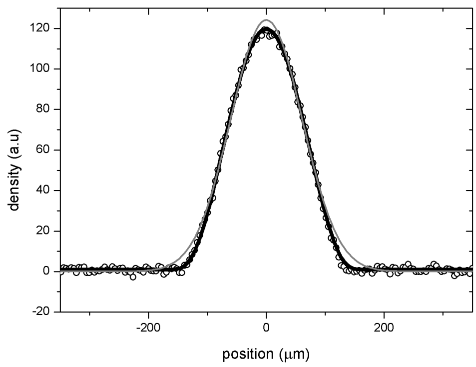

Figure 4.10 – On the left we show an expanding normal Fermi gas. On the right we show its integrated column density, fitted with both a gaussian profile (gray line) and a Fermi-Dirac distribution. The gaussian fit clearly both at the wings and on top of the cloud. The measured temperature in this case is $T/T_F = 0.06$ with $N = 3 \cdot 10^5$ per spin component.

magnetic field using the MOT coils in Helmotz configuration or load a second ODT from a *Mephisto* laser.

We finish evaporation with a typical atom number around $N = 3 \cdot 10^5$ per spin component and a temperature below 0.1 T_F, as reported in fig. 4.10. Remarkably, the evaporation ramps (figure 4.11) of the $|1\rangle - |3\rangle$ mixture at 300 G looks very similar to the one of the Crossover Fermi gas, showing extremely good thermalization properties for a fast production of a deeply degenerate sample. Evaporation of the $|1\rangle - |2\rangle$ with the same ramps was instead found to be unsuccessful, resulting in a sample way hotter and with

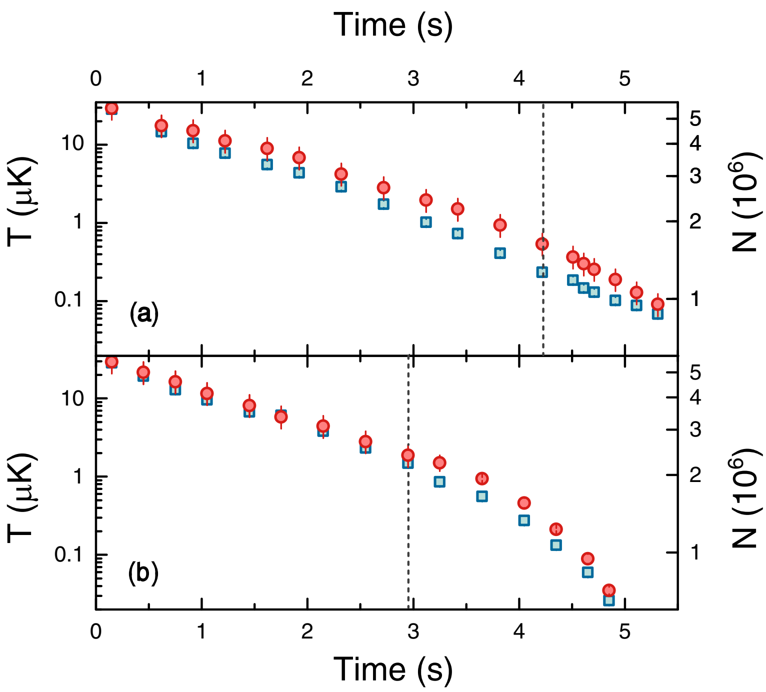

Figure 4.11 – Comparison among the evaporation ramps on the Crossover (top panel) and a t 310 G in the $|1\rangle - |3\rangle$ mixture (lower panel). In function of time of forced evaporation we report both the atom number (blue squares) and temperature (red circles). Vertical dotted lines show the onset of degeneracy for temperatures below the condensation one on the crossover and below the Fermi temperature at 310 G. The behavior of the two ramps is very similar, showing extremely good evaporation properties of the $|1\rangle - |3\rangle$ mixture.

significantly reduced atom number because of a worse thermalization due to a smaller scattering cross section.

The overall experimental procedure for producing the normal Fermi gas is of the order of 22 s.

Differently from the BEC-BCS superfluid case, while evaporating at 300 G the magnetic curvature due to the Feshbach coils is just of 3 Hz. This would not be enough for efficient evaporation or for preventing undesired spilling of atoms. The addition of a magnetic or optical curvature is thus mandatory.

CHAPTER 5

Coherent dynamics of strongly interacting fermionic superfluids

This chapter covers the first experimental investigation of coherent Josephson dynamics in atomic superfluids across the BEC-BCS crossover. A detailed description of the experimental configuration exploited for this purpose will be given in the following sections, together with the analysis of the rich phenomenology we have observed.
The main results have been published in:

- G. Valtolina, A. Burchianti, A. Amico, E. Neri, K. Xhani, J. A. Seman, A. Trombettoni, A. Smerzi, M. Zaccanti, M. Inguscio, G. Roati, *Josephson effect in fermionic superfluids across the BEC-BCS crossover*, Science **350**, 1505 (2015).

5.1 Experimental realization of an atomic Josephson Junction

For the investigation of the Josephson dynamics, our starting point is a tunable, crossed dipole trap where the atomic superfluid is produced. This is obtained by crossing the *IPG* and the *Mephisto* beams. The advantages of this configuration are essentially two. First, due to the tighter confinement of the *Mephisto* beam, atoms are essentially held along its axis, in a quite elongated cigar shaped trap. The trap aspect ratio is typically around 1 : 10. This allows an experimental investigation of a one-dimensional dynamics, triggered, as explained below, just along the longitudinal trap axis. Second and most important, the crossing with the *IPG* beam sets the minimum of the overall trapping potential. By tuning the RF-signal of the *IPG*'s AOM, the crossing point can be physically moved inside the science chamber, without affecting the evaporation efficiency. The high electronic control over the RF-signal allows an accurate positioning of the trap center, a fundamental prerequisite for the experiments hereafter described.
The atomic superfluid is generally produced in the $|1\rangle$ and $|2\rangle$ hyperfine levels, by forced evaporation on the top of their scattering resonance at 832 G. Typically, we end up with

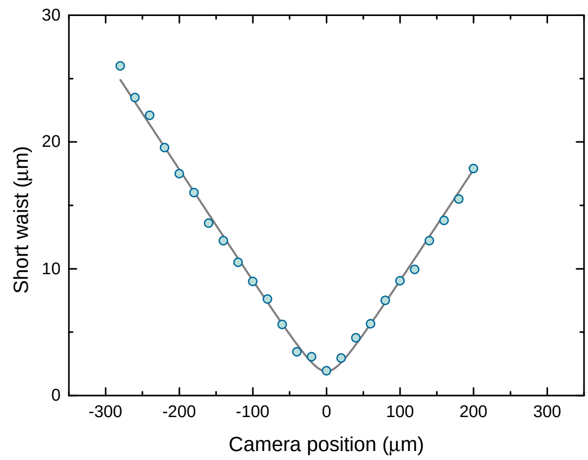

Figure 5.1 – Experimental measurement of the barrier short waist w_x along the beam direction. In the focus the experimental measurement gives 1.95(3) μm, while the fit by the theoretical expected trend $w_x = w_0\sqrt{1+\left(\frac{z}{z_R}\right)^2}$, where z_R is the green beam Rayleigh range, gives a value of 1.90(1)μm.

10^5 atoms per spin component, or equivalently 10^5 fermionic pairs. The trap frequencies are around 15 Hz along the longitudinal axis, 170 Hz along gravity and 150 Hz in the other radial direction.

The final temperature is extracted by measuring the EOS of the Unitary Fermi gas [125]. This gives us a final temperature $T = 0.07(2)T_F$, sufficiently below the superfluid critical one. According to [62], this condition ensures a superfluid fraction saturated at one for the resonant superfluid and the nearby strongly interacting regimes, both for positive and negative scattering lengths. Consistently with this, we also measure in time-of-flight the Bose condensed fraction by sweeping the Feshbach field in the BEC limit. This is found to be above 90%. At first order, a superfluid fraction close to one, across the whole BEC-BCS crossover, allows to neglect detrimental dynamical effects arising from normal currents, focusing only on a pure superfluid dynamics.

After having finished the evaporation stage on top of the Feshbach resonance, all the other interaction regimes are reached after evaporation by changing the Feshbach field through a linear ramp of tunable duration among 200 and 300 ms.

Characterization of the barrier potential

The atomic Josephson Junction (JJ) is realized by imprinting onto the atomic cloud a strongly elliptic repulsive optical potential. The beam light is brought from a *Verdi-V8* laser to the science chamber by a photonic crystal fiber from *NKT-Photonics*. At the fiber output we placed a collimation stage to a have a two-inches diameter beam. This beam has a wavelength of 532 nm, blue-detuned respect to the main transition of , resulting in a repulsive potential.

In order to engineer the profile of a thin insulator among two superfluids, the beam is made pass through a cylindrical lens with focal length $f = 25$ cm. At the focus of the aspheric lens, this results in a dimension much more squeezed than the other. The beam is first characterized on a replica optical system, which reproduces the exact beam path towards the science chamber. The only difference is given by the glass window after the aspheric lens. Lacking of another 6 mm thick viewport as in the science chamber, we substitute it with a 4 mm CF100 silica window. For the short axis, we measure on a CCD camera a beam waist of 1.90(1) μm, as shown in fig.5.1, while for the long one a waist of 840(30) μm. For the short axis measurement we added a X 20 magnification stage after the barrier focus, in order to resolve the micrometer sized waist. The long barrier waist is essentially constant over the displacement of fig.5.1.

To tune the angle of the barrier respect to the cloud, the cylindrical lens is placed on a rotating mounting, as those for conventional wave plates.

When placed onto the real science chamber, the 6 mm viewport may introduce additional aberrations, in particular along the short waist axis. Moreover, having just one large aspheric lens, we cannot correct for chromatic errors, such as the shift of the focus distance for different wavelengths. On the replica system, we measured the shift among the red imaging light and the green one to be of 1.4 μm. Given the short Rayleigh range of the green beam, this would result in a considerable enlargement of the barrier at the actual cloud position.

In the experiment, the aspheric lens is held on a vertically movable mounting with micrometer accuracy, and placed to have the image of the cloud probed by the red light on focus. Along the barrier path, we placed a two-lenses telescope with a $\times 1.25$ magnification. The last of these two lenses is mounted on a translational stage with a micrometer scale. This allows to move the focus of the barrier beam independently respect to the red light and to compensate for the achromatic shift. On the replica system, the movement of the telescope did not affect the value of the short beam waist in the focus.

To correctly focus the barrier, we perform a tunneling experiment on a molecular BEC. As it will be explained in the following sections (see fig.5.4), we produce the BEC with the trap minimum displaced respect to barrier position, in order to have a population difference among the two sites of the barrier. For this first investigation, we start with a population imbalance $z = \frac{N_L - N_R}{N_L + N_R} \simeq 0.40$, with N_L (N_R) being the number of molecules on the left (right) reservoir. The barrier is ramped up during evaporation till a tunable value V_0, without affecting the final temperature of the cloud. At this point, we non-adiabatically bring back the trap, centering it onto the barrier position. After half of the longitudinal trapping period, we measure how the population imbalance has evolved as a function of

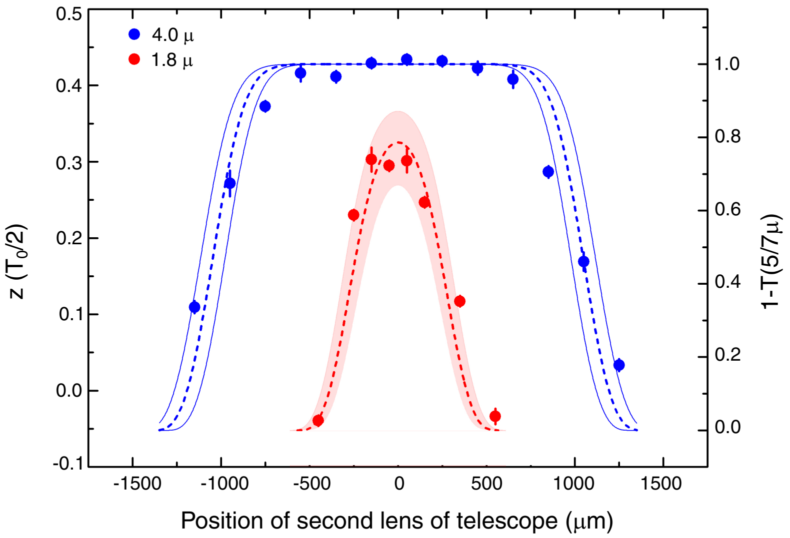

Figure 5.2 – Calibration of the barrier focus by moving the translational stage of the second telescope. The experimental data (red circles for $V_0 = 1.8\mu$ and blue circles for $V_0 = 4.0\mu$) are compared with the theoretically expected transmission probability given by the formula of eq.(5.4).

the movable lens position in the $\times 1.25$ telescope. Data are shown in fig.5.2. When the barrier is in focus, the tunneling through the other reservoir is more suppressed and the population imbalance remains quite high. For the data of fig.5.2, the barrier focus is at the zero point along the x-axis, where a maximum of the imbalance is observed.
Once having aligned the barrier with the previous method, we measure the barrier waist by imaging the density profile onto a molecular BEC. In the BEC limit, the Thomas-Fermi approximation tells us that the density distribution of the BEC can be written as:

$$|\psi(r)|^2 = \mu - V(r) \tag{5.1}$$

where μ is the BEC chemical potential and $V(r)$ the trapping one.
As for the negative of a photo, the atomic density profile mirrors the one of the confining potential, and also of the eventual barrier. We so place the center of the cloud onto the barrier. We raise the barrier in the cloud center till a value of 0.3μ, well below the experiments reported in fig.5.2. In this way, we don't pierce the cloud till the bottom of the density distribution. The dip created by the barrier is fitted with a gaussian profile. In the measurement, we take into account also the effect of the imaging pulse, which heats the sample while probing it. On such a short micrometer scale, this results in a sizable diffusion of the atoms during the imaging time, broadening the barrier dip carved into the density profile. The trend of the measured barrier waist is shown in fig.5.3 for increasing duration times of the imaging pulse. As it can be seen, the longer the pulse duration

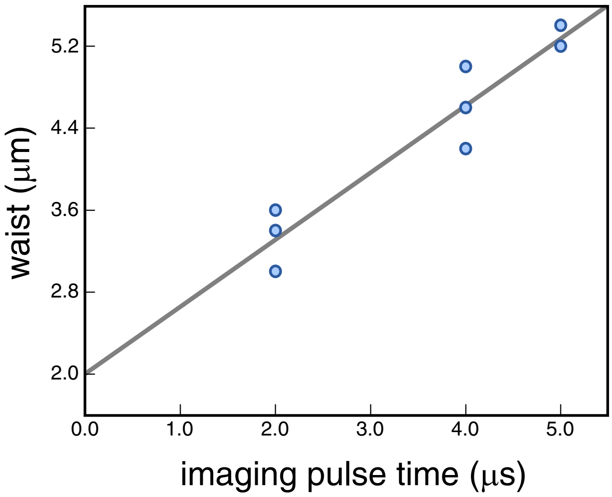

Figure 5.3 – Evolution of the measured barrier waist on the BEC profile for increasing duration of the imaging pulse. We extrapolate a barrier waist of 2.0(2) μm for a zero duration pulse, that is the real size of the barrier.

the wider the fitted dip. We ascribe this to the previously discussed increase of heating and diffusivity. From these, we extrapolate with a linear fit the beam waist for an ideal pulse of zero duration time. We obtain a value of 2.0(2) μm, in good agreement with the independent measurement.

To further validate our results, we develop a simple theoretical model for determining the transmission probability of the Bose gas through the barrier. First, in accordance to [98], we express the effective potential of the barrier as:

$$V(r) = C \cdot I(r) \tag{5.2}$$

where C takes into account all of the lithium atomic constants [126] for transforming the light intensity $I(r)$ in the potential energy felt by the composite molecules.

The peak potential height V_0 is given by the ratio:

$$V_0 = C \cdot \frac{P_0}{w_x(p) w_y} \tag{5.3}$$

where P_0 is the beam power and $w_x(p)$ (w_y) the short (long) beam waist.

The short waist $w_x(p)$ is a function of the movable lens position p according to the formula $w_x(p) = w_x^0 \sqrt{1 + \frac{(p/13)^2}{z_R}}$, where w_x^0 is the minimum of the short waist and z_R its Rayleigh range. The factor 1/13 takes into account that a displacement Δp of the movable lens becomes $\Delta p/13$ in the aspheric lens focus. This was independently measured on the replica optical system.

To develop our one-dimensional theoretical model, we neglect the role of interactions (single-particle approximation) and assume atoms to have the mean-energy per particle ϵ of a BEC, which is 5/7 of the BEC chemical potential. We further approximate the barrier to a square-well of height V_0 as expressed in eq.(5.3), and width $b = w_x(p)\sqrt{2 \ln V_0/\epsilon}$. The final expression for the transmission probability reads as:

$$\mathcal{T}(V_0, p, \epsilon) = 1/\left(1 + \frac{w_y}{2\sqrt{2}}\left(\sqrt{\frac{\epsilon}{V_0}} + \sqrt{\frac{V_0 - \epsilon}{\epsilon}}\right)^2 \sinh^2\left(\sqrt{\frac{2m}{\hbar^2}(V_0 - \epsilon)}\right)\sqrt{\ln\frac{V_O}{\epsilon}}\right) \tag{5.4}$$

Expectations for this model are shown in fig.5.2 assuming a short waist of 2.0 μm, as the one measured by the *in-situ* density profile dip. We found good agreement with the experimentally measured tunneling probability. We so take the value of 2.0(2) μm as the width of our barrier.

This calibration is of paramount importance for understanding how to correctly tune the barrier height respect to the energy scale of the system and address different regimes. For $V_0 \ll \mu$, we are in the so-called hydrodynamic limit, while when $V_0 \geq \mu$ we can access the Josephson dynamics, since the barrier is not anymore a trivial perturbation for the atomic density profile.

5.2 Superfluid versus single-particle tunneling

In the first set of experiments, we compare the dynamics through the barrier of a molecular BEC versus that of a normal non-interacting Fermi gas. The molecular BEC is realized by evaporating on top of the Feshbach resonance and then moving to a field of 690 G. This gives an interaction parameter $1/k_F a \simeq 4$. The non-interacting Fermi gas is instead produced in the $|1\rangle$-$|3\rangle$ mixture as explained in section 4.2, till a final temperature $T \leq 0.10(2)T_F$. The scattering length is then reduced to zero by sweeping the Feshbach field till the zero-crossing of the $|1\rangle$-$|3\rangle$ scattering resonance at around 568 G [25].

In both regimes, we excite the sloshing or also-called dipole mode with the barrier on. For small excitations, or equivalently in the linear response regime, the frequency of this mode is coincident with that of the Josephson plasma oscillations ω_J, and so, through the relation $\omega_J = \sqrt{E_J E_C}$, an effective probe of the Josephson energy. To properly define a Josephson plasma mode, according to [70], the value of ω_J for trapped atomic gases should be a fraction of the trapping period, even if not extremely smaller than that.

To excite this mode, the usual procedure we follow is summarized in fig.5.4, already described in the previous section for the characterization of the barrier focus. During evaporation, we keep the barrier at the target value V_0, with the trap center slightly displaced from the barrier position. We checked the presence of the barrier not to affect the evaporation efficiency. For triggering the dynamics, we center the trap in a non-adiabatic fashion back onto the barrier position.

One can think the situation in the JJ to be at time $t = 0$ as depicted in fig.5.5. This results in an initial non-zero population imbalance z, defined in the usual formula $z = \frac{N_L - N_R}{N_L + N_R}$. Equivalently to an initial chemical potential difference, this imbalance may trigger the dy-

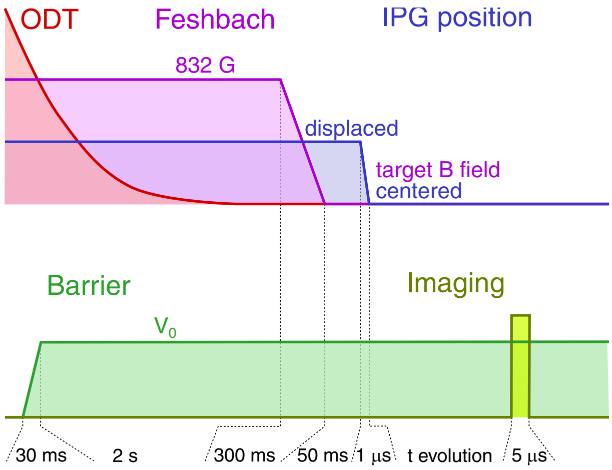

Figure 5.4 – Experimental procedure for triggering the dynamics in the atomic JJ. The barrier (green) is turned on before finishing evaporation in the ODT (red). After finishing the evaporation ramp, the Feshbach field is adjusted at the target $1/k_F a$ and after 30 ms, the *IPG* center (blue) is non-adiabatically placed on top of the barrier beam. After an evolution time t we measure the imbalance through resonant absorption imaging (acid green).

namics through the barrier. This quantity is evaluated by counting the atom number in each site of the well by absorption imaging.

In this first comparison among superfluid and normal tunneling, we start with a small population imbalance $z \leq 0.05(1)$. Such a small population difference is of primary importance for not exciting the radial modes of the trap, which may introduce breathing in the sloshing mode. Moreover, we avoid the entrance into the Macroscopic Quantum Self-Trapping (MQST) dynamics, since, as explained in section 2.4.1, this is triggered by self-interactions in each well.

The time evolution of the population imbalance is reported in panel 5.6. As it can be seen, the BEC, even for barriers higher than its energy per particle ϵ shows clear oscillations, with negligible damping, while those of the ideal Fermi gas are strongly damped even for V_0 below the threshold set by ϵ. This is a first signature of the differences among superfluid versus normal tunneling, which we mainly correlate to phase-coherence. In the normal case, any atom almost freely tunnels through the barrier, without significantly being affected by the presence of other particles. As a result of the single-particle character of this process, the overall dynamics is incoherent. For increasing barrier heights, this results in an increase of the damping and a washing out of the initial population difference. For the superfluid BEC instead, the presence of a macroscopic wavefunction with a well-defined phase-relation guarantees a synchronous tunneling among all particles with no damping, even for a range of barrier heights above the energy per particle.

Another difference arises from the evolution of the frequency ω_J of this oscillations, whether damped or not. The trend of the ratio ω_J/ω_0 as a function of V_0/ϵ is reported in

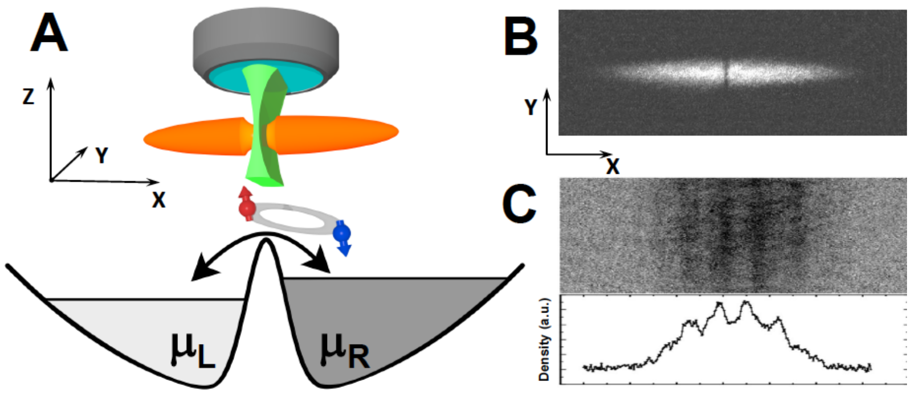

Figure 5.5 – a) Sketch of the atomic (JJ) with an initial non-zero population imbalance. b) Typical image for determinin the population imbalance, by counting the number of atoms N_L on the left side of the barrier and N_R on the irght side. c) Interference pattern of a molecular BEC after release from the trap. The interferogram allows determination of the relative phase among the two quantum states.

fig.5.7. Here, ω_0 is the axial trap frequency, which sets our natural time reference. For the superfluid case, once the barrier is higher than ϵ, the dynamics occurs at a frequency lower than the trapping one ω_0. This can also be seen in the panel of fig.5.6, where for higher barriers a significant slowing in the superfluid dynamics is signaled by a drift respect to the trapping period, marked as dashed lines. For the ideal Fermi gas the, dynamics happens only at the bare trap frequency and for barrier peaks below the mean-energy per particle. For even higher barriers ($V_0 > 2\epsilon$), the dynamics gets to noisy and we cannot detect a clear oscillation anymore.

This is a remarkable difference among the superfluid and the single-particle dynamics. In a certain sense, this is analogous to the drop of resistance for an atomic Fermi superfluid, which has been recently measured in [127]. Once $V_0 \geq \epsilon$, the barrier cannot be considered anymore a small defect and only a superfluid, thanks to its phase-coherence and frictionless flow, can pass through it. Moreover, this critical condition $V_0 \geq \epsilon$ is coincident with the assumption of the two-mode approximation for detecting Josephson plasma oscillations in atomic superfluids [67]. We can so conclude that for $V_0 \geq \epsilon$ we enter the Josephson regime, as signaled by the lowering of the Josephson plasma frequency respect to the bare trap one [70], which itself becomes our primary tool of investigation.

Moreover, one expects the imbalance dynamics to be coupled to the one of the relative phase ϕ. The relative phase ϕ is the difference among the condensates phases, that is $\phi = \phi_L - \phi_R$, where again the label L (R) refers to the left (right) reservoir. In the Josephson regime, the imbalance z and the phase ϕ are dynamically conjugated variables, so a relative phase shift of $\pi/2$ is expected among the two dynamics. We measure the phase ϕ by time-of-flight (TOF) measurements, letting the clouds expand for up to 15 ms, after having turned off at the same time both the trap and the barrier. We then probe the ex-

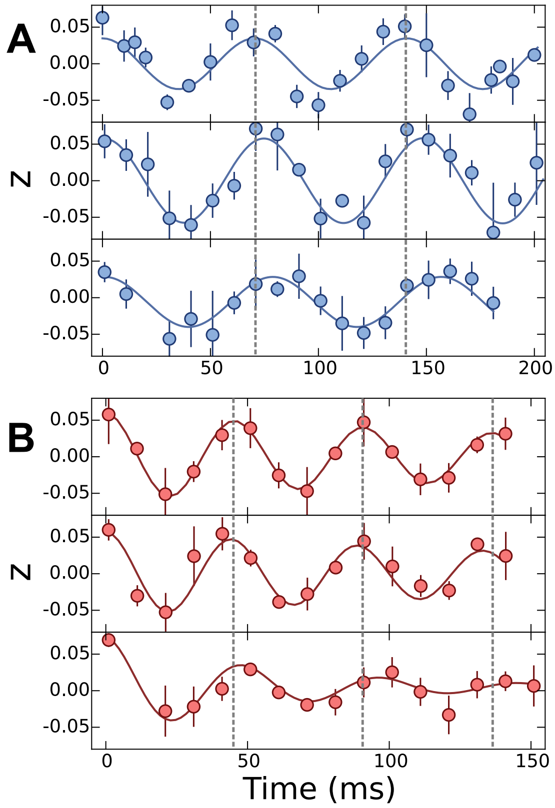

Figure 5.6 – Superfluid vs single-particle tunneling. a) Time-evolution of the population imbalance (blue symbols) of a molecular BEC for increasing barrier height V_0 respect to the energy per particle $\epsilon = \frac{5}{7}\mu_{\mathrm{BEC}}$. From top to bottom V_0/ϵ =0.25(2) (top), 1.50(3) (center),1.75(4) (bottom). b) Time-evolution of the population imbalance (red symbols) of non-interacting Fermi gas for increasing barrier height V_0 respect to the energy per particle $\epsilon = \frac{3}{4}E_F$. From top to bottom V_0/ϵ =0.40(2) (top), 0.60(2) (center), 0.81(3) (bottom). The dashed gray lines signal the expected maxima for a dynamics at the trap frequency ω_0.

panded clouds by resonant absorption imaging. A typical experimental picture is shown in fig.5.5c, where the nice interference patterns among the two superfluids can be distinguished in the modulation of the density profile. The phase ϕ is determined by fitting the density distribution with a gaussian profile plus an overall sinusoidal modulation as:

$$n(x,y) = Ae^{(-x^2/\sigma_x^2)}e^{-y^2/\sigma_y^2}(1+Bcos(kx+\phi) \tag{5.5}$$

An example of the coupled imbalance-phase dynamics is shown in fig.5.8. As expected, within our experimental resolution, the imbalance and the phase oscillate at the very same Josephson plasma frequency ω_J and with a relative phase shift $\delta\phi = 1.1(0.1)\ \pi/2$, consistent with the expectation for a $\pi/2$ difference.
Instead, for the ideal Fermi gas, the TOF expansion does not unveil an interference pattern, due to lack of a proper defined phase.
Again, the measurements of conjugated imbalance and phase oscillations are a smoking

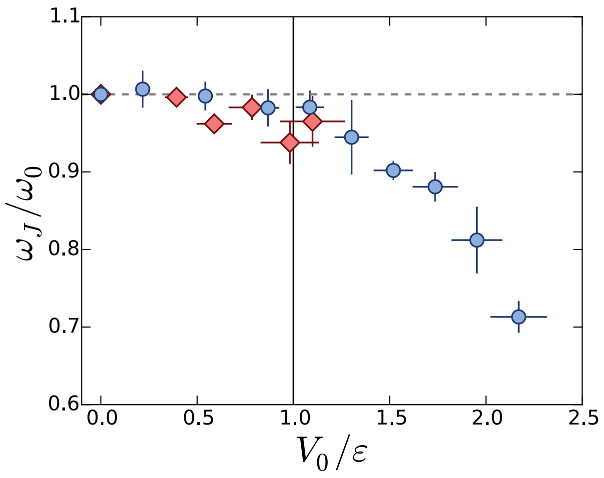

Figure 5.7 – Evolution of the frequency ω_J for increasing barrier height V_0 for a superfluid BEC (blue circles) and an ideal Fermi gas (red diamonds).

gun of macroscopic phase coherence in these systems due to a macroscopic condensate state, which can be directly probed and investigated by Josephson dynamics. Very interestingly, the Josephson effect couples an elusive quantity, such as the phase, to a more established or standard one, such as the particle current.

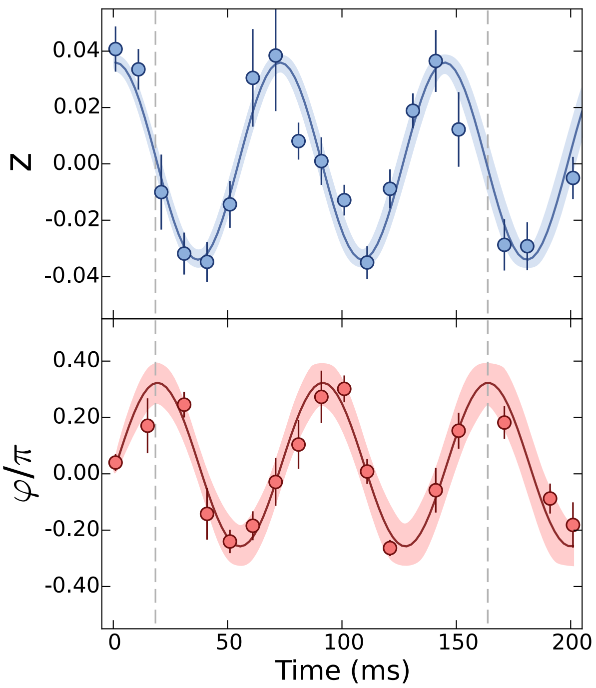

Figure 5.8 – Coupled dynamics of conjugated variables z and ϕ for a molecular BEC in the Josephson regime ($V_0 = 1.4(1)\epsilon$ or equivalently $V_0 = 1.0(1)\mu$). For the imbalance (phase), we measure a frequency ω_J of 13.9(0.1) Hz (13.8(0.2) Hz). The phase shift among the two observables is 1.1(0.1) $\pi/2$.

Beyond plasma oscillations

The previous section described the different dynamics in the tunneling regime ($V_0 \geq \epsilon$) among a superfluid and an ideal Fermi gas, which always displays for high barriers an exponential decay in the initial imbalance.

However, also for the superfluid BEC, the dynamics may turn (over)damped once the barrier is increased too much, as shown in fig.5.9, where the previously investigated plasma oscillations cannot be clearly detected anymore. In fig.5.7 the absence of experimental points for $V_0 > 2.2\epsilon$ is due to this kind of dynamics.

In our experimental configuration, the rise of V_0 is equivalent to diminishing the critical population imbalance z_C, above which the MQST dynamics is predicted. Unfortunately, the high interactions in the whole BEC-BCS crossover make the eventual amplitude of the MQST oscillations even smaller than those of the already investigated plasma oscillations [68], rendering their experimental observation unfeasible. The expected modulation should occur at higher frequencies, which are expected to be fractions of the chemical potential difference among the two reservoirs.

At best, the experimentally accessible imbalance dynamics can be generally described as an exponential decay with characteristic timescale increasing with the barrier height, due to suppression of tunneling. This is consistent with the considerations in section 2.4.1 about the metastability of the MQST regime due to non-vanishing role played by non-condensed particles [72] and topological defects nucleating at the barrier position [79, 80]. In particular, the role of these vortices would be further investigated below. In this regime, since the E_C starts to dominate over E_J, one expects the phase to evolve as $\hbar\phi(t) \simeq E_C z_0 N t$, linearly running in time. Due to the phase boundaries among [-π,π], a saw-tooth behavior is expected in the dynamics. For instance, the phase may initially

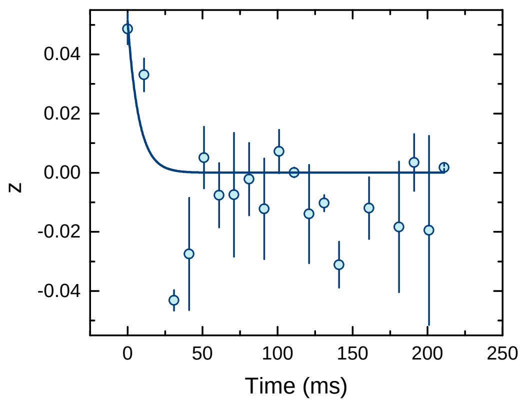

Figure 5.9 – Overdamped dynamics of a molecular BEC for $V_0 = 2.4(1)\epsilon$. A Josephson plasma oscillations is no more distinguishable.

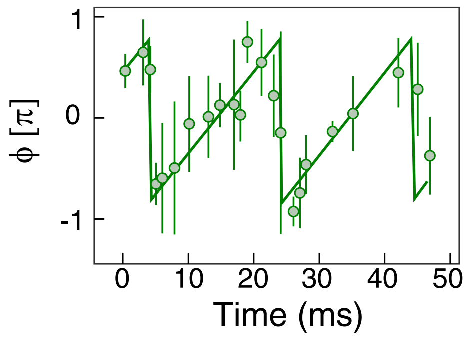

Figure 5.10 – Running phase for a molecular BEC at $V_0 = 3.3(2)\epsilon$. The extracted frequency is 45(2) Hz.

start from 0 and linearly increase till π, where a phase jump of 2π brings the phase to $-\pi$, where it starts running again till π and so on and so forth. For sufficiently high barrier, we confirm this theoretical expectation, as shown in fig.5.10.

In particular, during the first tens of milliseconds in the dynamics, we can trace the phase evolution and observe the saw-tooth behavior. In this time window, the imbalance does not show a distinguishable modulation and equilibrates towards zero at later times. Afterward, the phase evolution becomes to noisy and a clear trend cannot be distinguished anymore. The microscopic origins of these will be discussed in the following sections, however, as long as the frequencies are concerned, the initial dynamics allows to determine a frequency also in the running phase regime. Here, as we increase the barrier height, the frequency of the saw-tooth should approach the one given by the chemical potential

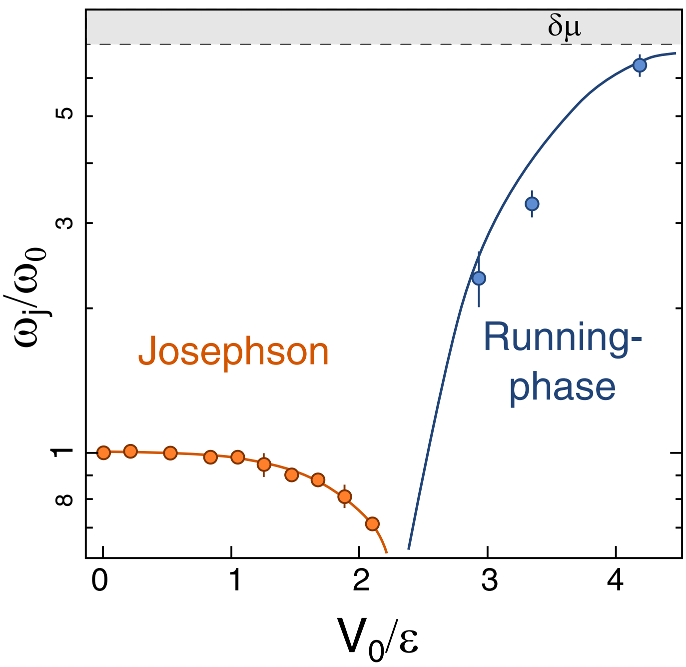

Figure 5.11 – Evolution of the frequency ω_J rescaled to the bare trap, both in the Josephson plasma and the running-phase regime, for different values of V_0/ϵ. Solid lines are guides to the eye.

difference among the reservoirs. We summarize our results in the figure 5.11, where the experimental determined frequency is plotted as a function of the ratio V_0/ϵ for the usual molecular BEC. This is analogous to the expectations for the MQST regime, but since we do not detect the typical MQST dynamics in the population imbalance and because of its exponential decay at longer evolution, we prefer to simply refer to this regime as the running-phase or dissipative regime.

For the data in fig.5.11, in the first part we observe the coupled plasma oscillations in both the imbalance and the phase, while for larger barrier we only detect a frequency from the phase pattern. As expected, this increases with V_0, approaching the value of 100 Hz set by our initial population imbalance. In the intermediate region, noise dominates over both the phase and the imbalance dynamics, limiting the determination of a clear frequency. However, despite our JJ being a multi-mode system, since many energy levels are occupied along the longitudinal trap axis ($\hbar\omega_0 \ll \mu$), a clear Josephson dynamics can be clearly distinguished in different regimes, in qualitative agreement with the ideal two-mode model expectations. Thus, our setup provides a good platform for extending the studies over weakly-coupled Fermi superfluids in different interaction regimes, starting from the direction paved by our investigation of a molecular BEC.

5.3 The Josephson effect across the BEC-BCS crossover

In this section we extend the investigation of Josephson dynamics to the whole crossover, focusing mainly on the comparison among the plasma oscillations. Again, the main reason for this is the determination of microscopic superfluid properties through the relation $\omega_J = \frac{1}{\hbar}\sqrt{E_J E_C}$. In particular, while the value of the charging energy E_C can be computed by state-of-the-art numerical simulations, the Josephson energy E_J, being proportional to the tunneling term, is more affected by the specific geometric properties of our JJ which, in addition to other microscopic features such as the condensate fraction and the pair-size, would make a dynamical numerical simulation extremely difficult to handle in the strongly interacting regime.

We start our comparison by moving from the deep BEC limit ($1/k_F a \simeq 4$) towards the unitary limit. In this framework, it is more convenient to express the barrier peak V_0 in units of the Fermi energy E_F of an ideal Fermi gas with the same trap potential and equal atom number. In this way, we have a helpful energy scale for the synopsis.

A first comparison is shown in fig.5.12, where the previous case of the molecular BEC at $1/k_F a \sim 4$ is compared with those of other superfluids with increasing interactions, till the Unitary Fermi gas (UFG) at $1/k_F a = 0$. Similarly to what happens for the molecular BEC, the other regimes show as well the usual trend for the plasma oscillations, with the

frequency bending down for increasing values of the barrier height.
However, an equivalent renormalization of the plasma mode requires a much higher V_0 when moving towards the center of the resonance on the BEC side. This can be understood in terms of the increase of the chemical potential towards the Unitary limit. Because of this, given a certain V_0, the ratio $V_0/\epsilon_{\mathrm{UFG}}$ for the UFG drops respect to $V_0/\epsilon_{\mathrm{BEC}}$ in the BEC limit. Looking back at the plot in fig.5.7, the increase of interactions is equivalent to reducing the ratio V_0/ϵ, so in this picture a plasma oscillation with a higher frequency is expected. In conclusion, on this side of the resonance, the bosonic character of the superfluid dominates. The increase of the particles energy requires a steeper barrier to significantly affect their motion, as in the textbook picture of single-particle tunneling.
For the relevant case of the UFG, we investigate also the evolution of the relative phase, which again is expected to be canonically conjugated respect to the imbalance [128]. However, in direct TOF images after release from the trap, a clear interference pattern as in the BEC case cannot be determined. This is mainly ascribed to strong interactions and collisions, which may scramble the phase during the overlap time [129].
To circumvent this issue, we perform a fast ramp on the BEC side during the expansion, significantly reducing the interactions during the TOF while increasing the contrast of the interference pattern. To enhance this effect, just for the phase measurement, we produce a resonant superfluid in the $|1\rangle$-$|3\rangle$ mixture, which features a Feshbach resonance with a reduced width of 180 G [25], requiring a smaller magnetic field jump from the UFG to the BEC limit. Moreover, because our Feshbach coils have a large inductance, we create an additional offset magnetic field with the smaller MOT coils, now flipped in Helmotz

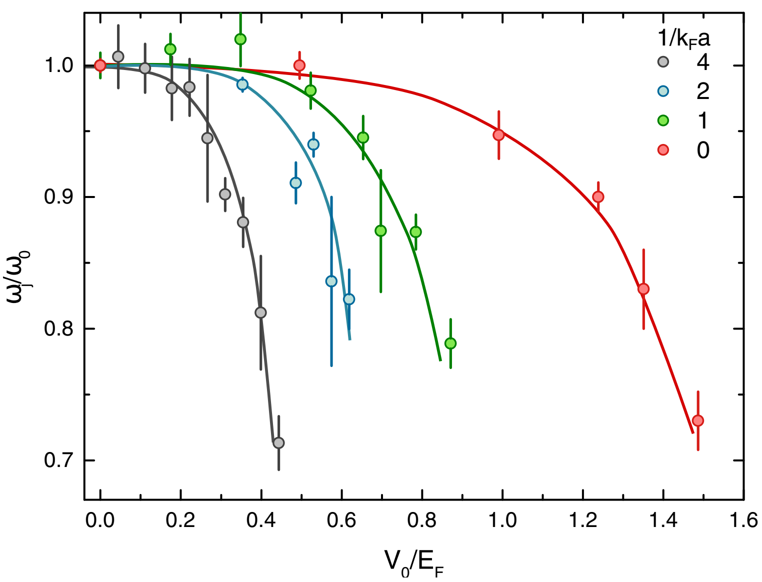

Figure 5.12 – Evolution of the plasma frequency for different regimes of $1/k_F a$ on the BEC side of the resonance for increasing values of V_0/E_F. Solid lines are guides to the eye.

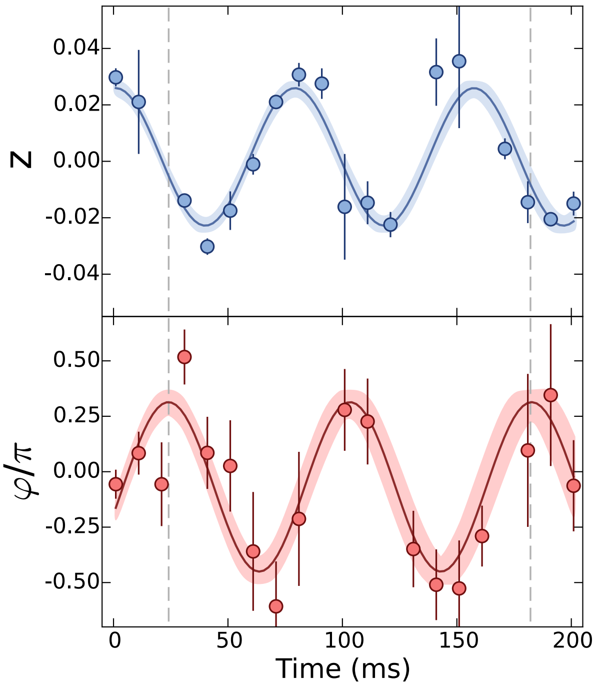

Figure 5.13 – Coupled dynamics of the imbalance (blue symbols) and the phase for a UFG. The two observables both show a sinusoidal oscillation. The evaluated frequency is of 12.8(0.1) Hz and 12.6(0.3) Hz for the imbalance and the phase, respectively. The relative phase shift among the two quantities is $\delta\phi = 1.2(0.2)\ \pi/2$.

configuration with the help of a relay switch. This allows a fast ramp ($t \sim 200\mu s$) from the Unitary limit (690 G for the $|1\rangle$-$|3\rangle$ mixture) till the BEC limit (620 G for this configuration). The comparison among the imbalance and the phase evolution is shown in fig.5.13 for a barrier height $V_0 = 1.0(1)\mu \sim \sqrt{\xi} E_F$, where ξ is the Bertsch parameter. Both quantities show the characteristic plasma sinusoidal oscillation, occurring at the same frequency within experimental uncertainty.

The measured relative phase shift is $\delta\phi = 1.2(0.2)\ \pi/2$, confirming the imbalance z and the phase ϕ to be canonically conjugated variables also for a UFG. As for the molecular BEC, this measurement is a direct proof of macroscopic phase coherence for this strongly interacting system.

Our investigation of the plasma excitations now moves to the BCS side of the resonance, as shown in fig.5.14. Here, despite the monotonous increase of the chemical potential, the slow plasma frequencies in the BCS regime stop drifting towards higher barrier heights. Respect to the UFG phenomenology, the plasma frequency in the deep BCS limit bends down for lower barrier potentials.

A zoom onto this behavior is shown in fig.5.15a, where the trend of the plasma frequency ω_J is compared for different interaction regimes across the resonance, for the same barrier height $V_0 = 1.2(1)E_F$.

As it can be seen, the trend of ω_J shown in fig.5.15a is non-monotonic, reflecting the tendency of the data in fig.5.14.
As long as E_C is concerned, we derive its value from an extended Thomas-Fermi model which takes into account the proper value of the chemical potential, obtained from QMC calculation. Further details on this theoretical model will be given below, however, this information, combined with the experimentally determined plasma frequency ω_J, allows us to extract the value of E_J, as shown in fig.5.15b. For comparison we plotted both E_J, determined in the $V_0 = 1.2(1)E_F$ case, and the value of $N \cdot E_C$ in units of E_F. As expected, being E_C related to the inverse of the compressibility of the gas, the quantity $N \cdot E_C$ monotonically increases across the Unitary limit. Instead, E_J reflects the up-and-down trend of the plasma frequency.
In the hydrodynamic limit, that is $V_0 \ll \mu$, a similar trend has been measured in the determination of the superfluid critical velocity across the whole crossover [55, 56]. This quantity depends on the energy spectrum of the system, which in the BEC regime is dominated by sound modes, while by pair-breaking excitations in the BCS limit. The critical velocity increases while moving towards resonance from the BEC regime and, just before reaching the $1/k_F a = 0$ point, it starts to decrease abruptly, due to the exponential lowering of the fermionic gap and the consequent emergence of the single-particle excitation branch.
Our measurements are instead carried out in the tunneling regime ($V_0 \geq \mu$), investigating over a coherent effect and avoiding the depletion of the superfluid fraction. On qualitative

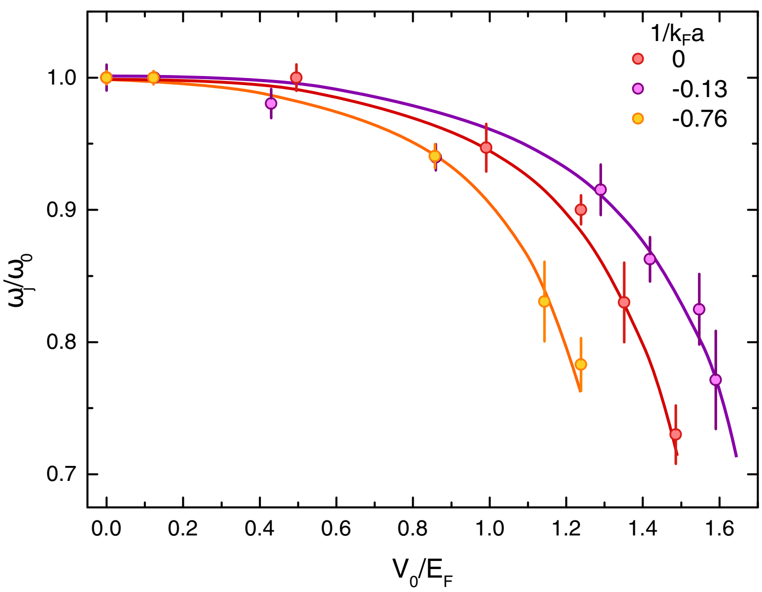

Figure 5.14 – Evolution of the plasma frequency for different regimes of $1/k_F a$ on the BCS side of the resonance for increasing values of V_0/E_F. Solid lines are guides to the eye.

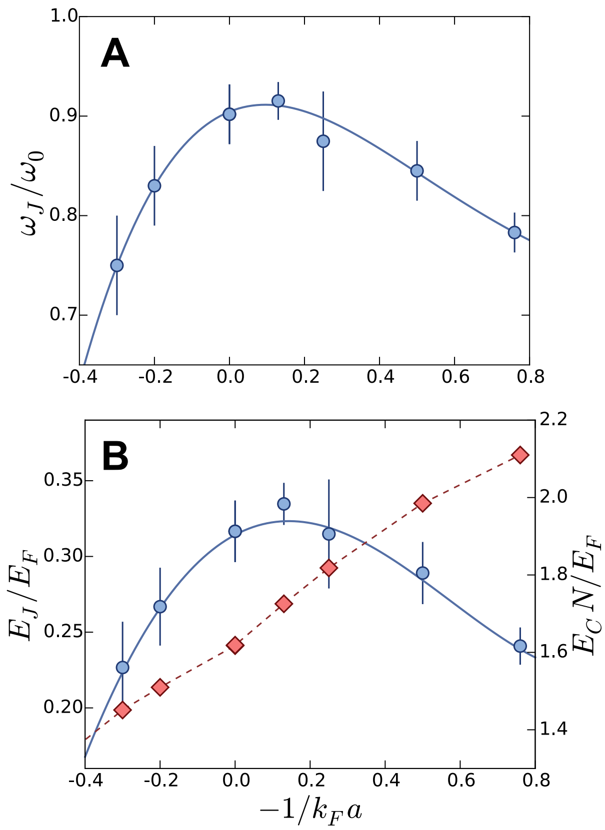

Figure 5.15 – a) Evolution of the plasma frequency across the UFG regime for a barrier height of $V_0 = 1.2(1)E_F$. b) Determination of the Josephson energy E_J (blue circles) from the computed value of E_C (red diamonds) and the measured value of ω_J (top panel).

arguments, one may expect:

$$E_J \simeq K N_0 \tag{5.6}$$

with K being the pair tunneling and N_0 the condensed fraction.

As explained before, on the BEC side, the increase of E_J can be understood as an increase of the tunneling term while approaching the resonance, since the barrier looks a smaller defect in this direction. In this regime, the condensed fraction slightly diminishes from unity. However, this is not true on the BCS regime where instead $N_0/N \propto \Delta/E_F$, reproducing the famed Ambeogaokar-Baratoff formula for conventional BCS superconductors JJs. The diminishing of E_J on the BCS side is so dominated by the depletion of the condensate fraction, due to the increasing fermionic character of the superfluid. Our results provide for the first time an alternative way to RF-spectroscopy for the determination of the BCS superfluid gap through tunneling experiments.

Interestingly, the determined E_J shows a peak value more shifted towards the BCS limit, differently from the results of the critical velocity [55, 56]. On a microscopic level, this should be referred to the increasing robustness of the so-called Andreev-Saint-James

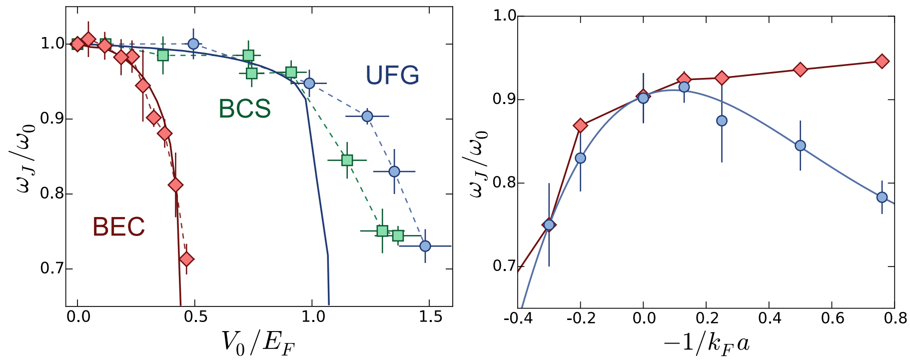

Figure 5.16 – Left: comparison among experimental plasma frequency (symbols) and ETFM model (solid lines) for three different interaction regimes, that is $1/k_F a$= 4 (red),0 (blue), -0.5 (green). Right: comparison among experimental (blue circles) and theoretical (red diamonds) frequency of the plasma oscillations across resonance for $V_0 = 1.2(1)E_F$.

bound states towards the unitary limit [130]. These bound states provide the microscopic mechanism for bridging two superconductors separated by a thin barrier [131]. Accessing and understanding the properties of these states in the strongly interacting regime is an active research line from both a theoretical and experimental point of view, also for the condensed matter community [132, 133]. Our results are just a first step in that direction.

Comparison with a laptop theoretical model

In our investigation, we compared our experimental results with those from a theoretical model that can run on a standard laptop, not requiring any particularly huge computational power, such as that of a supercomputer. This model is based on an extended Thomas-Fermi model (ETFM), where the Schödinger equation for the pairs wavefunction Ψ can be written as:

$$i\hbar\frac{\partial\Psi}{\partial t} = -\frac{\hbar^2}{4m}\nabla^2\Psi + 2V(x)\Psi + 2F(2|\Psi|^2)\Psi \tag{5.7}$$

where $V(x)$ is the overall potential (trap and barrier) felt by a single atom of mass m and $n = 2|\Psi|^2$ the total fermionic density. The non-linear coupling term F is defined as $F(n) = \frac{\partial\mathcal{E}}{\partial n}$, where $\mathcal{E}$ is the energy per particlewithin this model, whose value has been determined from an independent QMC calculation across the whole crossover [134]. This gives a different non-linear term any time we change the interaction parameter $1/k_F a$.
For instance, we used this model for defining a local chemical potential μ_{loc} and then for determining the charging energy E_C, in accordance to the relation $E_C = 2\frac{\partial\mu_{\text{loc}}}{\partial N}$.
Moreover, we used the ETFM for comparing its theoretical expectations with our experimental results, as it is shown in fig.5.16.

As it can be noticed, the theoretical model accurately reproduce the dynamics in the

BEC limit, as expected. For stronger interactions instead, the model doesn't reproduce correctly anymore the experimental observations. This is particularly highlighted on the right side of fig.5.16, where the situation of fig.5.15 is replotted. As it can be seen, the ETFM predicts a plasma frequency which monotonically increases through the crossover. The ETFM is a pure bosonic model, which lacks of the correct fermionic degrees of freedom on the BCS limit, that is the superfluid gap. The resulting inconsistency among our experimental results and those of the ETFM is actually expected, since the used theoretical model oversimplifies the rich structure of the crossover superfluids.

5.4 Quenching the superflow: dissipative dynamics and vortices

In the last discussion among the dynamics of a molecular BEC, we have seen the transition at high barriers from plasma oscillations to the dissipative regime, characterized mainly by a running-phase dynamics. However, the initial contrast of the phase trace is washed out as the evolution time increases. Generally, we observe always a high interference pattern in a single experimental run, but shot-to-shot fluctuations hinder the overall signal at longer times, making difficult to disclose again any trend in the phase evolution. At the same time, the initial imbalance has an exponentially decaying behavior, without any particular or measurable modulation on top of that.

We first try to observe if this running phase regime is also achievable for the UFG. We confirm this and show the evolution of the phase and the imbalance in fig.5.17a for a UFG at a barrier $V_0 = 2.0(1)E_F$. As expected, the phase evolution shows the mentioned running pattern at shorter time, becoming too noisy at longer ones. The imbalance, as for the molecular BEC case, shows instead a damped evolution. This is reminiscent of the discharge of a capacitor, with a resistive flow among the two reservoirs [127] which irreversibly tends to balance the initial chemical potential difference. We have so the unconventional situation of a resistive flow coexisting with a superfluid with a defined phase. We can so neglect pair-breaking excitations as the main mechanism of the superflow quench, since these would wash out phase-coherence at the single-shot level.

Rather, our phenomenology seems more connected to that of other neutral superfluids, such as the helium case. In these systems [6], the resistive flow is established by phase-slippage processes and consequent vortex nucleation in the tunnel link. In the running-phase regime, vortices are nucleated in the barrier region and then they annihilate any time the phase performs a full phase-slip, that is a jump of 2π. In the ideal MQST of the two-mode model, this would be a stable situation, with continuous and periodical creation and annihilation of vortices at the barrier region, that would prevent the imbalance

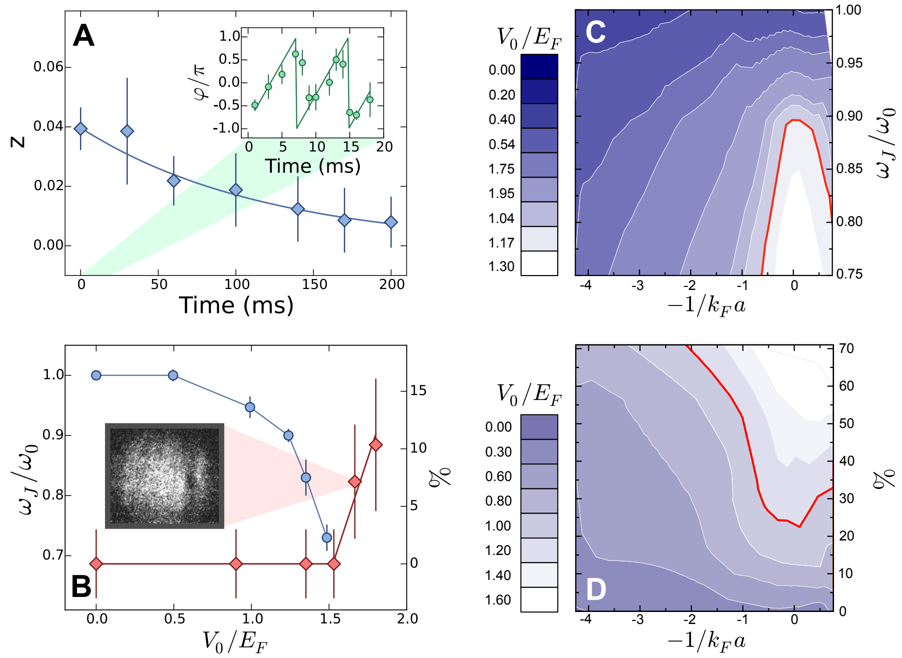

Figure 5.17 – a) Imbalance (blue diamonds) and phase (green circles in the inset) for a UFG at $V_0 = 2.0(1)E_F$. b) Evolution for a UFG of the plasma frequency (blue circles, left axis) versus occurrence of vortices in the bulk (red diamonds, right axis). c) Contour plot of the plasma frequencies across the whole crossover. The color code is the height of the barrier potential. d) Contour plot for the vortex occurrence across the whole crossover for an initial imbalance $z_0 = 0.12(2)$. The color code is the height of the barrier potential.

to equilibrate.

However, the strong interactions combined with the radial degrees of freedom of our junction may favor the leakage of vortices into the superfluid bulk. By taking out energy from the initial configuration at any phase-slip, the proliferation of vortices would result in the main mechanism for establishing the resistive flow among the two reservoirs.

For gaining more insights into this, we employ a different experimental procedure for disclosing the presence or not of vortices into the superfluid bulk. We trigger the dynamics at a given V_0 in the usual manner, but after a time of 50 ms we turn off with a linear ramp of 80 ms the barrier potential, a timescale essentially adiabatic with the longitudinal trapping period. Then, we sweep the magnetic field in 10 ms to the BEC limit and look at the density profile in TOF. Vortices would result as a dip in the density profile of the expanded cloud [121].

As shown in the inset of fig.5.17b, a density depletion in the density distribution actually may show up. We further characterize the presence of these topological defects by a statistical analysis over 40 different experimental images in the same condition, for different values of the barrier height. As summarized in fig.5.17b for a UFG, vortices appear only in the regime where plasma oscillations are absent.

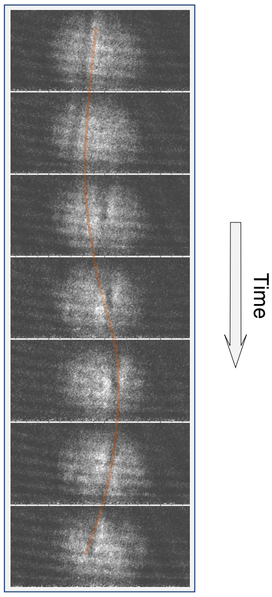

Figure 5.18 – In trap oscillation of a topological defect in the Unitary limit. Time increases from top to bottom. Solid orange line is a guid to the eye.

This further confirms the breakdown of Josephson oscillations by the appearance and proliferation of such defects. This interconnection is actually extended to the whole crossover picture. This is summarized in the figures 5.17c and 5.17d, where the trend of the Josephson oscillation is compared to the occurrence of vortices for different interactions regimes and barrier potentials. As it can be seen, the occurrence of vortices mirrors the trend of the ω_J frequencies, with resonant superfluids being more robust to vortex proliferation while maintaining the higher values of plasma frequency.

To further characterize the nature of these defects, we let them oscillate in the trap once they are created, by increasing the time among the barrier removal and the Feshbach sweep and the followig detection. As it can be seen in fig.5.18, the trapping potential induces an oscillatory dynamics on these defects.

As plotted in fig.5.19, the period of their in trap oscillation drastically increases when moving from the BEC to the BCS limit. This is consistent with the defect being a solitonic vortex [135], since its period is expected to follow the trend of the chemical potential across the BEC-BCS crossover. However, this defect may actually be the result of a cascade process from a vortex ring, initially created inside the barrier region [136], but becoming unstable while propagating inside the bulk. Further studies are however needed to confirm this, but also to further characterize the rich phenomenology arising from the interplay among elementary and topological excitations in the onset of dissipative flow.

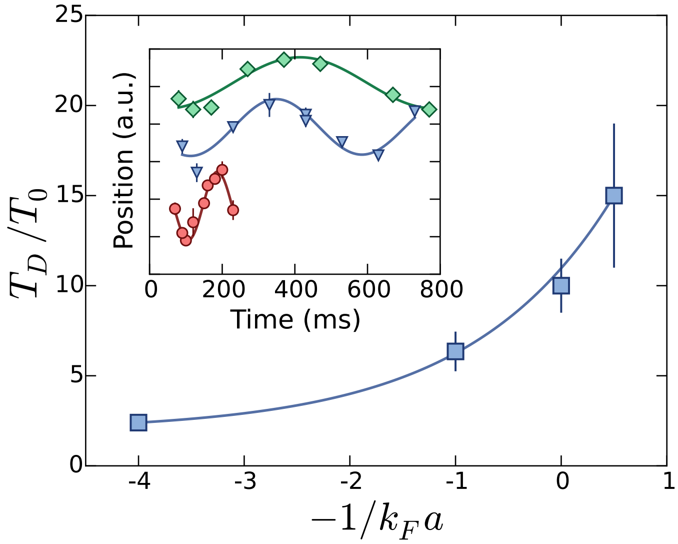

Figure 5.19 – Evolution of the oscillation period of the topological defects across the whole crossover. Inset: typical in trap dynamics for the vortex oscillations at $1/k_F a$= 4 (red circles), 1 (blue triangles), 0 (green squares).

5.5 Outlook: dissipation and thermodynamics

We reported in the previous sections about the investigation of coherent dynamics in strongly interacting Fermi gases, focusing first on the regime of small oscillations and then on the transition to the dissipative dynamics and the creation of vortices by phase-slips.

Here, we instead study the regime of high population imbalance for barrier heights of the order of the energy per particle of the system, to perform a more thorough characterization of the dissipative dynamics. We expect the junction not to sustain oscillations at large imbalance, since the initial chemical potential drop across the barrier should allow a coupling to the radial modes, with a resulting damping of the initial dynamics and a quench of the superflow. In this framework, understanding how a superfluid is affected and eventually impeded by an obstacle is a fundamental question dating back to the early days of investigation of superfluid dynamics [137–139]. In particular, we want to investigate how the creation of topological defects tangles with the coherent flow.

The experimental procedure we developed for these studies is a slight modification of that in fig.5.4. Previously, we started the experiment with the trap center a bit displaced from the barrier position, and then we triggered the particle tunneling by non-adiabatically getting back to the equilibrium position. Now, since we want to deal with higher initial imbalances ($z \geq 0.2$), the initial displacement would be large, in the tens of μm. The non-adiabatic movement would so result in a large perturbation, with direct excitation of

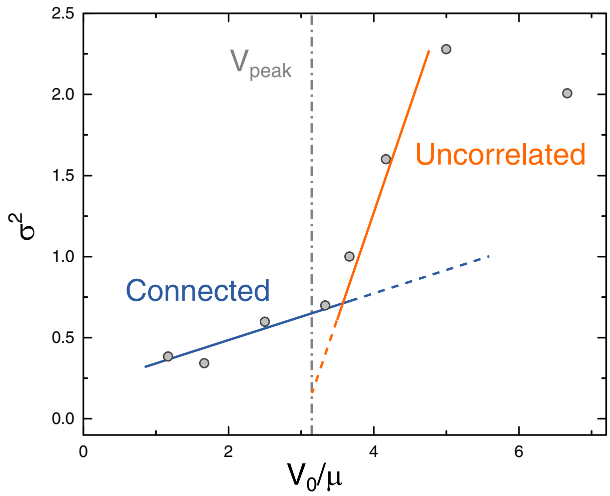

Figure 5.20 – Standard deviation of the phase measurement at $t = 0$ for a molecular BEC versus the barrier height V_0. At a barrier $V_0 > 3\mu$, we observe an increase in the shot-to-shot fluctuations. We ascribe this to the transtion to two uncorrelated condensates. The gray dashed-dotted line marks the peak value of V_0 during the separation procedure. Blue and orange solid lines are guide to the eye to mark the regimes of connected and uncorrelated superfluids, respectively.

breathing modes and heating of the superfluid. After finishing the evaporation, we raise the barrier height to a value generally of the order of four times the chemical potential, by a linear ramp of 30 ms duration. After this, we readjust the trap center back onto the barrier through a 120 ms ramp in the *IPG*'s AOM RF-signal. This creates a junction with a tunable and large chemical potential difference among the two reservoirs, without exciting any sloshing or breathing mode. The dynamics is then triggered by linearly decreasing the barrier from the peak value to the target one in 5 ms. First, we checked this procedure to effectively give the same results about the Josephson plasma oscillation, both in the imbalance and in the phase, as previously discussed. Second, we also controlled that the peak value reached by the barrier during the trap readjustment would not result in the disconnection of the two superfluids. If this would be the case, any of the two condensate would freely evolve in each reservoir, resulting in a considerable increase of the noise on the phase measurements due to shot-to-shot fluctuations. We observed that the standard deviation on the phase measurement remains low for the barrier heights employed during this procedure, considerably increasing only for barrier heights much higher, as reported in fig.5.20. This increase marks the transition to two uncorrelated superfluids [140].

With this starting configuration, we investigate how the current flow is affected by the initial population imbalance z_0, now set to a higher value respect to the former investigation of the Josephson oscillation, that is $z_0 > 0.05$. A typical evolution of this is shown in panel 5.21 for a UFG at a barrier $V_0 = 1.0(1)\mu$. Similar trends can be obtained as well for the other superfluid regimes.

The dynamics in this scenario looks more complex than in the previous experiments. When increasing the imbalance from $z_0 > 0.05$, we observe that the junction cannot sustain anymore an undamped oscillation as in fig.5.8 and 5.13. For the data in fig.5.21a-c, the evolution of z follows a fast initial decay towards zero. However, after this first transient, an oscillatory dynamics is observed at longer evolution times. Within our experimental uncertainty, this restored oscillation happens at the same frequency of the small imbalance case at a certain V_0 (see for instance fig.5.12). As well, their amplitude is in the same range of the plasma dynamics. After an initial damping the junction is able to restore the typical Josephson oscillation, dissipating away the excess energy introduced by the large initial imbalance.

Interestingly, when z_0 is further increased as in fig.5.21d, the flow evolution changes again, with the curve now describable just in terms of a simple exponential decay with a long timescale and no revival of the oscillatory trend. For the entire duration of the experimental run, we observe only a resistive flow, with a leakage of particles from one reservoir to the other.

Similarly to the investigation in [141], we derive the particle current through the barrier for the data in fig.5.21. The particle current is defined as the time derivative of the imbalance behavior. For a more accurate determination of the current, we fit the curves in fig.5.21a-c and similar with an exponential decay plus a sinusoidal oscillation, while for the data analogous to fig.5.21d we employ a single exponential. The analytic time derivative of this curves will give us the mean current through the barrier, which is connected to the amount of energy dissipated by the junction through the particle flow. For an exponential decay with a timescale τ, the current would be expressed simply as z_0/τ, while a sinusoidal term would not contribute to the mean current.

The results from this analysis are displayed in fig.5.22. It can be noticed that the current as a function of the initial imbalance has a non-monotonic behavior. For the case of fig.5.21, the current linearly increases for small imbalances, while abruptly diminishing at $z_0 \simeq 0.25$. After this drop, the current increases again but with a softer slope. The fast slope is associated to the ability of the junction to dissipate the excess imbalance in the first times of the dynamics, meaning a small τ in the expression for the current. When the system cannot efficiently dissipate the energy associated with z_0, the equilibration time increases, as observed in fig.5.21d, with a corresponding drop of the current.

This current trend is strongly affected by the barrier height V_0. For higher V_0, the first fast increase in the current in fig.5.22 is shrank in a smaller imbalance range, with the current drop occurring at an always smaller z_0. Eventually, for higher barrier only an exponential decay is observed, without the possibility to distinguish anymore an oscillation, neither the restored one nor the direct plasma one.

This non-monotonic behavior of the current can be observed for different superfluids, as

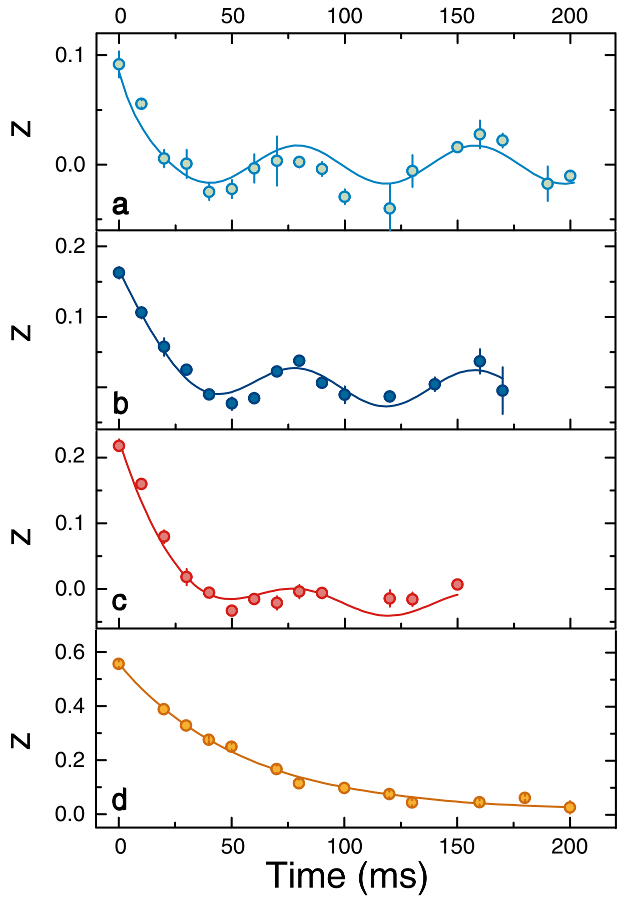

Figure 5.21 – Evolution of the current for a UFG at a barrier of $V_0 = 1.0(1)\mu$ for different initial imbalances. From top to bottom: a) $z_0 = 0.09(2)$, b) $z_0 = 0.16(3)$, c) $z_0 = 0.23(3)$, d) $z_0 = 0.54(4)$,

shown in fig.5.23a for a molecular BEC at $V_0 = 0.9\mu$. This is accompanied in fig.5.23b by the investigation of the vortex occurrence after 40 ms of the dynamics with the technique described in section 5.4.

For the case of fig.5.23 we can distinguish three different regimes as a function of the initial population imbalance. For $z_0 < 0.1$ we recover the usual undamped plasma oscillation, whose mean currents averages to zero and with no observation of topological defects in the bulk. We identify this with the Josephson regime. With the imbalance in the range $0.1 < z_0 < 0.35$, we enter the same dynamical regime of fig.5.21a-c, with a first initial damping and a restoring of plasma oscillations. This leads to a first increase of the mean current and to the appearance of a moderate number of defects into the bulk, that is the vortex detection probability increases with z_0 but stays below 30%. For a further increase of z_0 above 0.35, the transition to a more dissipative dynamics as in fig.5.21d is followed by a huge increase of the production rate of this topological defects, even with a possibility of observing more than one vortex in the same experimental shot.

As previously discussed, vortices appear only if the dynamics has a decaying part in the

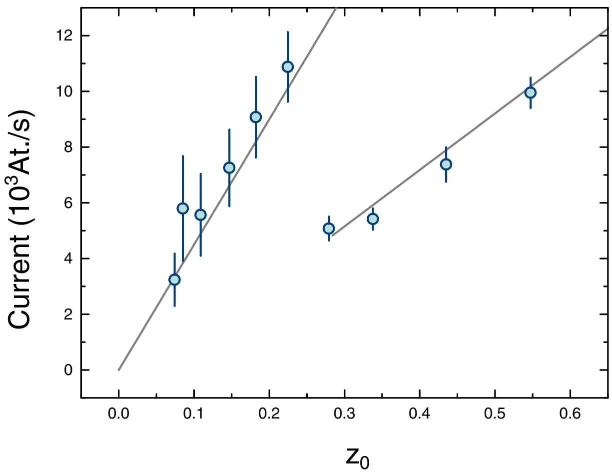

Figure 5.22 – Current through the junction as a function of the initial population imbalance. Solid lines are guide to the eye.

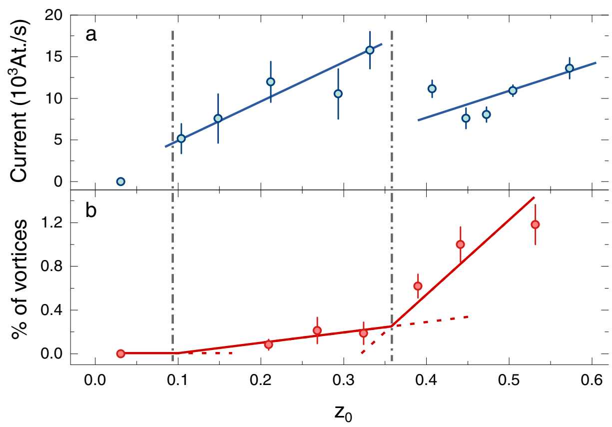

Figure 5.23 – a) Current versus initial imbalance for a molecular BEC at $V_0 = 0.9\mu$. b) Occurrence of vortices after 30 ms of dynamics. Solid lines are guide to the eye. Dotted dashed lines mark the transition to a different dynamical regime: $z_0 < 0.1$ plasma oscillations and no vortex; $0.1 < z_0 < 0.35$ revival of oscillation and few vortices; $z_0 > 0.35$ dissipative current and several vortices

particle flow. This means that the junction tends to balance the population difference by dissipating the excess energy through phase-slips and vortex nucleation. If the initial imbalance difference is moderate, the system rapidly dissipate the excess energy and after this, the coherent flow regime is re-established, with a consequent revival of the plasma oscillations. When instead, the excess energy is too high, the system cannot easily dissipate the initial chemical potential difference in a fast way, with a likely accumulation of topological defects inside the bulk, which completely scamble the phase correlations, preventing the observation of Josephson dynamics.

Interestingly, within our resolution we do not detect a significant increase of the temperature associated to the nucleation of vortices, even if the dissipative normal currents that are observed should introduce as well a local heat transport, which may compete with the

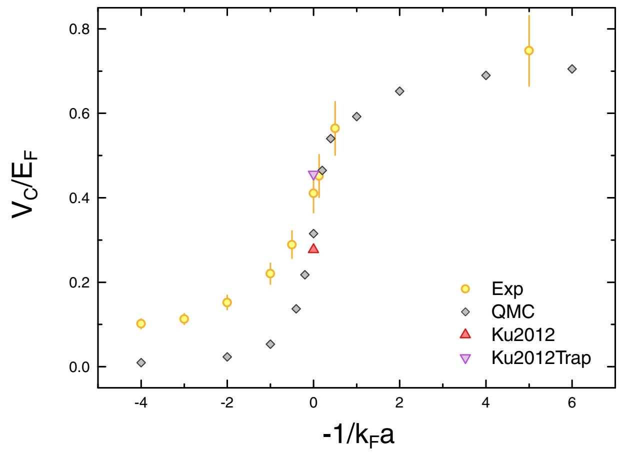

Figure 5.24 – V_C across the BEC-BCS crossover (yellow circles) compared with the EOS for a homogeneous system from QMC calculations (gray diamonds) [142]. The experimentally measured [25, 122] energy per particle for a UFG is displayed, both for the homogeneous case (red diamond) and the trapped one (purple inverted diamond).

vortex proliferation to the quench of the superfluid flow.

5.5.1 Connecting tunneling experiments with thermodynamical quantities

This section develops after a phenomenological interpretation of the imbalance dynamics at different barrier height V_0. This is connected to the onset of the dissipative dynamics, that is the one describable with a single exponential decay as in fig.5.21d. For a vanishing barrier $V_0 \ll \mu$, this dissipative dynamics is never observed, even for very initial z_0. The current always sustain some oscillatory behavior, despite an additional damping. The monotonic exponential decay in the large imbalance regime ($z_0 \leq 0.5$) shows up only above a critical value V_c of the barrier.

The experimental trend of V_c is plotted in fig.5.24 across the whole BEC-BCS crossover in units of E_F. This quantity increases monotonously from the BEC regime up to the BCS side. This is somehow an expected feature, since the chemical potential increase along the same direction makes a robust barrier on the BEC side look like a small perturbation for a BCS Fermi superfluid, (see discussion in 5.3). However, the value of V_C is quite close to the value of the equation of state evaluated by QMC calculations in [142] across the whole interaction regime for a homogeneous system. We already saw that for a molecular BEC the non-trivial superfluid dynamics is accomplished only for $V_0 \geq \epsilon$, with a significant renormalization of the plasma frequency ω_J respect to the bare trap one. Our tentative interpretation for the closeness of V_C to the energy per particle ϵ is that the barrier acts as a sharp knife edge in the energy space. When the barrier height is below the mean energy, some particle may still perform an oscillation on top of that, while for higher barrier this is impeded. Ideally, one would like to use the barrier as a local probe of the density of states of the two superfluids, establishing a closer connection with tunneling experiments in condensed matter [132]. However, one should avoid the inhomogeneity given by the conventional harmonic traps, which hinder the local signal. The recent implementation of flat box potential in quantum gases experiments [143] should allow to overcome this limitation, making feasible for instance the measurement of the superfluid gap on the fermionic side of the Feshbach resonance exploiting the so-called Giaver tunneling [39].

CHAPTER 6

Probing the magnetic properties of repulsive normal Fermi gases

We show in this chapter our results over the investigation of normal Fermi gases on the upper branch of a Feshbach resonance. Differently from the previous Josephson dynamics, here we access the regime of strong repulsion among fermions with different spin. As a consequence, we target the problem of the emergence of the ferromagnetic instability in a repulsive Fermi gas.
Our main findings have been collected in the following paper:

- G. Valtolina, F. Scazza, A. Amico, A. Burchianti, A. Recati, T. Enss, M. Inguscio, M. Zaccanti & G. Roati, *Evidence of ferromagnetic instability in a repulsive Fermi gas of ultracold atoms*. In preparation.

Here, an extended description will be given about the experimental setup and techniques employed for this investigation.

6.1 Producing an artificial atomic ferromagnet

The Stoner model represents a milestone in our understanding of a variety of systems which owe their magnetic properties to delocalised fermions. Despite its simple and mean-field arguments, this model in his first formulation [9], predicts the occurrence of a ferromagnetic instability in a homogeneous electron gas with sufficiently strong, short-ranged repulsive interactions. The Stoner's picture nowadays still holds only at the qualitative level, since more rigorous approaches confirm Stoner's expectations but differ in the quantitative results about critical interactions and temperature.
Unlike their solid-state counterparts, quantum gases experiments arise as an ideal platform for confirming the theoretical predictions, without the detrimental disorder and lattice structure, typical of condensed matter, that would hinder the comparison among microscopic theories and experiments.

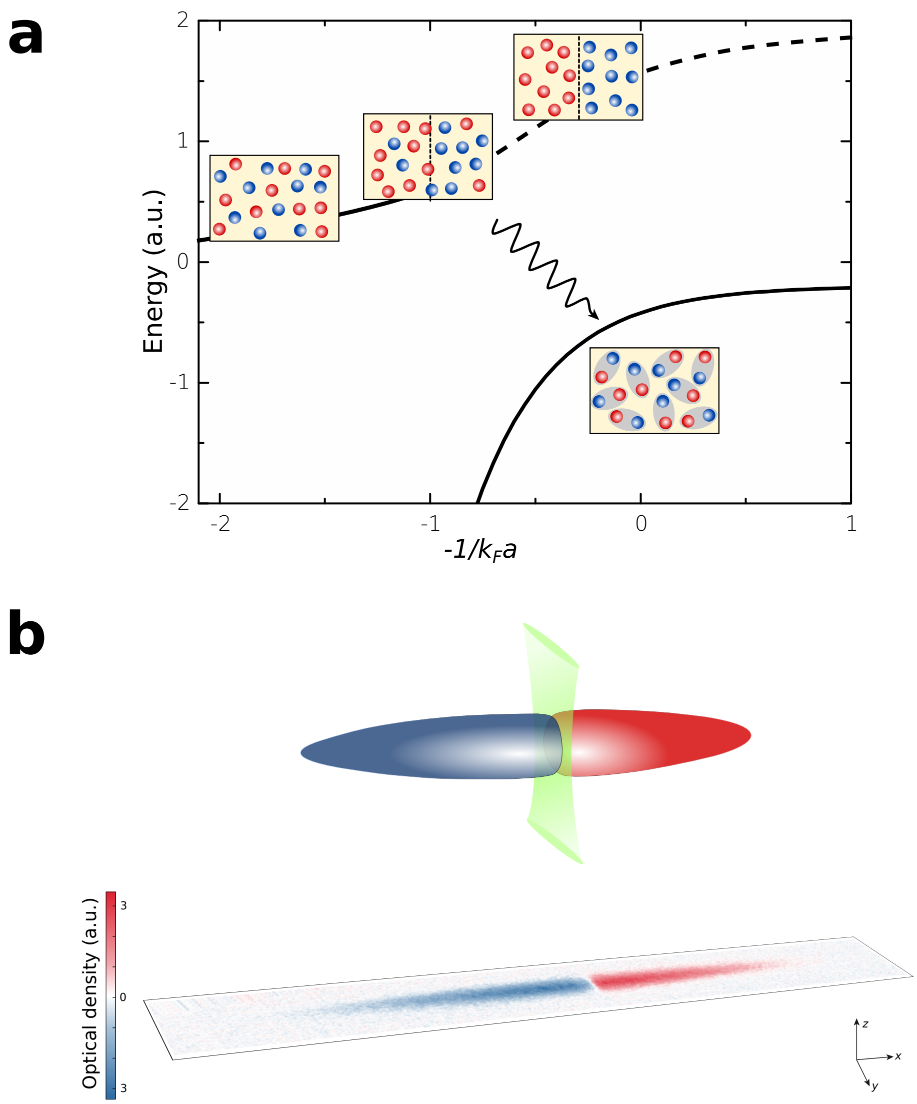

Figure 6.1 – a) Sketch of the upper and lower branch of the many-body system. On the upper branch, the repulsive gas may turn ferromagnetic but it has to compete with relaxation onto the lower branch. b) Concept of the experiment: realization of two spin-polarized Fermi gas separated by a thin optical barrier (experimental signal below), which would allow to beat detrimental losses due to decay from the upper to the lower branch.

So far, the Stoner model has been investigated in atomic gases starting from a paramagnetic weakly-interacting mixture by quenching interactions using a Feshbach resonance [10]. One would expect the Fermi gas to stay, while interactions are ramped up, always on the upper branch of the many-body picture, realizing a truly repulsive Fermi gas that may show a magnetic phase above some critical parameter. However, when interactions are quenched starting from a paramagnetic mixture, the pairing instability dominates over the ferromagnetic one, hindering the emergence of any magnetic correlation. This has been the subject of a deep investigation, both theoretical [144] and experimental [11], which ruled out the appearance of any ferromagnetic transition in such a configuration.

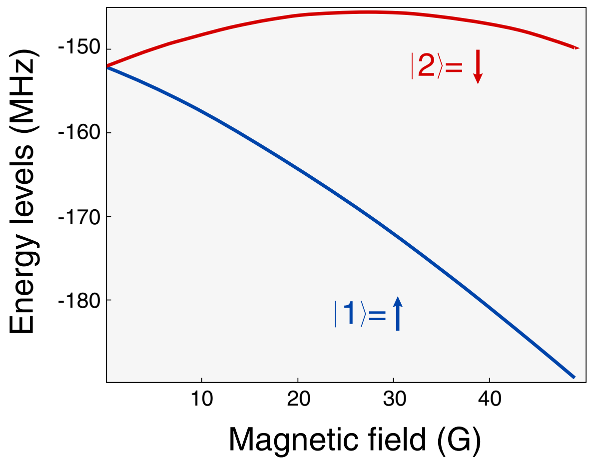

Figure 6.2 – Energy level dependance at low magnetic fields of the lowest two states $|1\rangle$ and $|2\rangle$ out of the six given by the hyperfine manifold. Below 10 G, the two magnetic moments have opposite sign with almost equal amplitude.

The general question "Can a homogeneous Fermi gas with short-range interactions turn ferromagnetic?" has not a conclusive answer yet.

Stimulated by this, we investigate this problem in the same physical system, but with a different initial approach. To overcome the pairing instability, we implemented an experimental procedure for splitting two atomic Fermi gases with different spin into two disconnected reservoirs, as depicted by the cartoon in fig.6.1b. The barrier in this scenario acts as an infinite repulsive wall, preventing undesired tunneling. In this way, since now the two spin-polarized Fermi gases do not interact, approaching the Feshbach resonance by a magnetic field sweep would not result in any molecule formation before having triggered the relevant dynamics. Hopefully, by removing the barrier after having reached a target interaction strength, the dynamics would be dominated only by the effective repulsion among atoms on the upper branch of the system, beating so the detrimental pairing mechanism.

For achieving this goal, we first produce a normal Fermi gas by forced evaporation at 300 G. As explained in section 4.2, by a suitable choice of the hyperfine levels, we can reach temperatures lower than 0.10 T_F. However, for performing the anticipated spin separation, we always need atoms to be equally distributed among the states $|1\rangle$ and $|2\rangle$ of the hyperfine manifold. The reason is hidden in the magnetic field response of these hyperfine states. As shown in fig.6.2, at low magnetic field, that is $B \leq 10$ G, the energy dispersion of $|2\rangle$ has a low-field seeking behavior, differently from that of $|1\rangle$. Consequently, the application of a magnetic field gradient at this offset field would result in a force with opposite directions for the atoms in these two levels.

A balanced and normal Fermi gas in the $|1\rangle$-$|2\rangle$ mixture is so very needed. Generally, when evaporation is accomplished in the $|1\rangle$-$|3\rangle$ mixture, the $|3\rangle$ state is flipped into $|2\rangle$

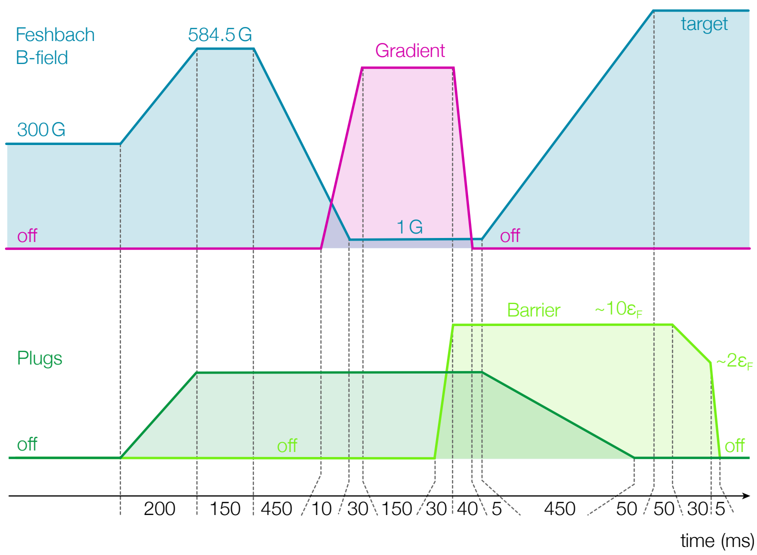

Figure 6.3 – Experimental sequence for separating the two spin domain on different sites of the trap, showing the ramps for the Feshbach field (blue), the magnetic gradient (purple), the plugs (dark green) and the barrier (acid green). The barrier removal ramp is that for the spin diffusion measurements.

by a RF π-pulse. This lasts 100 μs and it is applied at a field around 584 G for reducing interaction effects during the transfer. With a $|1\rangle$-$|2\rangle$ mixture finally in the trap, we reduce the offset field till a value of 1 G with a linear ramp of around 500 ms. Then we apply the magnetic field gradient for spatially separating the atoms. The gradient is linearly turned on in 40 ms till a peak value of 1 G/cm. After 150 ms the overlap of the two cloud is zeroed. We so raise the barrier in the center of the trap by a linear ramp of 30 ms, till a peak value of $V_0 \simeq 10E_F$. With such a high barrier potential, we do not observe at all tunneling of atoms for several seconds. Once the barrier separates the two spin clouds, we gently reduce the gradient and increase through a 500 ms linear ramp the Feshbach field till the target value.

While the gradient is on, for avoiding significant spilling of atoms from the trap, we turn on two additional plug beams, always at a wavelength of 532 nm and with a short (long) waist of 50 (120) μm along the longitudinal (gravity) trap axis. They create an additional repulsive potential on the edge of the trap, preventing the atoms from being spilled. The plugs are raised before lowering the magnetic field to 1 G and turned off while this last is increased.

By performing a round-trip similar to what usually done with optical lattices, we check that no significant heating occurs. We separate the atoms as explained before and we raise the field to 300 G. We measure the density distribution by absoprtion imaging after 5 ms of TOF. After the separation procedure, this is accomplished by turning off the barrier in the trap center through a 50 ms linear ramp, always performed at an offset field of 300 G. Once the cloud has occupied the overall trap volume, we observe again the typical

Fermi-Dirac distribution, with a fitted temperature equal within our experimental uncertainty to that measured just after evaporation. The separation induces however a 20% losses in atom number. Since we do not detect an increase of the degeneracy parameter T/T_F, we argue this procedure to spill just the hotter atoms at the trap edges, where the gradient effect is more pronounced.
After this, the pictorial representation of the system we deal with is extremely close to the expected ground state of an eventual ferromagnetic phase. This "adiabatic" realization of the spin domains allows to target a certain Feshbach field, that is a certain $k_F a$, without exciting any breathing or density modulation over the clouds. Importantly, the raising of the magnetic field does not result in any molecule formation while the barrier is still high. Once this is removed, our non-interacting Fermi gases will be projected onto the many-body scenario, that may result in the occupation, even if for a limited amount of time, of the real upper branch of the system, without the presence of preformed molecules. Our initialization in a domain-wall configuration would result in an ideal platform for the investigation of Fermi gases with resonant **repulsive** interactions, reducing those detrimental mechanisms that tend to depopulate the upper branch.

6.2 Magnetism 1.01: The spin-dipole mode softening

Collective modes are a powerful tool for addressing the excitation spectra of a system but also for disclosing the response of this to a small perturbation. Here, we investigate the evolution of the spin-dipole mode in a repulsive Fermi gas as a function of interactions. This mode is defined as the out-of-phase oscillation of two spin components. Being so related to a spin perturbation, it is a sensitive probe for disclosing a magnetic instability, similarly to the measurements of spin fluctuations.
In this framework, the sum-rule approach is a powerful method for evaluating an upper bound of collective modes excited by a small (linear response regime) perturbation. By using such a method [145], the frequency ω_{SD} of the spin-dipole mode can be valuated from the following formula:

$$\hbar^2 \omega_{SD}^2 \leq \frac{m_1}{m_{-1}} \tag{6.1}$$

where $m_k = \sum_n |\langle 0|D|n\rangle|^2 (E_n - E_0)^k$ are the moments of the strength distribution function, or sum rules, connected to the perturbation operator D. For the case of the spin-dipole mode, we have $D = \sum_{i\uparrow} z_i - \sum_{i\uparrow} z_i$, where z_i is the longitudinal coordinate along the trap axis.
Importantly, eq.(6.1) gives an upper bound to the lowest energy out-of-phase mode excited by D [145]. In this case, the direct energy weighted m_1 moment can be calculated from commutators algebra, giving $m_1 = N \frac{\hbar^2}{2m}$, while the formula for the inverse energy weighted

term m_{-1} reads as:

$$m_{-1} = \frac{1}{2}\int d\mathbf{r}\, z^2 \chi(n) \tag{6.2}$$

with n the density and χ the spin susceptibility.
Inserting this in eq.(6.1), gives:

$$\hbar^2 \omega_{SD}^2 = \frac{N}{2\int d\mathbf{r}\, z^2 \chi(n)} \tag{6.3}$$

This allows to write down:

$$\frac{\omega_{SD}^2}{\omega_0^2} \simeq \frac{\chi_0}{\chi(n)} \tag{6.4}$$

where χ_0 is the spin susceptibility of the ideal Fermi gas. For clarity, the density averaging has been omitted in eq.(6.4).
The frequency of the spin-dipole mode univocally connects us to the measurement of the spin susceptibility, that quantifies the tendency of the system to turn ferromagnetic. In a homogeneous system the spin susceptibility χ is expected to diverge towards the ferromagnetic transition, signaling the occurrence of the magnetic instability. In accordance with eq.(6.3), This would lead to a lowering, or more correctly, to a softening of the spin-dipole mode at the ferromagnetic transition. Given the coupling among this collective excitation and the spin susceptibility, the observation of the spin-dipole mode softening would translate into a direct proof of the occurrence of a ferromagnetic instability.
The relation expressed by eq.(6.3) is valid only below the ferromagnetic transition, since the sum-rule approach is alowed only for normal Fermi liquids, that is for a repulsive gas in a paramagnetic phase. How the frequency ω_{SD} evolves above the transition is not know yet and cannot be inferred with the previous methods.
In an atomic gas experiment, where atoms are held in harmonic potentials, the trap inhomogeneity would shrink the region of a diverging susceptibility only towards the trap center. This would result in a renormalization of χ, lowering its divergence. As a first consequence, the spin-dipole frequency would not decrease to zero at the critical interaction, but a significant deviation from the trap frequency is still expected [145].

Effective Fermi energy and wavevector

Accounting for the trap inhomogeneity, we redefine the length and energy scales of the system by a suitable trap averaging. We substitute the peak values of k_F and E_F with the effective ones in the trap κ_F and ϵ_F, which are defined as it follows.
First, we approximate the density distribution of a Fermi gas of N atoms in half a harmonic trap as half of the distribution of a $2N$ particle Fermi gas, spread all over the trap potential, neglecting de facto the presence of the barrier. Given the atom number, the

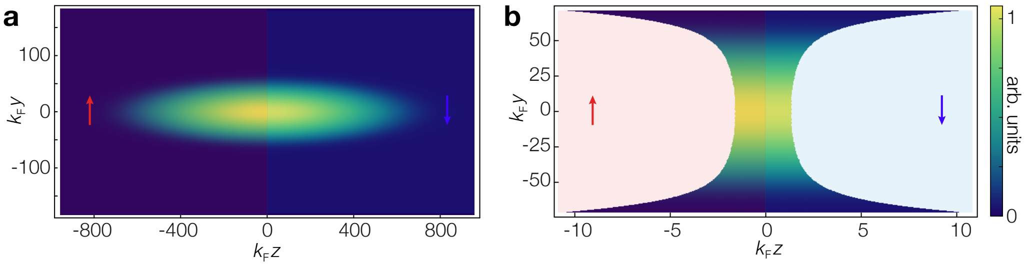

Figure 6.4 – Model for the definition of κ_F and ϵ_F. a) Effective density distribution of the cloud. b) Mean interparticle spacing at the interface.

trap frequencies and the finite temperature of the cloud, we use the usual Fermi-Dirac distribution $n_F(\mathbf{r}, T/T_F)$ for evaluating the density profile. After this, the local Fermi momentum reads as $k_F(\mathbf{r}, T/T_F) = (6\pi^2 n_F(\mathbf{r}, T/T_F))^{1/3}$ and the local Fermi energy as $E_F(\mathbf{r}, T/T_F) = \hbar^2 k_F(\mathbf{r}, T/T_F)^2/2m$. The rescaled Fermi momentum κ_F is so defined by averaging $k_F(\mathbf{r}, T/T_F)$ over a small volume around the trap center, that is at the barrier position at $z = 0$. This volume extends for one interparticle spacing $(6\pi^2/k_F(x, y, 0, T/T_F)$ along the overall radial extension of the cloud, as shown in fig.6.4. The parameter ϵ_F is defined in the same way.

We introduce this rescaling since the dynamics we probe is that of the overall interface among the two spin domains. Averaging over this region gives us the effective energy and length scales of our system.

6.2.1 Measurement of the spin-dipole mode

For measuring the spin-dipole mode, we use the same experimental scheme of fig.6.3 for initializing the system in the domain-wall configuration. The only difference is related to the barrier removal.

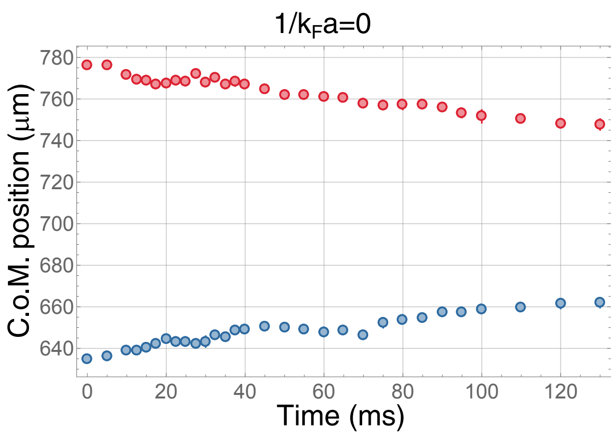

Figure 6.5 – Time evolution of the center of mass (C.o.M.) of the two clouds after removing the barrier. The spin dipole dynamics is obtained by subtracting the blue data (spin ↑ cloud) from the red data (spin ↓ cloud).

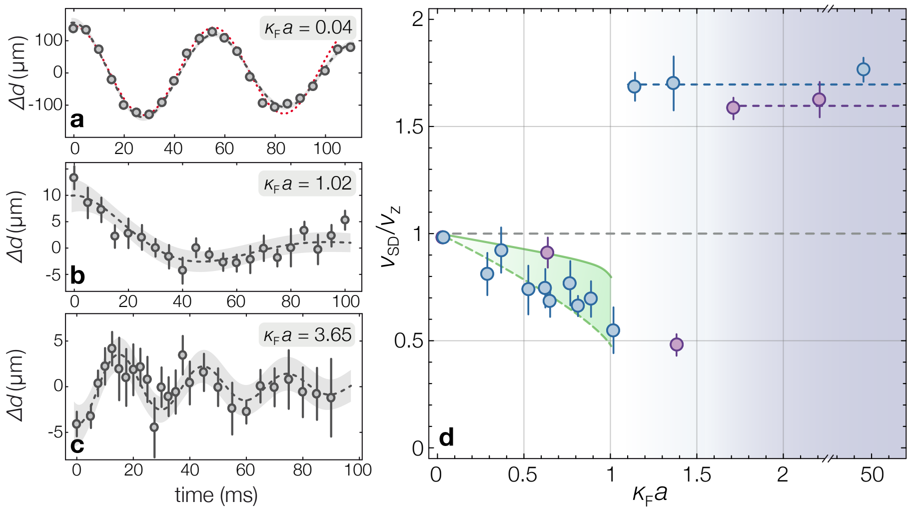

Figure 6.6 – a-c) Signal after removing the overall drift fot a Fermi gas at $T = 0.12(2)\,T_F$ and different interaction strenght. d) Evolution of the spin-dipole mode frequency as a function of $\kappa_F a$ for a Fermi gas at $T = 0.12(2)\,T_F$ (blue) and at $T = 0.25(4)\,T_F$ (purple).

Once the Feshbach field as reached the target value, the barrier is still as high as 10 E_F. For such a high peak value of the barrier, also the gaussian tails of the profile significantly affect the density distribution of the cloud, repelling more and more the atoms from the barrier center. With a barrier height $V_0 = 10E_F$, we measure an interface separation of the two domains of 5 μm. At this point, we turn off in few μs the barrier, a timescale instantaneous respect to the typical ones of the trap. We follow the evolution of the centers of mass z_i, with i being the spin-label, by spin-selective resonant absorption imaging.
The two clouds start to drift one towards the other, with their relative distance $d(t) = z_\uparrow - z_\downarrow$ approaching zero at long evolution time, as shown in fig.6.5. The timescale over which this diffusion happens will be the subject of another section, following below in this chapter. Here instead, we address the oscillatory signal that is detectable at short evolution times in the relative dynamics among the two centers of mass (see fig.6.5). The small-amplitude out-of-phase oscillation on top of $d(t)$ signals the excitation of the spin-dipole mode. For determining its frequency $\nu_{SD} = \omega_{SD}/2\pi$, we first fit the trend of $d(t)$ with an exponential decay, and then we subtract this to the data, obtaining the small-amplitude oscillation $\Delta d(t)$ on top of the overall drift. By fitting the remaining data with a damped sinusoidal oscillation, we evaluate the frequency ν_{SD}. Typical results for this procedure are reported in fig.6.6a-c. The evolution of ν_{SD} respect to the bare trap frequency ν_z is displayed in fig.6.6d, for two distinct temperature data sets, as a function of the interaction strength, parametrized by the usual dimensionless parameter $\kappa_F a$. First, we focus on the results of our coldest data set, that is a Fermi gas at a $T/T_F = 0.12(2)$. As shown in blue symbols in fig.6.6d, the value of ν_{SD} almost equals the bare trap frequency ν_z in the weakly-interacting regime ($\kappa_F a \to 0^+$ and fig.6.6a). As interactions are increased, the

spin-dipole frequency goes down to values as low as $\nu_{SD} \simeq 0.6\nu_z$ at $\kappa_F \simeq 1$ (see fig.6.6b). This decrease of ν_{SD} is accompanied by an increase of the damping of the oscillation in $\Delta d(t)$ [146]. By a further small increase of the interactions above $\kappa_F a \simeq 1$, we observe a sudden jump of the spin dipole frequency which remains essentially constant from $\kappa_F a \geq 1.1$ up to the center of the Feshbach resonance, with a mean value $\nu_{SD} = 1.70(4)\nu_z$. This is in very good agreement with theory models based on the hydrodynamics of two spin clouds bouncing off each other [147] and previous measurements [148]. Similarly, the damping of this oscillation does not significantly depend on interactions for $\kappa_F a \geq 1.1$. We connect the decrease of ν_{SD} with the parallel increase of the spin susceptibility χ. In fact, our experimental observations are in very good agreement with a recent sum-rule approach and knowledge of $\chi(\kappa_F a)$ from QMC calculations [145] for the trend of ν_{SD} versus $\kappa_F a$, evaluated at zero temperature for a repulsive Fermi liquid. The theoretical predictions are plotted in fig.6.6d as a dashed line for an initial overlap of 100% and as a solid line for an initial overlap of 25%, in closer analogy to the experimental configuration where the two clouds just partially mix at the trap center. The frequency of the 25% overlap prediction is higher since only an inner unpolarised layer will contribute to the frequency renormalization, the outer of the cloud being just a spin-polarized Fermi gas. However, the critical point where the abrupt change in ν_{SD} is observed does not depend on the initial configuration and the theoretical lines mark so a confidence range where all of our experimental data fall in. The sudden change in ν_{SD} marks the occurrence of a critical phenomenon and highlights the position of the critical value of $\kappa_F a$ where the ferromagnetic instability occurs.

It should be stressed that the experimental measurement of the spin-dipole mode starting from a mixed phase, as assumed for the theoretical results at 100% overlap, would be unfeasible, with pairing processes kicking in and preventing us to access the upper branch physics [149].

For higher temperatures, the spin-dipole frequency always shows the trend discussed above, but the critical point is shifted at higher $\kappa_F a$, consistently with the general expectations for higher T/T_F [21]. This is always shown in fig.6.6d in purple symbols for a $T = 0.25(4)T_F$ Fermi gas.

The importance of this measurement is that the softening of the spin-dipole mode tells us that the system in the paramagnetic phase is becoming unstable and “would like” to turn polarized. Our results strongly suggest that a para-to-ferro magnetic transition is actually feasible.

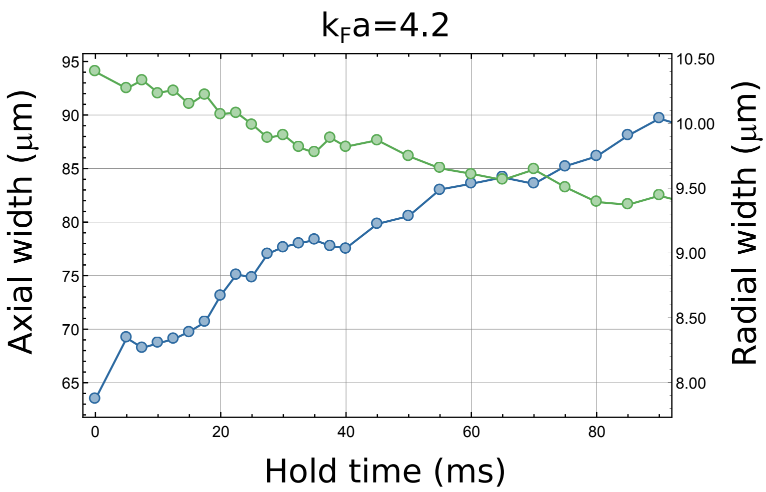

Figure 6.7 – Evolution of the axial and radial widths of the single-spin cloud during the spin-dipole measurement. On the left axis we report the evolution of the axial width (blue symbols) and on the right axis the axial width (green symbols).

Radial modes: collisionless to hydrodynamic transition

During the measurement of the spin-dipole mode, we follow the evolution of the radial and axial widths of each spin-polarized gas. Starting from half the overall trap potential, the clouds tend to fill the entire longitudinal axis, following the decay of the initial spatial separation shown in fig.6.5. This brings the axial width to increase in time, filling the whole longitudinal extension of the trap, while at the same time the radial width diminishes. An example of both of the widths dynamics for a $T = 0.12(2)T_F$ Fermi gas is shown in fig.6.7.

Out of the data in fig.6.7, we subtract an exponential trend and look for eventual modulations on top of that, similarly to the determination of ν_{SD} out of $\Delta d(t)$. Results for this procedure are reported in fig.6.8a, where we investigated the evolution of both the frequency and the damping of these oscillations on top of the overall trend.

The frequency ν_B of the investigated breathing mode shows a transition for increasing interactions from a collisionless to a hydrodynamic regime. At low interactions the breathing mode has a frequency around $2\nu_z$, consistent with the expectations for collisionless dynamics. While interactions are increased, the ratio ν_B/ν_z approaches the value of $\sqrt{12/5}$ predicted by the hydrodynamic regime. The transition already occurs for $\kappa_F a \leq 0.2$, far below the observed critical trend of the spin-dipole mode in fig.6.6. Parallel to this, the decay time of this oscillation, that is the inverse of the damping rate, shows a minimum in the same interaction range. Following the analysis in ref.[150], our system shows a collisionless to hydrodynamic transition around $\kappa_F a \simeq 0.2$.

The importance of this observation is twofold. First, the softening of the spin-dipole mode happens around $\kappa_F a \simeq 1$, well above the transition to the hydrodynamics regime. This

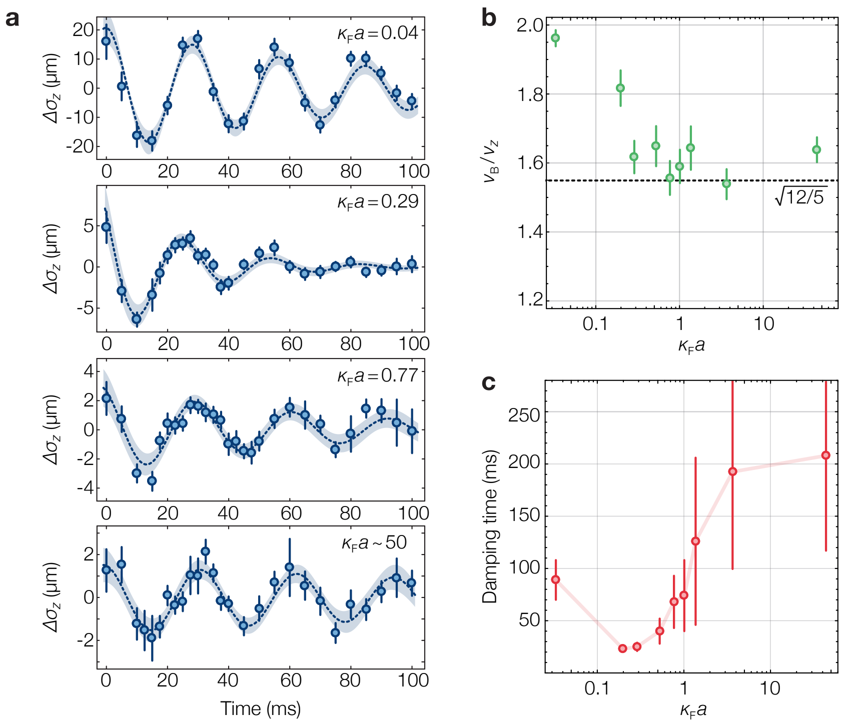

Figure 6.8 – a) Evolution of the axial width modulation for increasing $\kappa_F a$ (top to bottom). b) Frequency of the breathing modes in units of the bare axial trap frequency ν_z. c) Evolution of the damping of the breathing mode as a function of $\kappa_F a$.

means that our sudden change in the spin-dipole mode frequency is not coupled to the breathing dynamics, since the transition for this already happened when considering the relevant regime for the ferromagnetic instability. Second, the diffusion of one cloud into the other, as shown in fig.6.5, happens in a much longer timescale respect to the characteristic trapping periods. This means that the overlap of the two clouds is not 100% during the investigated time regime reported in fig.6.8, as well as for the results in fig.6.6. Despite this reduced overlap, the effect of interaction is sufficient to drive the transition from a collisionless to a hydrodynamic regime. Moreover, as it will be further discussed below, the stronger the interactions the longer the cloud diffusion, meaning an always smaller overlap region for larger $\kappa_F a$. However, the interface region seems to dominate the overall behavior of the spin-polarized cloud. This may explain as well our results for the spin-dipole softening and their good agreement with the theoretical expectations for a 100% overlap configuration.

6.3 Equilibrium spin dynamics

The previous experiments on the spin-dipole directly connected us with the determination of a relevant thermodynamical quantity, the spin susceptibility, whose critical behavior

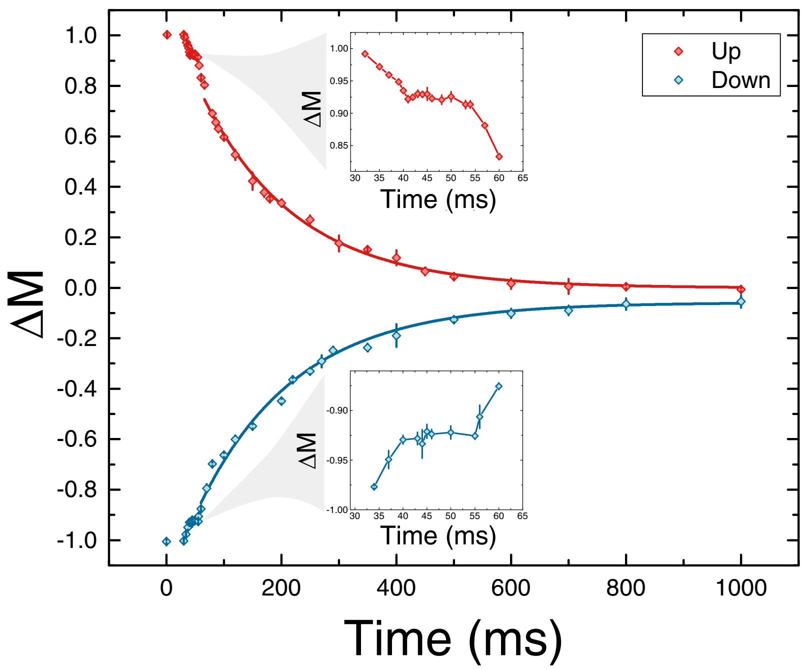

Figure 6.9 – Full time evolution of ΔM at $\kappa_F a = \infty$ at $T = 0.12(2)\,T_F$.

drives the occurrence of the ferromagnetic instability. Here, we instead investigate spin dynamics without exciting the spin-dipole mode, that is in a situation closer to equilibrium transport for accessing the measurement of spin diffusion and transport. Ideally, if the ferromagnetic phase were indefinitely stable, an adiabatic removal of the barrier would trigger just a small re-adjustment of the population in the trap center, maintaining a net magnetization in most of the trap volume.

Apart from the connection with itinerant ferromagnetism, the problem of spin transport is relevant as well for other research lines in physics, from more applied ones such as the creation of spintronics devices and their application in solid-state physics till more fundamental ones, towards a major understanding of the role of impurities in media and the search for phenomena beyond Landau's Fermi liquid picture [151].

We start this measurement preparing the system in the usual domain-wall configuration of fig.6.1b, with two spin domains separated by an impenetrable barrier and with the Feshbach field adjusted at the target value. Initially, the barrier is as high as 10 E_F, the spin interfaces as large as 5 μm. Despite the domain distance being that thin, by quenching the barrier we could trigger the small oscillations of the spin-dipole. For avoiding this, we now ramp down the barrier in a two steps process, as shown in fig.6.3. During the first step, the barrier is linearly ramped down from 10 E_F to 2 E_F in 30 ms, a timescale essentially adiabatic respect to the longitudinal trapping period. Due to the decrease of the barrier potential, the two clouds get closer to each other, with the interface distance reducing from 5 to 1 μm, a distance very similar to the expected size of an eventual

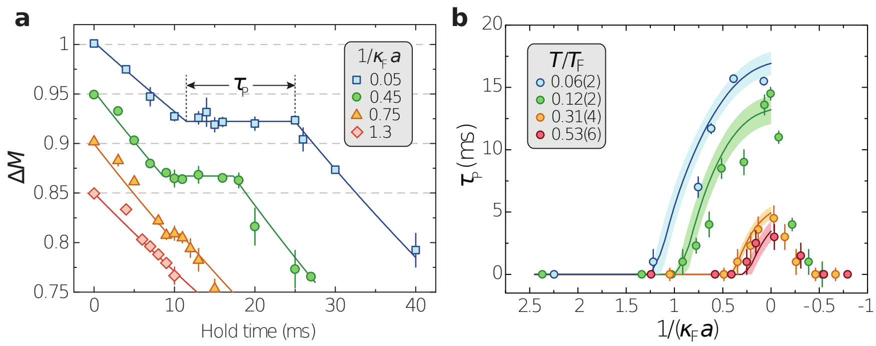

Figure 6.10 – a) Time evolution of ΔM for different $\kappa_F a$ at $T = 0.12(2)T_F$. b) Plateau duration τ_P for different interactions and temperatures

domain wall in a ferromagnetic state [152]. Moreover, during this first ramp down, atoms have not started yet to tunnel. We quantify this introducing the magnetization observable $\Delta M = (M_\uparrow - M_\downarrow)/2$ with $M_i = (N_{i,L} - N_{i,R})/N_i$, with the labels L and R referring to the left and right reservoir, respectively. Meanwhile the barrier is brought from 10 to 2 E_F, the value of ΔM is stuck to one, with the two domains that have not started yet to probe each other. After this, a second linear ramp turns off the barrier potential. The measurements presented in the following have been obtained with a 5 ms linear ramp, a fast timescale respect to the axial trapping period. As shown in fig.6.9, we can so discriminate among two different dynamical regimes, one at short times after the barrier removal, focusing on the eventual metastability of the upper branch and its properties, and one at longer timescales, similarly to what investigated in ref.[148] and connected to the relaxation from the upper branch.

6.3.1 Short time dynamics: exploring the upper branch

Here, we follow the evolution of ΔM, exploring different interaction and temperature regimes, focusing on the short time dynamics, that is just after removing the barrier. Due to the metastability of the upper branch, the physics related to it should be accessible only at the beginning of the dynamics, the longer time frame being dominated by the already occurred relaxation to the lower branch.

In fig.6.10a the time evolution of ΔM is shown for a $T = 0.12(2)T_F$ Fermi gas for different $1/\kappa_F a$. At zero time the barrier is as high as $V_0 = 2E_F$ and in the following 5 ms is turned off as described above. During this time, ΔM diminishes from its initial value of 1. This corresponds to the two cloud filling in the barrier region. However, after an initial mixing, we observe that the spin conductance may actually stop if interactions are sufficiently strong. The plateau of the signal in ΔM corresponds to the condition of zeroed spin current, which can be defined as $I_\sigma = d\Delta M/dt$. The stop of spin diffusivity would correspond to the ideal situation of two ferromagnets that repel each and do not interpenetrate one into the other. However, this spin conductance plateau happens in a limited time window, marked as τ_P. After this finite time τ_P, ΔM decays, similarly to ref.[148].

For measuring τ_p, we fit the ΔM curve with a piecewise function of the kind:

$$\begin{aligned} f(t,\tau_1,\tau_2,x_1,x_2,A) = & A\exp(-x/\tau_1)\cdot\min(x-x_1,0)/(x-x_1)\cdot\max(x,0)/x+ \\ & +A\exp(-x_1/\tau_1)\cdot\min(x-x_2,0)/(x-x_2)\cdot\max(x-x_1,0)/(x-x_1)+ \\ & +A\exp(-x_1/\tau_1)\exp(-(x-x_2)/\tau_2)\cdot\max(x-x_2,0)/(x-x_2) \end{aligned} \tag{6.5}$$

which takes into account the initial mixing, the intermediate stage of conductance stop and the final decay.

Following eq.(6.5), the duration of the plateau is given by $\tau_P = x_2 - x_1$. When no plateau is present, the term x_1 exceeds the time range of the data, loosing physical meaningfulness. We so mark a zero in τ_P when this happens. The investigation of the τ_P duration, as a function of interactions, parametrized by $1/\kappa_F a$, is reported in fig.6.10b, for Fermi gases at different T/T_F.

As it can be seen, for any temperature reported plateaus show up only above a certain interaction strength. Below this critical point, we do not observe any halt of spin diffusion. For stronger interactions on the BEC side of resonance, the plateau lasts for longer time, reaching is maximum around $1/\kappa_F a = 0$. At the same time the duration of τ_P is enhanced for colder samples and in addition, we do not observe any plateau in the spin diffusion for $T/T_F \geq 0.70$. Moving towards the BCS side, the duration of these plateaus abruptly decreases in a narrower region respect to the BEC side.

We understand this zeroing of spin conductance as an evidence of the presence of a domain wall, which sharply separates the regions with unequal spin. Above a critical interaction, the cost of adding a $\downarrow$ particle in a $\uparrow$ Fermi sea is too high and the clouds prefer to stay in a phase-separated state. Adding a $\downarrow$ in a $\uparrow$ Fermi sea would result in the creation of repulsive polaron [95], the quasiparticle associated with the upper branch of the many-body problem, whose tunneling through the phase boundary may become energetically unfavorable.

However, being the upper branch an excited state, the repulsive polaron would decay in the low-lying energy levels, that is the attractive polaron or the molecule-hole continuum, which, as the name suggests, are related to attractive interactions. The relaxation to the lower branch justifies the limited window of the ΔM plateau, with the consequent mixing of the two clouds and the diffusion of quasiparticles from both the branches that will wash out the initial polarization. For better understanding this and capture the experimental results, we developed a phenomenological model for describing the finite time window where spin conductance is stopped, which is explained as it follows:

- If a domain wall exists, a $\downarrow$ fermion would need to pay an energy $\sigma > 0$ to access the other spin domain and form a repulsive polaron at E_+.
- We assume $\sigma = E_+ - E_{+c}$ where E_{+c} is the energy of a free fermion at the interface. This is kept in our case as a phenomenological parameter, but for a homegeneous system at zero temperature we would have $E_{+c} = E_F$.
- The energy of the interface is obtained as $N_{\text{int}}\sigma$, where N_{int} is the number of atoms at the interface of the two spin domains ($z = 0$), evaluated in a shell of thickness equal to one interparticle spacing.
- From the upper branch, repulsive polarons relax into the lower branch at a rate Γ. For any of these processes, an amount of energy $\Delta E = E_+ - E_- - \sigma$ is released into the system at a rate Γ. E_- is the energy of the attractive polaron.
- The value of E_+,E_- and Γ are derived from non-perturbative theoretical results in [94]
- When an amount equal to the tension of the domain wall is released into the system the domain wall melts down. This is given by the condition:

$$N_{\text{int}}\sigma = (E_+ - E_- - \sigma)\Gamma\tau_P \tag{6.6}$$

- Consequently, after eq.(6.6), we have for τ_p:

$$\tau_P = \frac{N_{\text{int}}(E_+ - E_{+c})}{\Gamma(E_{+c} - E_-)}\frac{\hbar}{\epsilon_F} \tag{6.7}$$

In a homogeneous system and in the impurity limit (i.e. $N_\downarrow \ll N_\uparrow$), $E_{+c} = E_F$ is expected for the realization of a fully-saturated ferromagnet. However, we leave E_{+c} as free fitting parameter in eq.(6.7) for the data in fig.6.10b. As it can be seen, our model for the decay of the repulsive polaron and the consequent melting of the domain wall seems to correctly capture the trend of the plateau duration on the BEC side, for the different interaction and temperature regimes. On the BCS side, the model complete fails to reproduce the results. While the measured τ_P decreases to zero already for $1/\kappa_F a \simeq -0.5$, the theoretical model predicts a monotonous increase for τ_P from the resonance to the BCS side. This is mainly due to the increase of Γ predicted by the theoretical approach in ref.[94]. This difference is ascribed to the properties of our initial state, the synthetic ferromagnet. We start the measurement with two disconnected fermionic system, each one occupying all the levels up to the Fermi energy. The energy of the repulsive polaron instead increases monotonically, approaching $2\epsilon_F$ away from resonance on the BCS side. This means that the upper branch on the BCS side is too high for our system to occupy it. When the dynamics is started, our

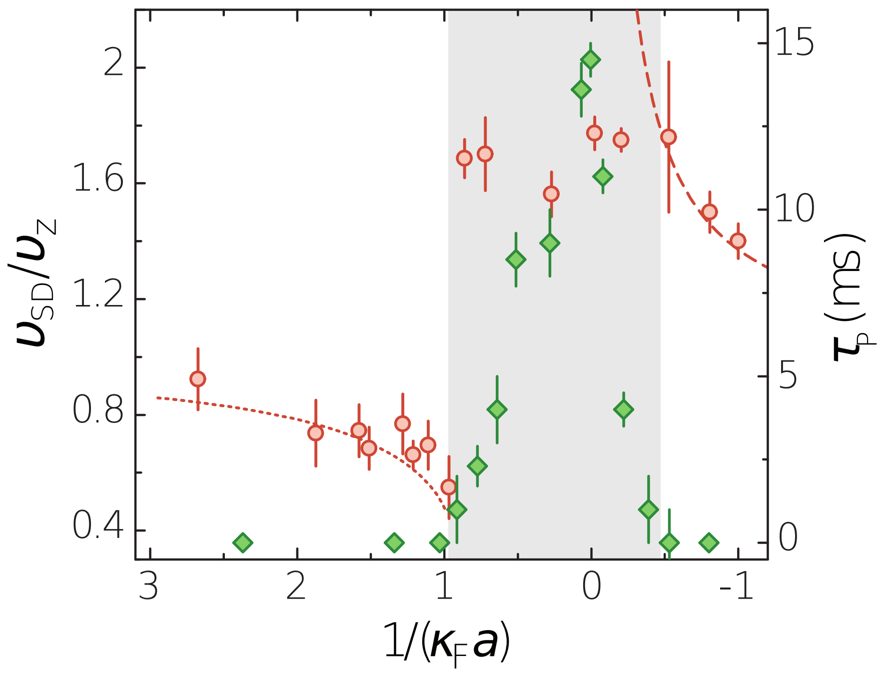

Figure 6.11 – Evolution of the spin-dipole mode frequency (red symbols) versus the occurrence of the ΔM plateau (red symbols) for a Fermi gas at $T = 0.12(2)\,T_F$. Theory for the spin-dipole mode from [145] (dotted red line) and first order prediction for the BCS side (dashed red line). The gray shaded area marks the limit of the ferromagnetic phase.

two non-interacting Fermi gases are projected onto the many-body landscape. Due to the energy distribution of the upper branch, we argue that on the BEC side the system actually occupies this excited level, while becoming energetically not allowed on the BCS side. The upper branch is populated only slightly in a narrow region on the BCS side, realizing so a counter intuitive situation of a repulsive gas with $a < 0$. In a one dimensional system, the occupation of the upper branch for negative scattering length would realize the so-called super Tonks phase, as experimentally observed in [153]. Given the previous energetic arguments, our system populates from the start the lower-branch in the deep BCS regime. These considerations are further supported by the comparison among the spin-dipole frequency trend and that of the plateau, plotted in fig.6.11 for a Fermi gas at $T = 0.12(2)T_F$. First and most important, the softening of the spin-dipole mode is coincident with the appearance of the plateau in ΔM. While the paramagnetic phase is favored, ν_{SD} decreases and no plateau is observed. Once ν_{SD} jumps above the critical point, we observe a $\tau_P > 0$. The existence of the plateau marks the occurrence of the ferromagnetic state, even if in a metastable sense. Even on the BCS side, in the narrow region where $\nu_{SD} \simeq 1.7\,\nu_z$, we found a finite τ_P. In the deep BCS limit, we observe a reduction of the spin-dipole frequency. This trend is expected, since for attractive interactions the spin susceptibility is expected to be lower than that of an ideal Fermi gas, meaning an higher ν_{SD}. For $\kappa_F a \to 0^-$, $\chi \to \chi_0$ and so the spin-dipole frequency should approach the bare trap one. We find very good agreement among our data and that obtained by a first-order theoretical approach. However, this perturbative treatment should not be very reliable in the strongly-interacting limit and we should consider it only as a guide to the eye. The lowering on the BCS side of the spin-dipole frequency is another hint towards the occupation of the lower-branch from the very beginning, since the feature of a normal Fermi liquid with attractive interactions are found. For the BEC side of the resonance, we argue that the observation of a plateau is indeed an effect of the genuine repulsive interactions, associated to the energy cost of repulsive polaron to cross a phase boundary.

6.3.2 Phase diagram of the metastable ferromagnetic state

The measurement of the spin-dipole mode softening is considered the true smoking gun about the instability of the Fermi liquid, occurring at a critical value of the interaction. In fig.6.11, we show the softening to be locked to the observation of the conductance plateau in the spin dynamics investigation. This last measurement requires considerably less experimental effort respect to the spin-dipole one, but equivalently shows the instability of the Fermi liquid.

After this, we have investigated the emergence of the conductance plateau for different interactions and temperature regime. In the temperature-interaction plane, we pinpoint the critical points where the plateau conductance starts to occur, that is $\tau_P > 0$. This results in the determination of the critical line that separates the para from the ferro magnetic state. Results are reported in fig.6.12. For the data at $T = 0.12(2)T_F$ and $T = 0.25(5)T_F$, the onset of the finite plateau is coincident with the critical behavior of the spin-dipole frequency.

Within the framework of Landau's Fermi liquid theory, the spin susceptibility at finite temperature can be written as:

$$\chi^{-1}(T) = \frac{2\pi^2}{m^* k_f}(1 + F_0^a + \pi^2/12(T/T_F)^2) \tag{6.8}$$

The additional quadratic term in the temperature respect to zero temperature case is a signature of Fermi liquid theory. For $T \ll T_F$, the correction is due only to free quasiparticles which is proportional to the density n and therefore to T^2, similarly to the Sommerfeld expansion. After this, the critical line on the temperature-interaction plane for a Fermi liquid is expected to follow the trend:

$$\left(\frac{T}{T_F}\right) \simeq \sqrt{\kappa_F a - (\kappa_F a)_c} \tag{6.9}$$

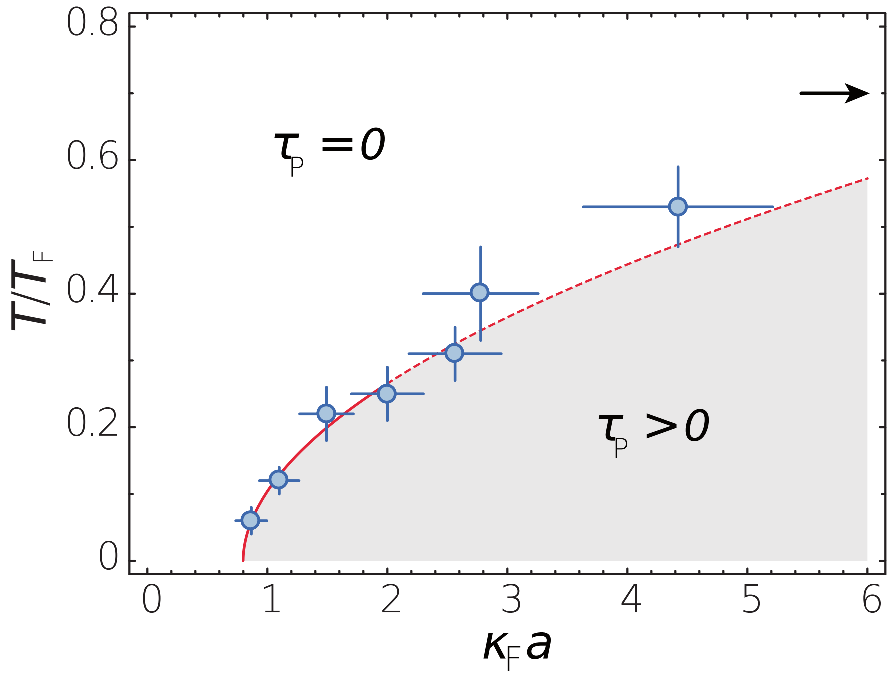

Figure 6.12 – Phase diagram on the temperature-interaction plane of the metastable ferromagnetic state. The solid line is a low temperature fit ($T < 0.3T_F$) with a power law function, which gives a critical exponent $\alpha = 0.52(5)$ and a zero temperature critical interaction $(\kappa_F a)_c = 0.80(9)$. The dashed line is a continuation of this fit, assuming no plateau for $T > 0.7T_F$ (right arrow).

where the term $(\kappa_F a)_c$ indicates the critical interaction at zero temperature, which in the original Stoner model is $(\kappa_F a)_c = \pi/2$.
The low temperature data ($T < 0.3T_F$) have been fitted with a power law function of the kind:

$$y = A \cdot (x - x_0)^\alpha \tag{6.10}$$

with y for the temperature and x for the interaction term.
We obtain a value for the zero-temperature critical interaction $(\kappa_F a)_c = 0.80(9)$, in good agreement with recent QMC calculations, which place this critical parameter in the range $0.8 \leq (\kappa_F a)_c \leq 0.9$ [29, 89]. For the critical exponent we instead obtain $\alpha = 0.52(5)$, in good agreement with the expectations for the Fermi liquid theory of $\alpha = 1/2$.
The line in the high T- high $\kappa_F a$ region of fig.6.12 is extedend for including the absence of plateau at $T \geq 0.7T_F$. We use an exponential curve which smoothly connects with the fitted line of eq.(6.10) and asymptotically approaches the $T = 0.7T_F$ line.
Our results could be a benchmark validation for those theoretical approaches that seek the boundaries of the ferromagnetic instability. However, it should be stressed that we do not realize the proper phase of the itinerant ferromagnetism, since the eventual ferromagnetic state is washed out by detrimental processes at the interface of the two spin domains.

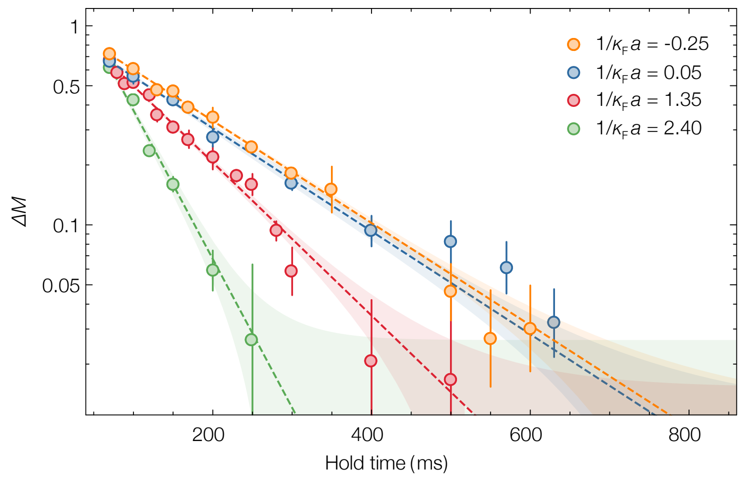

Figure 6.13 – Evolution of $\Delta M(t)$ for different interactions at a T/T_F=0.12(2).

Rather, our results show that the regime of ferromagnetic instability is achievable as well for ultracold atomic Fermi gases and should be regarded as a starting point for the stabilization of the ferromagnetic phase. As instance, this could be achieved by exploiting the kinetic energy quench given by optical lattices or disorder [154, 155], which are expected to lower the critical interaction to a regime where the upper branch is sufficiently stable, or by using proper mass-imbalanced fermionic mixtures where the decay from the upper branch is naturally suppressed [118].

6.3.3 Long time dynamics: spin drag in the lower branch

The evolution at longer times, that means after the plateau transient as disappeared, is instead connected to the scattering properties of the quasiparticles that may populate the different branches. Their diffusion through the medium washes out the initial spin polarization, bringing the system to a vanishing final magnetization. The characterization of the timescale and how this diffusion happens may connect us to the microscopic scattering properties of these quasiparticles.

Following the previous arguments, naively one would expect that on the BCS side the diffusion is dominated by attractive polarons, since the upper branch is forbidden for energetic arguments. On the BEC regime instead, one expects the diffusion to be connected to that of repulsive polarons, since these quasiparticles are well defined away from the resonance, that is have a high residue Z and a long lifetime, whit the lower branch too low in energy for being populated. In the strongly interacting regime, quasiparticles on both branches will contribute to the overall diffusion, with a continuous relaxation from the excite level to the ground one.

The scattering properties of these quasiparticles in a medium can be investigated developing a diffusion equation for the relative dynamics of the center of mass of the two spin clouds $d(t) = z_\uparrow - z_\downarrow$ or equivalently for $\Delta M(t)$. This can be modeled starting from the Boltzmann equation [156], obtaining two coupled equations as:

$$\partial_t(z_\uparrow - z_\downarrow) - (v_\uparrow - v_\downarrow) = 0 \tag{6.11}$$

$$\partial_t(v_\uparrow - v_\downarrow) + \omega_z^2(z_\uparrow - z_\downarrow) = (\partial_t(v_\uparrow - v_\downarrow))_{\text{coll}} \tag{6.12}$$

where v_i is the average velocity of the i-spin component cloud and $(\partial_t(v_\uparrow - v_\downarrow))_{\text{coll}}$ the collisional term. Following [156], the collisional term can be written as:

$$(\partial_t(v_\uparrow - v_\downarrow))_{\text{coll}} = -\Gamma_S(v_\uparrow - v_\downarrow) \tag{6.13}$$

where Γ_S is the spin drag coefficient.
Given this, the equation of motion can be written as:

$$\ddot{d} + \Gamma_S \dot{d} + \omega_z^2 d = 0 \tag{6.14}$$

The evolution of $d(t)$ and ΔM follows that of a damped oscillator, with a damping rate related to the spin drag coefficient Γ_S, which encodes the diffusion of a quasiparticle in the medium.
By fitting our experimental decaying curves, as those in fig.6.13, with the solution of eq.(6.14), we investigate the evolution of the spin drag in units of $\epsilon_F/\hbar$ as a function of temperature and interactions. Data are reported in fig.6.14 and are compared with a theoretical model for an impurity moving in a homogeneous Fermi gas based on kinetic theory and T-matrix approximation for evaluating the scattering cross section of the impurity itself with the medium. Our results are in very good agreement with the theoretical model, in particular in the high temperature regime ($T \geq 0.3T_F$ in fig.6.14b, since the T-matrix approximation is known to be less accurate at low temperatures. Our data also capture the asymmetry of the spin drag coefficient across the Unitary limit, with the maximum being shifted at $a > 0$, similarly to other recently experimentally determined transport coefficients such as the shear viscosity [157] and the transverse demagnetization [158, 159]. This asymmetry is progressively washed out for increasing T/T_F, in agreement with the expectations for a non-degenerate Fermi gas or Boltzmann gas, where the drag is expected to be a^2 dependent [148, 160, 161].

6.4 Pairing instability and molecule formation

As extensively anticipated, one major issue that hindered the investigation of Fermi gases with strong repulsion is represented by the pairing instability [10, 11, 144]. Repulsive interactions can be achieved only when sitting on the upper branch of the system, which in

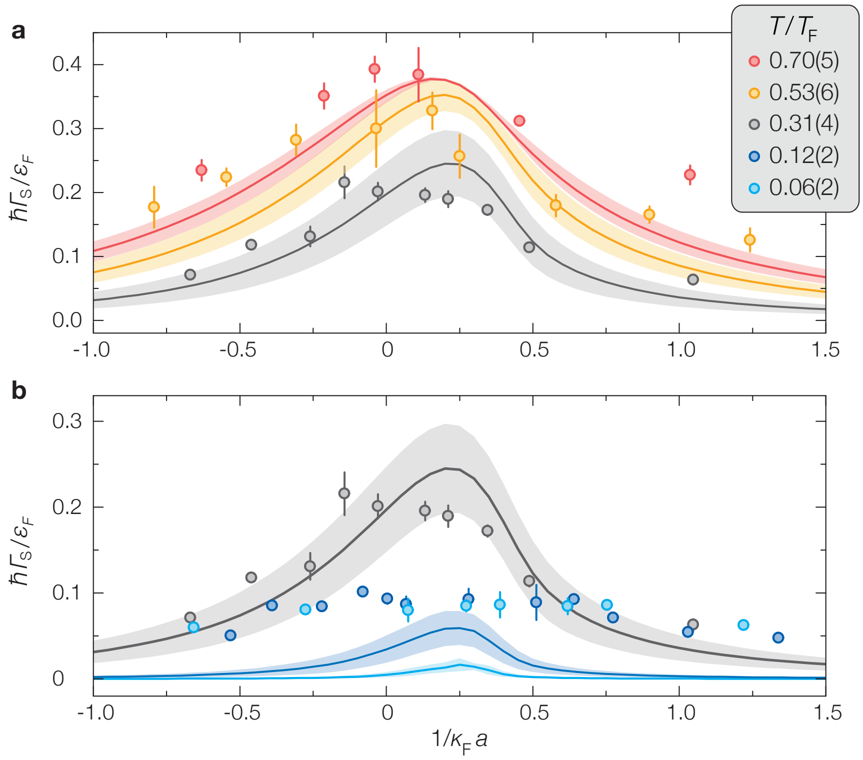

Figure 6.14 – Evolution of the spin drag coefficient Γ_S in units of $\epsilon_F \hbar$ for different temperatures across the Feshbach resonance. a) Higher temperatures. b) Lower temperatures.

turn is intrinsically metastable, being an excited state of the low lying BEC-BCS crossover superfluid state. The paired phase represents the true ground state of the many-body system, thus the upper branch will inevitably show a tendency to relax into it via decay processes, both of two and three-body character.

Our initial domain-wall configuration has to interpreted as the only one to overcome the pairing instability, which in a paramagnetic homonuclear mixture close to a broad Feshbach resonance is the dominating mechanism [21, 96, 144]. With this, we are able to contain the system tendency towards pairing, allowing for the investigation of the metastable upper branch. Furthermore, since our phenomenological model seems to capture the observed plateau, attractive polarons, rather than pairs, seem to be the preferential decay products in our system, at least in the strongly interacting regime. Nonetheless, we should rule out that the observed features, both in the mode softening and the spin transport measurements, are ascribable to pairing effects.

Typically [11], the counting of molecules is achieved via a rapid magnetic field ramp technique. After some evolution time at a target field close to the Feshbach resonance center, where molecules could be formed via recombination processes, two distinct measurements are performed. In the first, performed close to the Feshbach resonance center,

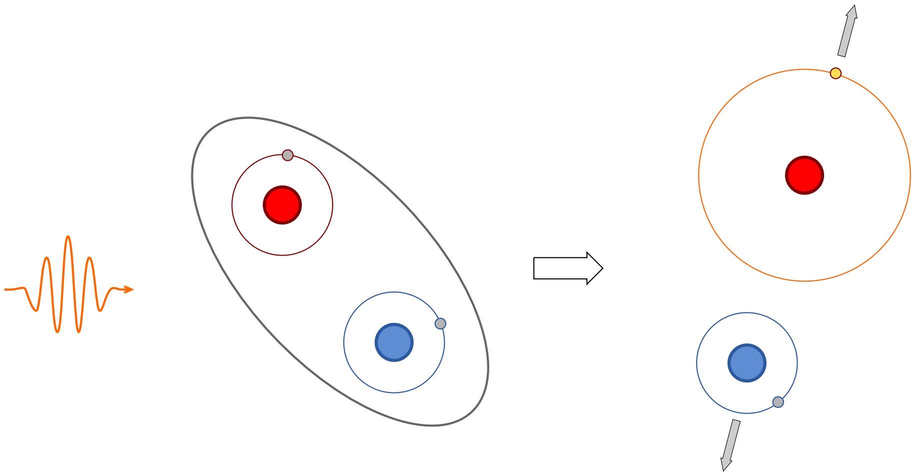

Figure 6.15 – Sketch of the technique employed for the determination of the molecular fraction. The incident photon may be absorbed by one spin component of the pair, resulting in the dissociation of this last and with the two bare atoms acquiring a considerable momentum

the population of both atoms and molecules can be monitored by the same absorption imaging technique, since the molecular binding energy is here much smaller than the linewidth of the imaging transition, preventing them to be distinguished from bare atoms. In the second instead, the imaging pulse is taken after a rapid sweep of the magnetic field to zero. In this way, the weakly bound pairs created at the Feshbach center are converted into deeply bound molecules, which become transparent to the imaging light. From the differential analysis among the two images, the molecules population can be recovered. Unfortunately, our setup does not allow to perform fast ($\sim 10^2$ G/μs) ramps to low fields, hence we employed a different protocol to monitor the presence of molecules in the system. This is based on acquiring, within a single experimental run, two subsequent absorption images, by means of 4 μs long pulses resonant with the $\uparrow$ and $\downarrow$ states, respectively, and separated by 300 μs. If no molecules are present, the effect of the first imaging pulse resonant with the $\uparrow$ state on $\downarrow$ atoms is negligible, the $\uparrow$ imaging light being off-resonant to the $\downarrow$ component. Furthermore, the short delay between the two pulses greatly limits the effect of heating of the $\downarrow$ cloud associated to collisions with escaping $\uparrow$ imaged atoms.

The effect of the first imaging pulse is in turn completely different if molecules, rather than atoms, are considered. Since the $\uparrow - \downarrow$ dimers are only weakly bound, the first imaging photon, resonant with the $\uparrow$ optical transition, dissociates the bound state into two atomic products, each of which symmetrically acquires a significant momentum. The latter is associated to the density of states of the two outgoing atoms, to the binding energy of the dimer (negligible in this case), and to the photon momentum[119] $\hbar k_L$, as shown in fig.6.15. The increase of the cloud size detected by the second imaging pulse is thus proportional to the amount of molecules in the system. We therefore monitor the increase of the radial width after the first pulse for different interaction strengths and different evolution times during the spin diffusion.

We developed a simple model to link the molecular fraction to the increase of the cloud width after the first pulse, following the experimental protocol described above. In general, the size of a trapped cloud can be written as:

$$\langle x_0^2 \rangle = \frac{2\langle U \rangle}{m\omega^2} \tag{6.15}$$

Where $\langle U \rangle$ is the potential energy of one atom weighted over the density distribution of the cloud, the latter being eventually modified by interaction effects. In the case of a pure gas of dimers, application of an imaging pulse resonant with the $\uparrow$ component causes the dimers to dissociate with a certain transfer of energy E_1 to the $\downarrow$ component. Since the photon energy is always larger than the binding one, we assume E_1 to be independent from the molecular binding, and hence independent from $\kappa_F a$.

According to the same argument of Eq. (6.15), the width measured through the second pulse, following the first, can be written as:

$$\langle x_1^2 \rangle = \frac{2\langle U + E_1 \rangle}{m\omega^2} \tag{6.16}$$

If the gas is a mixture of free atoms and molecules, the mean size is set by:

$$\langle x^2 \rangle = \frac{N_a \langle x_0^2 \rangle + N_m \langle x_1^2 \rangle}{N_a + N_m} \tag{6.17}$$

Defining the molecular fraction $f_m = N_m/N$, we get:

$$\langle x^2 \rangle = \frac{2}{m\omega^2}\langle U \rangle + \frac{2}{m\omega^2}\langle E_1 \rangle f_m = \langle x_0^2 \rangle + \frac{2}{m\omega^2}\langle E_1 \rangle f_m \tag{6.18}$$

When starting from a pure molecular sample, $f_m = 1$, we would have:

$$\frac{2}{m\omega^2}\langle E_1 \rangle = \langle x_{1m}^2 \rangle - \langle x_{0m}^2 \rangle \tag{6.19}$$

We can therefore express the molecular fraction as:

$$f_m = \frac{\langle x_1^2 \rangle - \langle x_0^2 \rangle}{\langle x_{1m}^2 \rangle - \langle x_{0m}^2 \rangle} \tag{6.20}$$

The denominator of Eq. (6.20) can be experimentally determined by applying the double-pulse imaging technique on a BEC-BCS crossover superfluid at a temperature $T/T_F < 0.1$, which ensures a molecular fraction $f_m \simeq 1$ on the BEC side of the resonance. The change of the density distribution when moving from the unitary limit to the BEC one is accounted by renormalizing the measured radial width by the average density of the gas, evaluated with the conventional single-pulse absorption imaging.

The numerator of Eq. (6.20) is evaluated by measuring the radial size of the cloud $\langle x_1^2 \rangle$ at

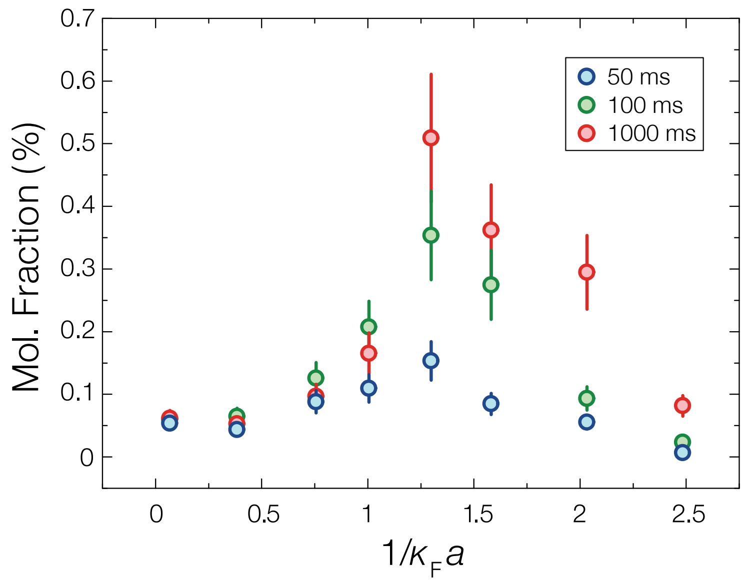

Figure 6.16 – Molecule fraction derived from the double image technique. The peak of molecule formation appears below the measured critical interactions.

different evolution times of the dynamics. Conversely, $\langle x_0^2 \rangle$ is the size measured through the first imaging pulse at the corresponding times. Results of this analysis are reported in Fig. 6.16, for various interaction strengths and different diffusion times, for a repulsive Fermi gas mixture initially prepared at T/T_F=0.12(2).

The general trend for these measurements is interpreted as follows: starting from the weakly repulsive regime, the upper branch is very long-lived, and despite rapid mixing of the two spin clouds only a small number of molecules is formed. Increasing interactions, the decay rate of the upper branch monotonically increases[21, 94–96]: hence, despite a parallel increase of the spin drag coefficient[146, 148], which tends to slow down the interpenetration and to reduce the spatial overlap of the ↑ and ↓ clouds, the molecule formation becomes more sizable, reaching a maximum near $1/(\kappa_F a) \sim 1.3$. However, as one accesses the strongly interacting regime where the magnetic susceptibility is increasing, the molecule formation is again strongly reduced, highlighting the resistance of the system to mix the two spin components. The trend at large $\kappa_F a$ values, observed also after long evolution times even when the spatial overlap of the two clouds has considerably increased, suggests that also at small values of local population imbalance the system may be a Fermi liquid state of attractive polarons, rather than a Bose gas of dimers. The Fermi liquid state might be favored by our way to initialize the system dynamics, and also by the temperature increase associated to the exothermic decay process from the upper to the lower branch.

Importantly, for timescales below 100 ms, over which both the plateau measurements and the spin-dipole oscillations were acquired, the observed heating is relatively small and the derived molecule fraction remains below 10% for interaction strengths exceeding the critical value for the stop of diffusion to occur. We therefore conclude that neither the behaviour of the spin-dipole frequency nor the appearance of plateaus in the spin diffusion can be strongly influenced by dimer formation. For what concerns the measurement of the spin-dipole frequency, the possible development of a sizeable cloud of molecules is expected to strongly reduce the amplitude of the out-of-phase oscillation. While some additional damping associated to pairing effects cannot be excluded in our frequency measurements, we do not envision how the observed dynamics could arise from a lower-branch energy functional, with attractive interactions forming bound pairs[11, 147]. This is equally true if an attractive Fermi liquid, rather than a Bose gas of pairs, would be considered: for this latter system, both experimental studies[11, 162] and theoretical calculations[163] indicate that the spin susceptibility monotonically decreases when moving from the BCS to the BEC side of the crossover, vanishing at $k_F a \simeq 1$. This in turn would correspond to a spin-dipole frequency monotonically increasing when passing from BCS to BEC side along the lower branch, a qualitatively different trend with respect to the one revealed in our experiment.

CHAPTER 7

Conclusions and outlook

Within this thesis we have described the construction of an experimental apparatus for the production of ultracold degenerate samples of atomic ^{6}Li Fermi gases. We have realized a flexible quantum simulator to investigate over the transport and dynamical properties of strongly interacting fermionic systems. We have focused on the exploration of some fundamental aspects of paradigmatic phenomena, namely superfluidity and ferromagnetism, allowing comparison with state-of-the-art theoretical approaches.

We have first probed fermionic superfluidity by investigating the coherent Josephson dynamics in these systems. Importantly, the Josephson effect was used as a probe of the strongly interacting condensate states across the whole BEC-BCS crossover and of their inner order parameter. Further investigation in this regime may allow to determine the fermionic superfluid gap of these fermionic superfluids or to observe other dynamical phases, such as for instance Shapiro resonances [164].

In the second part of this thesis, we have investigated repulsive Fermi gases on the upper branch of a Feshbach resonance. Our observation of the softening of the spin-dipole mode and the investigation of spin currents point out that a para-to-ferromagnetic phase transition is possible, for critical values of interaction and temperature, as first envisioned by Stoner [9] in his minimal model of a homogenous gas of itinerant fermions. Interesting future extension of our studies could allow us to tackle other fundamental issues, such as the order of the occurring phase transition, even in the presence of weak optical lattices or controlled disorder.

The results we have obtained within this work may pave the way for the exploration of similar phenomena in situation where quantum correlations and fluctuations are enhanced, as for instance in two-dimensions (2D) [165, 166].

In the last period of this thesis, an optical scheme which exploits a TEM01 beam has been developed for trapping the atoms in a single two-dimensional layer. This is a physical scenario extremely relevant for strongly-correlated fermionic phenomena such as high-T_C superconductivity. The large optical access of our apparatus will enable an accurate microscopic investigation over the dynamics of the system. Moreover, the tailoring of the trapping potential will allow to explore a regime at the dimensional crossover from three-to-two dimensions, a scenario difficult to target in condensed matter systems and where the increase of the critical temperature of the superfluid state is expected to occur [167], similarly to the phenomenology of cuprate superconductors.

The rich possibility given by optical manipulation will allow to further explore ideal models of condensed matter, from the usual Fermi-Hubbard model with single-particle resolution [168], to more exotic ones, as for instance the trapping in a toroidal configuration in analogy to SQUID devices in solid-state physics. This may be achieved by the implementation of optical elements, such as a Digital Mirror Device (DMD) or a Spatial Light Modulator (SLM), which may allow the creation of microscopically tailored optical potentials when combined with our high-resolution optical systems. Very recently, we have started to implement the DMD device for replacing the rigid optical scheme of the barrier potential with a more versatile one.

An extreme fertile ground for experimental exploration in quantum gases is represented by the realization of synthetic gauge potentials [169] and synthetic spin-orbit coupling [170, 171]. The implementation of these on a strongly interacting ^{6}Li quantum gas may lead to the exotic realization of a topological superfluid. Recently, a theoretical approach showed the possibility of using the Josephson effect [172] for identifying the presence of the elusive Majorana fermion in a topological superfluid system.

Quantum gases experiments are really entering into the regime on the edge of our theoretical knowledge, with the possibility to push its boundary a bit further and to artificially create new states of matter nowadays only in theorists mind [173, 174].

Ringraziamenti

Questa tesi è il riassunto di un intenso lavoro durato quasi quattro anni, frutto di una intensa collobarazione e interazione con molte altre persone, senza le quali non avrei realizzato nessun dei risultati sperimentali qui presentati.
In primis, vorrei ringraziare il prof. Massimo Inguscio e il prof. Rosario Fazio per avermi sostenuto e mostrato fiducia, e per avermi permesso di affrontare questo cammino a cavallo tra due istituti distinti, il LENS di Firenze e la Scuola Normale di Pisa, consentendomi di fare ricerca in un ambiente sempre stimolante.
Un grazie speciale agli altri miei due supervisors, quelli che mi hanno insegnato i trucchi del mestiere, Giacomo Roati e Matteo Zaccanti. Grazie per avermi insegnato tanto ed essere stati degli ottimi amici.
Le intense giornate in laboratorio sono passate più facilmente grazie alla presenza di molte altre persone, che mi hanno aiutato nei momenti di difficoltà, ma soprattutto con cui ho condiviso momenti di gioia quando ci rendevamo conto che la fisica aveva un senso. Un grazie di cuore ad Alessia e Jorge, che hanno iniziato questa avventura con me, e anche ai membri più recenti del laboratorio Andrea, Francesco, Elettra, Chiara ed Andreas.
Un grazie a tutti gli altri membri del gruppo di atomi freddi del LENS e ai numerosi amici che vi ho trovato.
Un abbraccio speciale anche alla mia famiglia che mi è sempre stata vicina anche se da lontano e mi ha sempre sostenuto nelle mie scelte.
Infine, un grazie a Claudia. Per tutto il resto.

APPENDIX A

^{6}Li Level structure

Hyper-fine structure

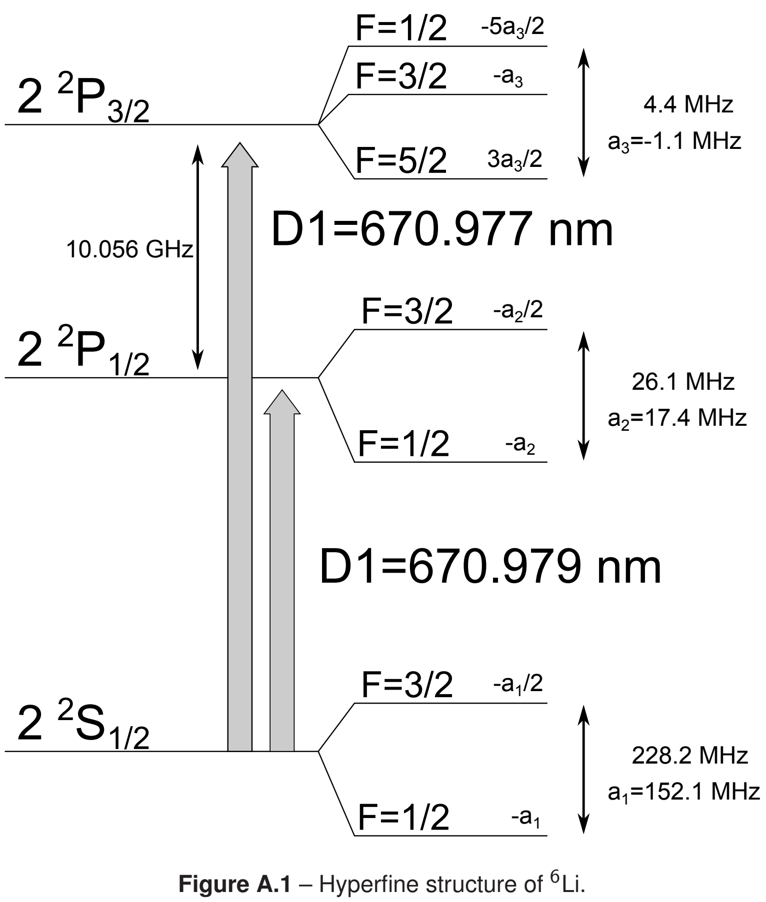

Figure A.1 – Hyperfine structure of ^{6}Li.

The hyper-fine structure of Li6 is sketched in the figure A.1. The ground state is described using conventional spectroscopic notation with momentum quantum numbers $L = 0$ (s-wave orbital), $S = 1/2$ and $I = 1$. The D2 and D1 line are reported and their relative splitting.

High magnetic field behavior

Here we report in fig.A.2 the energy shifts of the hyperfine levels of the ^{6}Li ground state as a function of the applied magnetic field. The usual labeling $|1\rangle, |2\rangle, \ldots$ of the ground-state levels is also shown in fig.A.2.

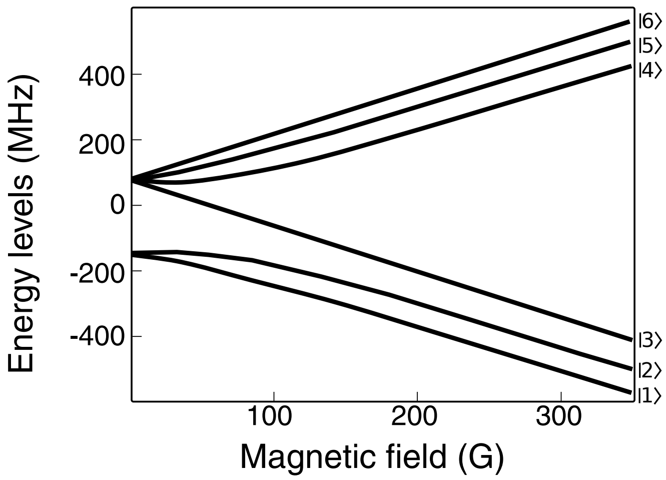

Figure A.2 – Behavior of the $^2S_{1/2}$ level as a function of the magnetic field.

Bibliography

[1] I. Bloch, J. Dalibard, and W. Zwerger. Many-body physics with ultracold atoms. *Rev. Mod. Phys.*, 80:885, 2008. See page: 1

[2] R. P. Feynman. Simulating physics with computers. *Int. Journ. of Theo. Phys.*, 21 (6/7):467, 1982. See page: 1

[3] C. Chin, R. Grimm, P. Julienne, and E. Tiesinga. Feshbach resonances in ultracold gases. *Rev. Mod. Phys.*, 82:1225, 2010. See pages: 1, 10, 12, 68

[4] A. J. Leggett. *in: Modern trends in the theory of condensed matter*. Springer-Verlag, 1980. See pages: 2, 18, 19

[5] M. W. Zwierlein. Superfluidity in ultracold atomic Fermi gases. In K.H Benneman and J.B. Ketterson, editors, *Novel Superfluids*, volume 2. Oxford Science Publications, 2014. See pages: 2, 24

[6] E. Varoquaux. Anderson's considerations on the flow of superfluid helium: Some offshoots. *Rev. Mod. Phys.*, 87:803–854, 2015. See pages: 2, 33, 91

[7] Y. Makhlin, G. Schön, and A. Shnirman. Quantum-state engineering with Josephson-junction devices. *Rev. Mod. Phys.*, 73:357–400, 2001. See page: 2

[8] P.W. Anderson. Special effects in superconductivity. In E. R. Caianello, editor, *Lectures on the Many-body Problems*, pages 113 – 135. Academic Press, 1964. See page: 3

[9] E. C. Stoner. Atomic moments in ferromagnetic metals and alloys with non-ferromagnetic elements. *Philos. Mag.*, 15:1018, 1933. See pages: 3, 33, 101, 127

[10] G. B. Jo et al. Itinerant ferromagnetism in a Fermi gas of ultracold atoms. *Science*, 325(5947):1521–1524, 2009. See pages: 3, 102, 120

[11] C. Sanner et al. Correlations and pair formation in a repulsively interacting Fermi gas. *Phys. Rev. Lett.*, 108:240404, 2012. See pages: 3, 102, 120, 121, 125

[12] M. Knap, A. Shashi, Y. Nishida, A. Imambekov, D. A. Abanin, and E. Demler. Time-dependent impurity in ultracold fermions: Orthogonality catastrophe and beyond. *Phys. Rev. X*, 2:041020, 2012. See page: 4

[13] E. Fermi. Sulla quantizzazione del gas perfetto monoatomico. *Rend. Lincei*, 3: 145–149, 1926. See page: 7

[14] M. Bartenstein et al. Collective excitations of a degenerate gas at the BEC-BCS crossover. *Phys. Rev. Lett.*, 92:203201, 2004. See page: 9

[15] A. Altmeyer et al. Precision measurements of collective oscillations in the BEC-BCS crossover. *Phys. Rev. Lett.*, 98:040401, 2007. See page: 9

[16] W. Ketterle and M. W. Zwierlein. Making, probing and understanding ultracold Fermi gases. In M. Inguscio, W. Ketterle, and C. Salomon, editors, *Proceedings of the International School of Physics "Enrico Fermi"*, volume 31, pages 247–422, 2008. See pages: 9, 10

[17] B. DeMarco and D. S. Jin. Onset of Fermi degeneracy in a trapped atomic gas. *Science*, 285:1703–1706, 1999. See page: 9

[18] B. DeMarco. *Quantum behavior of an atomic Fermi gas*. PhD thesis, UC Boulder, 2001. See page: 9

[19] G. M. Bruun and C. W. Clark. Ideal gases in time-dependent traps. *Phys. Rev. A*, 61: 061601, 2000. See page: 10

[20] L. D. Landau and E. M. Lifshitz. *in: Quantum Mechanics - Non-relativistic theory*. Pergamon Press, 1965. See page: 11

[21] P. Massignan, M. Zaccanti, and G. M. Bruun. Polarons, dressed molecules and itinerant ferromagnetism in ultracold Fermi gas. *Rep. Prog. Phys*, 77:034401, 2014. See pages: 11, 33, 34, 36, 39, 40, 109, 121, 124

[22] K. Burnett et al. Quantum encounters of the cold kind. *Nature*, 416:225, 2002. See page: 12

[23] H. Feshbach. A unified theory of nuclear reactions. ii. *Ann. Phys.*, 19:287–313, 1962. See page: 13

[24] S. Inouye et al. Observation of Feshbach resonances in a Bose-Einstein condensate. *Nature*, 392:151–154, 1998. See page: 14

[25] G. Zürn et al. Precise characterization of ^{6}li feshbach resonances using trap-sideband-resolved rf spectroscopy of weakly bound molecules. *Phys. Rev. Lett.*, 110: 135301, 2013. See pages: 14, 68, 78, 86, 99

[26] D. S. Petrov, C. Salomon, and G. V. Shlyapnikov. Weakly bound dimers of fermionic atoms. *Phys. Rev. Lett.*, 93:090404, 2004. See pages: 16, 20, 23, 68

[27] D. L. Pricoupenko and Y. Castin. One particle in a box: the simplest model for a Fermi gas in the unitary limit. *Phys. Rev. A*, 69:051601(R), 2004. See pages: 16, 17

[28] T. Busch, B. Englert, K. Rzazewski, and M. Wilkens. Two cold atoms in a trap. *Found. Phys.*, 28:549–559, 1998. See page: 16

[29] S. Y. Chang, M. Randeria, and N. Trivedi. Ferromagnetism in the upper branch of the Feshbach resonance and the hard-sphere Fermi gas. *PNAS*, 108:51–54, 2009. See pages: 18, 36, 118

[30] C. Kohstall. *Resonantly interacting Fermi gases: coherence, collective dynamics and polarons*. PhD thesis, University of Innsbruck, 2012. See page: 19

[31] M.H. Anderson et al. Observation of Bose-Einstein condensation in a dilute atomic vapor. *Science*, 269:198, 1995. See page: 20

[32] F. Dalfovo, S. Giorgini, L. Pitaevskii, and S. Stringari. Theory of Bose-Einstein condensation in trapped gases. *Rev. Mod. Phys.*, 71:463, 1999. See page: 20

[33] S. Jochim et al. Bose-Einstein condensation of molecules. *Science*, 302:2101–2103, 2003. See page: 21

[34] M. Greiner, C. A. Regal, and D. S. Jin. Emergence of a molecular Bose-Einstein consensate from a Fermi gas. *Nature*, 426:537–540, 2003.

[35] M. W. Zwierlein et al. Observation of Bose-Einstein Condensation of molecules. *Phys. Rev. Lett.*, 91:250401, 2003. See page: 21

[36] L. N. Cooper. Bound electron pairs in a degenerate Fermi gas. *Phys. Rev.*, 104:1189, 1956. See page: 21

[37] J. Bardeen, L. N. Cooper, and J. R. Schrieffer. Theory of superconductivity. *Phys. Rev.*, 108:1175, 1957. See page: 21

[38] M. Inguscio, W. Ketterle, and C. Salomon. In *Proceedings of the International School of Physics "Enrico Fermi"*, volume 164, 2007. See page: 21

[39] I. Giaever. Energy gap in superconductors measured by electron tunneling. *Phys. Rev. Lett.*, 5:147–148, 1960. See pages: 21, 32, 100

[40] A. Damascelli, Z. Hussain, and Z. X. Shen. Angle-resolved photoemission studies of the cuprate superconductors. *Rev. Mod. Phys.*, 75:473–541, Apr 2003. See page: 21

[41] C. Chin et al. Observation of the pairing gap in a strongly interacting Fermi gas. *Science*, 305:1128–1130, 2004. See page: 21

[42] A. Schirotzek, Y. Shin, C. H. Schunck, and W. Ketterle. Determination of the superfluid gap in atomic Fermi gases by quasiparticle spectroscopy. *Phys. Rev. Lett.*, 101: 140403, 2008. See page: 21

[43] M. Randeria. Ultracold Fermi gases: Pre-pairing for condensation. *Nat. Phys.*, 6: 561–562, 2010. See page: 22

[44] M. Holland, S. J. J. M. F. Kokkelmans, M. L. Chiofalo, and R. Walser. Resonance superfluidity in a quantum degenerate Fermi gas. *Phys. Rev. Lett.*, 87:120406, 2001. See page: 22

[45] G. F. Bertsch. Many-body challenge problem. *Int. J. Mod. Phys.*, 15:3, 2001. See page: 22

[46] Q. Chen, J. Stajic, S. Tan, and K. Levin. BCS-BEC crossover: from high temperature superconductors to fermionic superfluids. *Physics Reports*, 412:1–88, 2005. See page: 22

[47] M. W. Zwierlein. *High-Temperature superfluidity in an ultracold Fermi gas*. PhD thesis, MIT, 2006. See page: 22

[48] C. A. R. S. de Melo, M. Randeria, and J. Engelbrecht. Crossover from BCS to Bose superconductivity: transition temperature and time-dependent Ginzburg-Landau theory. *Phys. Rev. Lett.*, 71:3202–3205, 1993. See page: 22

[49] J. G. Bednorz and K. A. Muller. Possible hightc superconductivity in the Ba-La-CuO system. *Zeit. Phys. B Cond. Matter*, 64(2):189–193, 1986. See page: 22

[50] T. Timusk and B. Statt. The pseudogap in high-temperature superconductors: an experimental survey. *Rep. Prog. Phys.*, 62:61, 2010. See page: 23

[51] H. Ding et al. Spectroscopic evidence for a pseudogap in the normal state of underdoped high-Tc superconductors. *Nature*, 382:51–54, 1996. See page: 23

[52] G. E. Astrakharchik, J. Boronat, J. Casulleras, and S. Giorgini. Momentum distribution and condensate fraction of a fermion gas in the BCS-BEC crossover. *Phys. Rev. Lett.*, 95:230405, 2005. See pages: 23, 26, 31

[53] C. A. Regal et al. Momentum distribution of a Fermi gas of atoms in the BCS-BEC crossover. *Phys. Rev. Lett.*, 95:250404, 2005. See page: 23

[54] R. Combescot, M. Yu. Kagan, and S. Stringari. Collective mode of homogeneous Fermi gases in the BEC-BCS crossover. *Phys. Rev. A*, 74:042717, 2006. See page: 23

[55] D. E. Miller et al. Critical velocity for superfluid flow across the BEC-BCS crossover. *Phys. Rev. Lett.*, 99:070402, 2007. See pages: 23, 88, 89

[56] W. Weimer et al. Critical velocity in the BEC-BCS crossover. *Phys. Rev. Lett.*, 114: 095301, 2015. See pages: 23, 88, 89

[57] E. M. Lifshitz and L. P. Pitaevskii. *Statistical Physics*. Elsevier, 1980. See page: 24

[58] O. Penrose and L. Onsager. Bose-Einstein condensation and liquid helium. *Phys. Rev.*, 104(3):576, 1956. See page: 24

[59] L. Salasnich, N. Manini, and A. Parola. Condensate fraction of a Fermi gas in the BCS-BEC crossover. *Phys. Rev. A*, 72:023621, 2005. See page: 25

[60] N. R. Cooper and Z. Hadzibabic. Measuring the superfluid fraction of an ultracold atomic gas. *Phys. Rev. Lett.*, 104:030401, 2010. See page: 25

[61] N. D. Mermin and H. Wagner. Absence of ferromagnetism or antiferromagnetism in one- or two-dimensional isotropic Heisenberg models. *Phys. Rev. Lett.*, 17:1133–1136, 1966. See page: 25

[62] A. L. Sidorenkov et al. Second sound and the superfluid fraction in a Fermi gas with resonant interactions. *Nature*, 498:78–81, 2013. See pages: 26, 74

[63] M. R. Andrews et al. Observation of interference between two Bose condensates. *Science*, 275:637–641, 1997. See page: 27

[64] K. W. Madison, F. Chevy, W. Wohlleben, and J. Dalibard. Vortex formation in a stirred Bose-einstein condensate. *Phys. Rev. Lett.*, 84:806–809, 2000. See page: 27

[65] C. Raman et al. Vortex nucleation in a stirred Bose-Einstein condensate. *Phys. Rev. Lett.*, 87:210402, 2001.

[66] J. R. Abo-Shaeer, C. Raman, J. M. Vogels, and W. Ketterle. Observation of vortex lattices in Bose-Einstein condensates. *Science*, 292:476, 2001. See page: 27

[67] A. Smerzi, S. Fantoni, S. Giovanazzi, and S. R. Shenoy. Quantum coherent atomic tunneling between two trapped Bose-Einstein Condensates. *Phys. Rev. Lett.*, 79: 4950–4953, 1997. See pages: 28, 80

[68] P. Zou and F. Dalfovo. Josephson oscillations and self-trapping of superfluids fermions in a double-well potential. *arxiv:1401.2007*, 2014. See pages: 28, 29, 30, 83

[69] T. Zibold, E. Nicklas, C. Gross, and M. K. Oberthaler. Classical bifurcation at the transition from Rabi to Josephson dynamics. *Phys. Rev. Lett.*, 105:204101, 2010. See page: 29

[70] I. Zapata, F. Sols, and A. J. Leggett. Josephson effect between trapped Bose-Einstein condensates. *Phys. Rev. A*, 57:R28–R31, 1998. See pages: 30, 78, 80

[71] A. J. Dahm, A. Denenstein, T. F. Finnegan, D. N. Langenberg, and D. J. Scalapino. Study of the Josephson plasma resonance. *Phys. Rev. Lett.*, 20:859–863, 1968. See page: 30

[72] F. Meier and W. Zwerger. Josephson tunneling between weakly interacting Bose-Einstein condensates. *Phys. Rev. A*, 64:033610, 2001. See pages: 30, 31, 33, 83

[73] V. Ambegaokar and A. Baratoff. Tunneling between superconductors. *Phys. Rev. Lett.*, 10:486–489, 1963. See page: 30

[74] S. Raghavan, A. Smerzi, S. Fantoni, and S. R. Shenoy. Coherent oscillations between two weakly coupled Bose-Einstein Condensates: Josephson effects, π oscillations, and macroscopic quantum self-trapping. *Phys. Rev. A*, 59:620–633, 1999. See page: 31

[75] M. Albiez et al. Direct observation of tunneling and nonlinear self-trapping in a single bosonic Josephson junction. *Phys. Rev. Lett.*, 95:010402, 2005. See page: 31

[76] S. Levy, E. Lahoud, I. Shomoroni, and J. Steinhauer. The a.c. and d.c. Josephson effects in a Bose-Einstein condensate. *Nature*, 449:579–583, 2007. See page: 31

[77] M. Abbarchi et al. Macroscopic quantum self-trapping and Josephson oscillations of exciton polaritons. *Nature Physics*, 9:275–279, 2013. See page: 31

[78] I. Giaever. Electron tunneling between two superconductors. *Phys. Rev. Lett.*, 5: 464–466, 1960. See page: 32

[79] S. Finazzi, F. Piazza, M. Abad, A. Smerzi, and A. Recati. Instability of the superfluid flow as black-hole lasing effect. *Phys. Rev. Lett.*, 114:245301, 2015. See pages: 33, 83

[80] F. Piazza, L. A. Collins, and A. Smerzi. Instability and vortex ring dynamics in a three-dimensional superfluid flow through a constriction. *New Journal of Physics*, 13:043008, 2011. See pages: 33, 83

[81] M. Abad et al. Phase-slips and vortex dynamics in josephson oscillations between Bose-Einstein condensates. *EPL*, 105:40005, 2015. See page: 33

[82] J. Hubbard. Electron correlations in narrow energy bands. *Proceedings of the Royal Society of London A: Mathematical, Physical and Engineering Sciences*, 276:238–257, 1963. See page: 33

[83] M. Brando, D. Belitz, F. M. Grosche, and T. R. Kirkpatrick. Metallic quantum ferromagnets. *arxiv:1502.02898*, 2015. See page: 34

[84] G. B. Jo. *Quantum Coherence and Magnetism in Bosonic and Fermionic Gases of Ultracold Atoms*. PhD thesis, MIT, 2010. See page: 35

[85] D. Belitz, T. R. Kirkpatrick, and T. Vojta. First order transitions and multicritical points in weak itinerant ferromagnets. *Phys. Rev. Lett.*, 82:4707–4710, 1999. See page: 36

[86] D. Belitz, T. R. Kirkpatrick, and T. Vojta. How generic scale invariance influences quantum and classical phase transitions. *Rev. Mod. Phys.*, 77:579–632, 2005. See page: 36

[87] D. Belitz and T.R. Kirkpatrick. A compilation of metallic systems that show a quantum ferromagnetic transition. *arXiv:1204.0873*, 2012. See page: 36

[88] R. A. Duine and A. H. MacDonald. Itinerant ferromagnetism in an ultracold atom Fermi gas. *Phys. Rev. Lett.*, 95:230403, 2005. See page: 36

[89] S. Pilati, G. Bertaina, S. Giorgini, and M. Troyer. Itinerant ferromagnetism of a repulsive atomic Fermi gas: A Quantum Monte Carlo study. *Phys. Rev. Lett.*, 105: 030405, 2010. See pages: 36, 118

[90] G. F. Giuliani and G. Vignale. *Quantum theory of the electron liquid*. Cambridge University press, 2005. See pages: 36, 37

[91] L. D. Landau. The theory of a Fermi liquid. *Soviet Physics JETP*, 2:920–925, 1957. See page: 37

[92] L. D. Landau. Oscillations in a Fermi liquid. *Soviet Physics JETP*, 5:101–108, 1957. See page: 37

[93] F. Chevy. Universal phase diagram of a strongly interacting Fermi gas with unbalanced spin populations. *Phys. Rev. A*, 74:063628, 2006. See page: 38

[94] R. Schmidt and T. Enss. Excitation spectra and rf response near the polaron-to-molecule transition from the functional renormalization group. *Phys. Rev. A*, 83: 063620, 2011. See pages: 38, 115, 124

[95] P. Massignan and G. M. Bruun. Repulsive polarons and itinerant ferromagnetism in strongly polarized Fermi gase. *EPJD*, 65:83–89, 2011. See pages: 39, 114

[96] C. Kohstall et al. Metastability and coherence of repulsive polarons in a strongly interacting fermi mixture. *Nature*, 485:615–618, 2012. See pages: 40, 121, 124

[97] P. Massignan, Z. Yu, and G. M. Bruun. Itinerant ferromagnetism in a polarized two-component Fermi gas. *Phys. Rev. Lett.*, 110:230401, 2013. See page: 40

[98] R. Grimm, M. Weidemüller, and Y. B. Ovchinnikov. Optical dipole traps for neutral atoms. *Advances in Atomic, Molecular and Optical Physics*, 42:95–170, 2000. See pages: 47, 77

[99] H. J. Metcalf and P. van der Straten. *Laser cooling and trapping*. Spinger Science, 1999. See page: 51

[100] E. L. Raab et al. Trapping of neutral sodium atoms with radiation pressure. *Phys. Rev. Lett.*, 59:2631–2634, 1987. See page: 53

[101] G. Reinaudi, T. Lahaye, Z. Wang, and D. Guéry-Odelin. Strong saturation absorption imaging of dense clouds of ultracold atoms. *Optics Letters*, 32(21), 2007. See page: 56

[102] T. Yefsah et al. Exploring the thermodynamics of a two-dimensional Bose-gas. *Phys. Rev. Lett.*, 107:130401, 2011. See page: 56

[103] Y. Shin et al. Observation of phase-separation in a strongly interacting imabalanced Fermi gas. *Phys. Rev. Lett.*, 97:030401, 2006. See page: 56

[104] A. L. Gaunt and Z. Hadzibabic. Robust digital holography for robust ultracold atom trapping. *Scientific Reports*, 2:721, 2012. See page: 59

[105] Z. Hadzibabic et al. Fiftyfold improvement in the number of quantum degenerate fermionic atoms. *Phys. Rev. Lett.*, 91(16):160401, 2003. See page: 61

[106] P.M. Duarte et al. All-optical production of a lithium quantum gas using narrow-line laser cooling. *Phys. Rev. A*, 84:061406, 2011. See page: 61

[107] T. W. Hänsch and A. L. Schawlow. Cooling of gases by laser radiation. *Opt. Comm.*, 13(1):68–69, 1975. See page: 61

[108] P. D. Lett. et al. Observation of atoms laser cooled below the Doppler limit. *Phys. Rev. Lett.*, 61(2):169, 1988. See page: 61

[109] J. Dalibard and C. Cohen-Tannoudji. Laser cooling below the Doppler limiti by polarization gradients - simple thepretical models. *Jour. Opt. Soc. Am. B*, 6:2023–2045, 1989. See page: 62

[110] D. Rio Fernandes et al. Sub-doppler laser cooling of fermionic ^{40}K atoms in three-dimensional gray optical molasses. *EPL*, 100(6):63001, 2012. See page: 62

[111] A. Aspect et al. Laser cooling below the one-photon recoil energy by velocity-selective coherent population trapping. *Phys. Rev. Lett.*, 61:826, 1988. See page: 62

[112] D. Boiron et al. Laser cooling of cesium atoms in gray optical molasses down to 1.1 μK. *Phys. Rev. A*, 53:R3734–R3737, 1996. See page: 62

[113] D. Rio Fernandes. *Trapping and cooling of fermionic alkali atoms to quantum degeneracy. Sub-Doppler cooling of Potassium-40 and Lithium-6 in gray molasses*. PhD thesis, LKB-ENS Paris, 2014. See page: 63

[114] A. T. Grier et al. Λ-enhanced sub-doppler cooling of lithium atoms in D1 gray molasses. *Phys. Rev. A*, 87:063411, 2013. See page: 65

[115] E. Haller et al. Single-atom imaging of fermions in a quantum-gas microscope. *Nat. Phys.*, 11:738–742, 2015. See page: 67

[116] L. W. Cheuk et al. Quantum-gas microscope for fermionic atoms. *Phys. Rev. Lett.*, 114:193001, 2015. See page: 67

[117] M. F. Parsons and et al. Site-resolved imaging of fermionic ^{6}Li in an optical lattice. *Phys. Rev. Lett.*, 114:213002, 2015. See page: 67

[118] D. S. Petrov. Three-body problem in fermi gases with short-range interparticle interaction. *Phys. Rev. A*, 67:010703(R), 2003. See pages: 68, 119

[119] C. Chin and R. Grimm. Thermal equilibrium and efficient evaporation of an ultracold atom-molecule mixture. *Phys. Rev. A*, 69:033612, 2004. See pages: 68, 122

[120] Mohit Randeria and Edward Taylor. Crossover from Bardeen-Cooper-Schrieffer to Bose-Einstein Condensation and the Unitary Fermi Gas. *Annual Review of Condensed Matter Physics*, 5:209–232, 2014. See page: 68

[121] M. W. Zwierlein et al. Vortices and superfluidity in a strongly interacting Fermi gas. *Nature*, 435:1047–1051, 2005. See pages: 69, 92

[122] M. J. H. Ku, A. T. Sommer, L. W. Cheuk, and M. W. Zwierlein. Revealing the superfluid lambda transition in the universal thermodynamics of a Unitary Fermi gas. *Science*, 335:563–567, 2012. See pages: 69, 70, 99

[123] N. Navon, S. Nascimbene, F. Chevy, and C. Salomon. The equation of state of a low-temperature Fermi gas with tunable interactions. *Science*, 328:729, 2010. See page: 69

[124] S. Nascimbene, N. Navon, K. J. Jiang, F. Chevy, and C. Salomon. Exploring the thermodynamics of a universal Fermi gas. *Nature*, 463:1057, 2010. See page: 69

[125] A. Amico. Master thesis: Measurement of the equation of state of superfluid Fermi gases of ^{6}Li atoms, 2014. See page: 74

[126] E. Arimondo, M. Inguscio, and P. Violino. Experimental determinations of the hyperfine structure in the alkali atoms. *Rev. Mod. Phys.*, 49:31–75, 1977. See page: 77

[127] D. Stadler et al. Observing the drop of resistance in the flow of a superfluid fermi gas. *Nature*, 491:736–739, 2012. See pages: 80, 91

[128] A. Spuntarelli, P. Pieri, and G. C. Strinati. Josephson effect throughout the BCS-BEC crossover. *Phys. Rev. Lett.*, 99:040401, 2007. See page: 86

[129] C. Kohstall et al. Observation of interference between two molecular Bose-Einstein condensates. *New. Journ. Phys.*, 13:065027, 2011. See page: 86

[130] A. Spuntarelli, P. Pieri, and G. C. Strinati. Solution of the Bogolioubov-de Gennes equations at zero temperature throughout the BCS-BEC crossover: Josephson and related effects. *Phys. Rep.*, 488:111–167, 2010. See page: 90

[131] L. Bretheau et al. Exciting Andreev pairs in a superconducting atomic contact. *Nature*, 499:312, 2013. See page: 90

[132] G. Deutscher. Andreev-saint-james reflections: a probe of cuprate superconductors. *Rev. Mod. Phys.*, 77:109, 2005. See pages: 90, 100

[133] D. Husmann et al. Connecting strongly correlated superfluids by a quantum point contact. *Science*, 350:1498, 2015. See page: 90

[134] S. Gandolfi, K. E. Schmidt, and J. Carlson. BEC-BCS crossover and universal relations in unitary Fermi gases. *Phys. Rev. A*, 83:041601, 2011. See page: 90

[135] M. J. H. Ku et al. Motion of a solitonic vortex in the BEC-BCS crossover. *Phys. Rev. Lett.*, 113:065301, 2014. See page: 93

[136] M. J. K. Ku, B. Mukherjee, and T. Yefsahand M. W. Zwierlein. Cascade of solitonic excitations in a superfluid Fermi gas: From planar solitons to vortex rings and lines. *Phys. Rev. Lett.*, 116:045304, 2016. See page: 93

[137] L. D. Landau. The theory of superfluidity in helium ii. *J. Phys USSR*, V:71, 1941. See page: 94

[138] R. P. Feynman. Atomic theory of the λ transition in helium. *Phys. Rev.*, 91:1291–1301, 1953.

[139] R. P. Feynman. Atomic theory of liquid helium near absolute zero. *Phys. Rev.*, 91: 1301–1308, 1953. See page: 94

[140] Z. Hadzibabic et al. Interference of an array of independent Bose-Einstein Condensates. *Phys. Rev. Lett.*, 93:180403, 2004. See page: 95

[141] J. P. Brantut et al. Conduction of ultracold fermions through a mesoscopic channel. *Science*, 31:1069–1071, 2012. See page: 96

[142] G. E. Astrakharchik, J. Boronat, J. Casulleras, and S. Giorgini. Equation of state of a Fermi gas in the BEC-BCS crossover: A Quantum Monte Carlo study. *Phys. Rev. Lett.*, 93:200404, 2004. See page: 99

[143] A. L. Gaunt et al. Bose-Einstein condensation of atoms in a uniform potential. *Phys. Rev. Lett.*, 110:200406, 2013. See page: 100

[144] D. Pekker et al. Competition between pairing and ferromagnetic instabilities in ultracold Fermi gases near Feshbach resonances. *Phys. Rev. Lett.*, 106:050402, 2011. See pages: 102, 120, 121

[145] A. Recati and S. Stringari. Spin fluctuations, susceptibility, and the dipole oscillation of a nearly ferromagnetic Fermi gas. *Phys. Rev. Lett.*, 106:080402, 2011. See pages: 105, 106, 109, 116

[146] R. A. Duine, M. Polini, H. T. C. Stoof, and G. Vignale. Spin drag in an ultracold Fermi gas on the verge of ferromagnetic instability. *Phys. Rev. Lett.*, 104:220403, 2010. See pages: 109, 124

[147] E. Taylor, S. Zhang, W. Schneider, and M. Randeria. Colliding clouds of strongly interacting spin-polarized fermions. *Phys. Rev. A*, 84:063622, 2011. See pages: 109, 125

[148] A. Sommer, M. Ku, G. Roati, and M. W. Zwierlein. Universal spin transport in a strongly interacting Fermi gas. *Nature*, 472:201–204, 2011. See pages: 109, 113, 114, 120, 124

[149] S. Zhang and T. L. Ho. Atom loss maximum in ultra-cold Fermi gases. *New Journal of Physics*, 13:055003, 2011. See page: 109

[150] S. D. Gensemer and D. S. Jin. Transition from collisionless to hydrodynamic behavior in an ultracold Fermi gas. *Phys. Rev. Lett.*, 87:173201, 2001. See page: 110

[151] M. Cetina, M. Jag, R. S. Lous, J. T. M. Walraven, R. Grimm, R. S. Christensen, and G. M. Bruun. Decoherence of impurities in a Fermi sea of ultracold atoms. *Phys. Rev. Lett.*, 115:135302, 2015. See page: 112

[152] I. Zintchenko, L. Wang, and M. Troyer. Ferromagnetism of the repulsive atomic Fermi gas: three-body recombination and domain formation. *arXiv:1308.1961*, 2013. See page: 113

[153] E. Haller et al. Realization of an excited, strongly correlated quantum gas phase. *Science*, 325:1224–1227, 2009. See page: 116

[154] S. Pilati, I. Zintchenko, and M. Troyer. Ferromagnetism of a repulsive atomic Fermi gas in an optical lattice: A Quantum Monte Carlo study. *Phys. Rev. Lett.*, 112: 015301, 2014. See page: 119

[155] S. Pilati and E. Fratini. Ferromagnetism in a repulsive atomic Fermi gas with correlated disorder. *arxiv:1604.01052*, 2016. See page: 119

[156] L. Vichi and S. Stringari. Collective oscillations of an interacting trapped Fermi gas. *Phys. Rev. A*, 60:4734–4737, 1999. See page: 120

[157] E. Elliott, J. A. Joseph, and J.E. Thomas. Anomalous minimum in the shear viscosity of a Fermi gas. *Phys. Rev. Lett.*, 113:020406, 2014. See page: 120

[158] A. B. Bardon et al. Transverse demagnetization dynamics of a Unitary Fermi gas. *Science*, 344:722–724, 2014. See page: 120

[159] S. Trotzky et al. Observation of the Leggett-Rice effect in a Unitary Fermi gas. *Phys. Rev. Lett.*, 114:015301, 2015. See page: 120

[160] G. M. Bruun and C. J. Pethick. Spin diffusion in trapped clouds of cold atoms with resonant interactions. *Phys. Rev. Lett.*, 107:255302, 2011. See page: 120

[161] G. M. Bruun. Spin diffusion in Fermi gases. *New Journal of Physics*, 13:035005, 2011. See page: 120

[162] S. Nascimbène et al. Fermi-liquid behavior of the normal phase of a strongly interacting gas of cold atoms. *Phys. Rev. Lett.*, 106:215303, 2011. See page: 125

[163] T. Kashimura, R. Watanabe, and Y. Ohashi. Spin susceptibility and fluctuation corrections in the BCS-BEC crossover regime of an ultracold Fermi gas. *Phys. Rev. A*, 86:043622, 2012. See page: 125

[164] S. Shapiro. Josephson currents in superconducting tunneling: The effect of microwaves and other observations. *Phys. Rev. Lett.*, 11:80–82, 1963. See page: 127

[165] I. Boettcher et al. Equation of state of ultracold fermions in the 2D BEC-BCS crossover region. *Phys. Rev. Lett.*, 116:045303, 2016. See page: 127

[166] K. Fenech et al. Thermodynamics of an attractive 2D Fermi gas. *Phys. Rev. Lett.*, 116:045302, 2016. See page: 127

[167] Andrea M. Fischer and Meera M. Parish. Quasi-two-dimensional Fermi gases at finite temperatures. *Phys. Rev. B*, 90:214503, 2014. See page: 128

[168] D. Greif et al. Site-resolved imaging of a fermionic Mott insulator. *Science*, 351: 953–957, 2016. See page: 128

[169] Y. J. Lin et al. Synthetic magnetic fields for ultracold neutral atoms. *Nature*, 462: 628–632, 2009. See page: 128

[170] M. Mancini et al. Observation of chiral edge states with neutral fermions in synthetic Hall ribbons. *Science*, 25:1510–1513, 2015. See page: 128

[171] B. K. Stuhl et al. Visualizinge edge states in an atomic Bose gas in the quantum Hall regime. *Science*, 25:1510–1513, 2015. See page: 128

[172] C. Laflamme, J. C. Budich, P. Zoller, and M. Dalmonte. Non-equilibrium 8π Josephson Effect in Atomic Kitaev Wires. *ArXiv:1602.05845*, 2016. See page: 128

[173] T. Schaetz, C. R. Monroe, and T. Esslinger. Focus on quantum simulation. *NJP*, 15: 085009, 2013. See page: 128

[174] T. Esslinger. Fermi-Hubbard physics with atoms in an optical lattice. *Ann. Rev. of Cond. Matter Phys.*, 1:129–152, 2010. See page: 128